

**OPERATIONAL STRUCTURAL DAMAGE
IDENTIFICATION USING DE-NOISED MODAL FEATURE
IN MACHINE LEARNING**

CHEN SHILEI

**FACULTY OF ENGINEERING
UNIVERSITY OF MALAYA
KUALA LUMPUR**

2021

**OPERATIONAL STRUCTURAL DAMAGE
IDENTIFICATION USING DE-NOISED MODAL
FEATURE IN MACHINE LEARNING**

CHEN SHILEI

**THESIS SUBMITTED IN FULFILMENT OF THE
REQUIREMENTS FOR THE DEGREE OF MASTER OF
ENGINEERING SCIENCE**

**FACULTY OF ENGINEERING
UNIVERSITY OF MALAYA
KUALA LUMPUR**

2021

UNIVERSITY OF MALAYA
ORIGINAL LITERARY WORK DECLARATION

Name of Candidate: Chen Shilei

Matric No: KGA180015

Name of Degree: Master of Engineering Science

Title of Project Paper/Research Report/Dissertation/Thesis ("this Work"):

Operational structural damage identification using de-noised modal feature in machine learning.

Field of Study:

Vibration

I do solemnly and sincerely declare that:

- (1) I am the sole author/writer of this Work;
- (2) This Work is original;
- (3) Any use of any work in which copyright exists was done by way of fair dealing and for permitted purposes and any excerpt or extract from, or reference to or reproduction of any copyright work has been disclosed expressly and sufficiently and the title of the Work and its authorship have been acknowledged in this Work;
- (4) I do not have any actual knowledge nor do I ought reasonably to know that the making of this work constitutes an infringement of any copyright work;
- (5) I hereby assign all and every rights in the copyright to this Work to the University of Malaya ("UM"), who henceforth shall be owner of the copyright in this Work and that any reproduction or use in any form or by any means whatsoever is prohibited without the written consent of UM having been first had and obtained;
- (6) I am fully aware that if in the course of making this Work I have infringed any copyright whether intentionally or otherwise, I may be subject to legal action or any other action as may be determined by UM.

Candidate's Signature

Date:

Subscribed and solemnly declared before,

Witness's Signature

Date:

Name:

Designation:

OPERATIONAL STRUCTURAL DAMAGE IDENTIFICATION USING DE-NOISED MODAL FEATURE IN MACHINE LEARNING

ABSTRACT

Structural damage can severely affect the safety and functionality of the structure and lead to economic loss. Vibration-based structural damage detection has raised continuous interest over the decades, as a non-destructive way to provide warnings and predict certain faults at early stages. Compared with conventional modal parameters such as the natural frequency and mode shape, the upstream modal data, namely the frequency response function (FRF), can be a better alternative, because it is rich in modal information and can be easily obtained. However, the FRF is usually measured through experimental modal analysis (EMA) when the test object is in shut-down mode, which is not practical for real-time application in the working environment. This limitation can be overcome by a novel technique named impact-synchronous modal analysis (ISMA) performed under the operational condition. Machine learning is also a focus in this work, which was employed to process and classify FRF data in terms of damage. By integrating ISMA, both supervised and unsupervised machine learning algorithms were investigated to develop real-time damage identification schemes. Specifically, the back-propagation (BP) network was employed in the supervised learning method, and the FRF changes in a selected frequency interval at several measurement points were used as the input of the network. The unsupervised learning method was developed by combining principal component analysis (PCA), waveform chain code (WCC) analysis and hierarchical cluster analysis. WCC analysis was carried out on the PCA-reduced FRF to extract damage-sensitive PCA-WCC features. The unsupervised hierarchical cluster analysis was then conducted on these features. The proposed schemes were tested on a rectangular Perspex plate. The results show that the similarity between the FRF obtained by ISMA

and EMA exceeds 0.993, proving that the de-noising method of ISMA provides static comparable FRF data during the in-service condition. For the supervised learning method, the trained BP network can successfully identify the scenarios of high and moderate damage with an overall accuracy of 100% when all five measurement points are used. With the input features optimized by mode shape assessment, 100% accuracy can also be achieved with only two measurement points. For the unsupervised learning method, the hierarchical cluster analysis can correctly cluster the samples in terms of their damage states. In terms of damage severity and location identification, the proposed scheme is sensitive to detect damage severity with damage index as low as 0.05. In addition, the combination of PCA-reduced FRF and mode shapes shows a positive correlation between the magnitude of the resonant peak and the displacement of the impact point in identifying the damage location of the plate. In conclusion, the supervised learning method using FRF change is convenient and effective in identifying the damage state of the plate, and can be optimized through mode shape assessment. Meanwhile, the unsupervised learning method using PCA-WCC features is good at detecting unknown damage, and is sensitive to low-severity damage. With the help of PCA-reduced FRF, it is also feasible to estimate the severity and locate the damage of the test plate.

Keywords: damage identification; frequency response function; impact-synchronous modal analysis; machine learning; vibration.

**PENGESANAN KEROSAKAN STRUKTUR BEROPERASI BERDASARKAN
CIRI-CIRI MODAL BEBAS DARIPADA BUNYI DALAM TEKNIK
PEMBELAJARAN MESIN**

ABSTRAK

Kerosakan struktur boleh menjejaskan keselamatan dan fungsinya serta turut mengakibatkan kerugian ekonomi. Pengesanan kerosakan struktur berasaskan getaran, sebagai cara tanpa penjejasan dalam memberi amaran dan ramalan kerosakan, semakin menarik minat secara berterusan daripada lebih banyak pengkaji selama beberapa dekad. Berbanding dengan menggunakan parameter modal konvensional seperti frekuensi dan bentuk mod, kaedah menggunakan data upstream seperti frekuensi response function (FRF), ialah alternatif yang lebih baik kerana FRF kaya dengan maklumat modal dan mudah diperolehi. Walau bagaimanapun, FRF biasanya diperolehi melalui kaedah analisis modal eksperimen (EMA) ketika objek yang diuji tidak beroperasi. Kaedah ini tidak praktikal untuk aplikasi sebenar yang berada di persekitaran kerja yang beroperasi. Oleh itu, FRF dapat diekstrak melalui kaedah analisis modal serasi impak (ISMA) dari objek uji yang berada dalam keadaan operasi. Kaedah pembelajaran mesin digunakan untuk memproses dan menganalisis data FRF yang dikumpul untuk pengesanan kerosakan. Bersama dengan ISMA, cara pembelajaran mesin *supervised* dan *unsupervised learning* dikaji untuk membina skema pengesanan kerosakan secara langsung. Rangkaian *back-propagation* (BP) digunakan sebagai cara *supervised learning*, manakala data yang dimasukkan ke dalam rangkaian ini untuk latihan data ialah perubahan data FRF dalam jarak frekuensi terpilih diukur dari beberapa titik pengukuran. Gabungan analisis komponen prinsipal (PCA), analisis gelombang rantai kod (WCC) dan analisis kluster secara hierarki digunakan untuk skema pengesanan kerosakan yang berdasarkan cara *unsupervised learning*. Analisis WCC dijalankan pada FRF yang

dikurangkan oleh PCA untuk mengekstrak ciri-ciri PCA-WCC yang sensitif terhadap kerosakan. Seterusnya, analisis kluster secara hierarki dijalankan pada ciri-ciri PCA-WCC tersebut. Skema yang dicadangkan diuji pada plat Perspex bersegi-empat tepat. Kajian ini menunjukkan bahawa persamaan antara FRF yang diperoleh oleh ISMA dan EMA adalah lebih daripada 0.993. Ini membuktikan bahawa kaedah ISMA dapat memberikan data FRF yang setanding dengan EMA semasa objek berada dalam keadaan beroperasi. Untuk kaedah *supervised learning*, rangkaian BP yang terlatih berjaya mengesan kerosakan tahap tinggin dan sederhana, dengan ketepatan keseluruhan 100% apabila semua lima titik pengukuran digunakan. Selain itu, apabila skema ini dioptimumkan dengan penilaian bentuk mod, ketepatannya masih 100% dengan hanya menggunakan dua titik pengukuran. Untuk kaedah *unsupervised learning*, analisis kluster secara hierarki dapat mengumpulkan sampel mengikut keadaan kerosakan dengan tepat. Skema yang dicadangkan dapat mengesan keparahan kerosakan indeks serendah 0.05. Gabungan FRF yang dikurang oleh PCA dan bentuk mod telah menunjukkan korelasi positif antara puncak resonan dengan anjakan titik hentaman dalam mengenal pasti lokasi kerosakan plat. Kesimpulannya, kaedah *supervised learning* dengan menggunakan perubahan FRF mudah dan berkesan dalam mengesan keadaan kerosakan plat dan dapat dioptimumkan melalui penilaian bentuk mod. Sementara itu, kaedah *unsupervised learning* dengan menggunakan ciri PCA-WCC dapat mengesan kerosakan baru dan kerosakan tahap rendah. Keparahan dan lokasi kerosakan di plat uji dapat dikesan dengan menggunakan FRF yang dikurang oleh PCA.

Keywords: pengesanan kerosakan; frekuensi response function; analisis modal serasi impak; pembelajaran mesin; getaran.

ACKNOWLEDGEMENTS

The completion of the thesis is attributed to many people's support and encouragement.

First and foremost, I want to express my sincere gratitude to my supervisor, Dr. Ong Zhi Chao. His patient guidance, valuable suggestions and constant encouragement are of great help to my research work and will always be valuable for my future career.

My thanks also go to all the teachers and classmates who have helped me with my studies in University of Malaya. I am particularly grateful to Ms Siow Pei Yi for her assistance in the experimental work.

Last but not least, I would like to express my special thanks to my parents. Their love, care and support have always been my source of motivation and strength to pursue my goals.

Universiti Malaya

TABLE OF CONTENTS

Abstract	iii
Abstrak	v
Acknowledgements	vii
Table of Contents	viii
List of Figures	xi
List of Tables.....	xiii
List of Symbols and Abbreviations.....	xiv
List of Appendices	xvii
CHAPTER 1: INTRODUCTION.....	1
1.1 Background.....	1
1.2 Motivation.....	3
1.3 Objectives of research.....	4
1.4 Outline of thesis	5
CHAPTER 2: LITERATURE REVIEW AND BACKGROUND THEORIES.....	6
2.1 Literature review.....	6
2.1.1 Introduction	6
2.1.2 Vibration-based damage detection techniques using modal parameters....	6
2.1.2.1 Natural frequency	7
2.1.2.2 Mode shape	8
2.1.2.3 Mode shape derivatives	9
2.1.2.4 Strain energy	9
2.1.2.5 Frequency response function.....	10
2.1.3 Impact-synchronous modal analysis.....	11

2.1.4	Machine learning in damage identification	15
2.1.5	Summary.....	19
2.2	Background theories	21
2.2.1	FRF measurement using ISMA.....	21
2.2.2	FRF change.....	23
2.2.3	PCA-reduced FRF	24
2.2.4	WCC analysis	25
2.2.5	BP network	27
2.2.6	Hierarchical cluster analysis based on complex network theory.....	30
CHAPTER 3: METHODOLOGY		33
3.1	Introduction.....	33
3.2	Research flow and scope	33
3.3	Experimental set-up	35
3.4	Design of experiment and procedures	38
3.4.1	Modal analysis using ISMA de-noising method under operational condition.....	38
3.4.2	Development of operational damage identification scheme using supervised learning.....	40
3.4.3	Development of operational damage identification scheme using unsupervised learning.....	43
CHAPTER 4: RESULTS AND DISCUSSION.....		46
4.1	Introduction.....	46
4.2	Modal analysis using ISMA de-noising method under operational condition	46
4.2.1	Measurement of FRF using ISMA under operational condition.....	46
4.2.2	Acquisition of natural frequencies and mode shapes	50

4.3	Development of operational damage identification scheme using supervised learning	54
4.3.1	Construction of input feature: FRF change	54
4.3.2	Damage identification using BP network.....	63
4.3.3	Optimization of measurement points using mode shape assessment	68
4.4	Development of operational damage identification scheme using unsupervised learning	71
4.4.1	Construction of WCC features from PCA-reduced FRF.....	71
4.4.2	Hierarchical cluster analysis.....	81
4.4.3	Damage identification using PCA-reduced FRF	87
4.5	Summary.....	95
CHAPTER 5: CONCLUSIONS.....		97
5.1	Conclusions.....	97
5.2	Future work.....	98
References		100
List of Publications and Papers Presented		106
Appendix A		107

LIST OF FIGURES

Figure 2.1: Structure of three-layer BP network.....	27
Figure 3.1: Flow chart.....	33
Figure 3.2: Experimental set-up.....	36
Figure 3.3: Measurement points, damage location and impact location.....	37
Figure 4.1: EMA and ISMA FRFs measured in UD scenario	48
Figure 4.2: First three mode shapes of plate with different damage locations	53
Figure 4.3: Comparison of FRFs of HD scenarios.....	55
Figure 4.4: Input features of network: FRF change δ in 10~25 Hz.....	57
Figure 4.5: Input features of network: FRF change δ in 30~40 Hz.....	59
Figure 4.6: Input features of network: FRF change δ in 45~55 Hz.....	60
Figure 4.7: Testing results of damage identification based on BP network using FRF change of five measurement points (UD, LD, MD and HD scenarios).....	67
Figure 4.8: Second and third mode shapes of plate	70
Figure 4.9: FRFs and PCA-reduced FRF of UD scenario	72
Figure 4.10: PCA-reduced FRF of all scenarios	73
Figure 4.11: Slope differential value sequences	75
Figure 4.12: PCA-WCC features of different damage states.....	81
Figure 4.13: Modularity Q in respect to number of clusters	82
Figure 4.14: Dendrogram.....	84
Figure 4.15: Results of hierarchical clustering	85
Figure 4.16: Second resonant peaks of PCA-reduced FRFs.....	87
Figure 4.17: First and second resonant peaks of PCA-reduced FRFs.....	90
Figure 4.18: First mode shapes of plate under different damage states.....	91

Figure 4.19: First mode shapes of plate with PCA-reduced FRF near first resonant peaks 93

Figure 4.20: Second mode shapes of plate with PCA-reduced FRF near second resonant peaks..... 94

Universiti Malaya

LIST OF TABLES

Table 3.1: List of damage scenarios and descriptions.....	38
Table 3.2: Settings of three-layer BP network.....	42
Table 3.3: Notation for comparing two partitions.....	45
Table 4.1: FRAC between the FRFs measured by EMA and ISMA	49
Table 4.2: First three natural frequencies of plate obtained by EMA and ISMA	50
Table 4.3: MAC between mode shapes obtained by EMA and ISMA	54
Table 4.4: Comparison between natural frequency and FRF change of first mode.....	62
Table 4.5: Comparison between natural frequency and FRF change of second mode ...	62
Table 4.6: Comparison between natural frequency and FRF change of third mode.....	63
Table 4.7: Performance of damage identification based on BP network using FRF change of five measurement points (UD, LD, MD and HD scenarios)	63
Table 4.8: Performance of damage identification based on BP network using FRF change of five measurement points (UD, HD and MD scenarios).....	68
Table 4.9: Performance of damage identification based on BP network using FRF change of two measurement points (UD, HD and MD scenarios).....	69
Table 4.10: Feature a_{s1} in comparison with shift in first resonant peak of PCA-reduced FRF.....	76
Table 4.11: Feature a_{s2} in comparison with shift in second resonant peak of PCA-reduced FRF.....	77
Table 4.12: Feature a_{s3} in comparison with shift in third resonant peak of PCA-reduced FRF.....	78
Table 4.13: ARI performance of new hierarchical clustering and k-means clustering...	86
Table 4.14: Reduction in second natural frequency and damage indices	88
Table 4.15: Magnitude of first and second resonant peaks.....	90

LIST OF SYMBOLS AND ABBREVIATIONS

AANN	:	Auto-associative neural network
AID	:	Automated impact device
ANN	:	Artificial neural network
ARI	:	Adjusted Rand index
ATM	:	Adaptive template matching
BP	:	Back-propagation
CE	:	Cross entropy
CNN	:	Convolutional neural network
COMAC	:	Coordinate Modal Assurance Criterion
DOF	:	Degree of freedom
ELOD	:	Equivalent level of degradation system
EMA	:	Experimental modal analysis
FFT	:	Fast-Fourier transform
FRAC	:	Frequency response assurance criterion
FRF	:	Frequency response function
HD	:	High damage
Hz	:	Hertz
ISMA	:	Impact-synchronous modal analysis
ISTA	:	Impact-synchronous time averaging
kg	:	Kilogram
LD	:	Low damage
MAC	:	Modal Assurance Criterion
MD	:	Moderate damage
MLP	:	Multi-layer perceptron

mm	:	Millimeter
MSE	:	Modal strain energy
OMA	:	Operational modal analysis
PCA	:	Principal component analysis
SAC	:	Signature assurance criterion
SHM	:	Structural health monitoring
WCC	:	Waveform chain code
\odot	:	Hadamard product
\mathbf{M}	:	Mass matrix
\mathbf{C}	:	Damping matrix
\mathbf{K}	:	Stiffness matrix
\mathbf{H}	:	FRF matrix
$\mathbf{x}(t)$:	Displacement
$\mathbf{f}(t)$:	Force
\mathbf{h}_i	:	FRF magnitude sequence measured at i -th measurement point
δ_i	:	FRF change at i -th measurement point
\mathbf{p}	:	PCA-reduced FRF
α	:	Weight coefficients of linear combination
\mathbf{u}	:	Sequence equidistantly discretized signal
\mathbf{s}	:	Slope of signal \mathbf{u}
s_{max}	:	Maximum value in slope \mathbf{s}
\mathbf{s}^{rs}	:	Scaled relative slope
\mathbf{s}^{dv}	:	Slope differential values
a_s	:	Area under \mathbf{s}^{dv} curve
$a_{s\ norm}$:	Normalized a_s

\mathbf{v}^i	:	Input vector of BP network
\mathbf{v}^t	:	Target vector of BP network
\mathbf{v}^o	:	Output vector of BP network
$\mathbf{w}^{(i)}$:	Weights of BP network
$f^{(i)}(\cdot)$:	Activation function of BP network
ϵ	:	Learning rate of BP network
J	:	Performance of BP network
S	:	Vector set
$d(\mathbf{n}_i, \mathbf{n}_j)$:	Euclidean distance between nodes \mathbf{n}_1 and \mathbf{n}_2
$w(\mathbf{n}_i, \mathbf{n}_j)$:	Weight of edge between nodes \mathbf{n}_i and \mathbf{n}_j
σ	:	Strength parameter for weight of edge
\mathcal{C}	:	Partition of set S
C_i	:	Subset of S , belonging to partition \mathcal{C}
e_{ij}	:	Class similarity between C_i and C_j
\mathbf{e}	:	Class similarity matrix
Q	:	Modularity of hierarchical clustering
ΔQ_{ij}	:	Incremental modularity with merger of C_i and C_j
ΔQ_{max}	:	Maximum of incremental modularity
$\{H\}$:	Equidistantly discretized sequences of FRF
Ψ	:	Mode shape

LIST OF APPENDICES

Appendix A.1: Figure of new test plate	107
Appendix A.2: Comparison of FRFs (new test plate)	108
Appendix A.3: FRF change (new test plate)	109
Appendix A.4: Results of damage identification based on BP network using FRF change (new test plate)	110
Appendix A.5: PCA-reduced FRF (new test plate)	110
Appendix A.6: Slope differential value sequence (new test plate)	111
Appendix A.7: Modularity Q in respect to number of clusters (new test plate) ...	111
Appendix A.8: Dendrogram (new test plate)	112
Appendix A.9: Magnitude of first and second resonant peaks (new test plate)	112

CHAPTER 1: INTRODUCTION

1.1 Background

Mechanical machines accumulate damage during their service life. Structural damage can severely affect the safety and functionality of the structure and lead to significant economic loss. Structural health monitoring (SHM) and vibration-based damage detection have raised continuous interest over the years, seeking for non-destructive ways to provide warnings and predict certain faults at early stages. Structural damage leads to alterations in physical characteristics like stiffness and damping. Consequently, the changes in the modal parameters of the structure will be observed. Hence, modal parameters offer promising alternatives for damage detection.

During the past decades, efforts have been made to develop damage detection schemes using various modal parameters. Yet, the suitability of using the downstream modal parameters is sometimes questioned. For example, the natural frequency may fail to indicate the specific location of damage and is not sensitive to the local damage. The processing procedure of mode shape-based methods is complicated, which may affect the credibility of the results and prone to more errors. It is hypothesized that the upstream modal data, namely the frequency response function (FRF), is more suitable for the use of damage detection. Frequency response refers to the quantitative measure of the output spectrum of a system or device in response to a stimulus. It describes the correspondence between the input and output of the system in the frequency domain. Compared with other dynamic features, FRF can be advantageous mainly in two aspects. First, FRF can be directly acquired in real time from the vibration transducer and then fast-Fourier transform (FFT). Second, FRF is rich in modal information and many modal parameters are originally retrieved from the raw FRFs.

Currently, there are two techniques used to extract modal parameters, including the experimental modal analysis (EMA) and the operational modal analysis (OMA). However, EMA requires the system to be in complete ‘shutdown’ mode, where there should be no unaccounted excitation force induced into the system. While in OMA, FRF is not available, for the lack of knowledge of the input forces, and the accuracy of parameters extracted is affected. A novel method named impact-synchronous modal analysis (ISMA) was thus proposed, where the actual input forces can be provided and subsequently a full FRF can be obtained even when the system is in operation. In ISMA, when the analysis is performed while the machine is in the running condition, both the responses caused by cyclic loads and random noise are filtered out in the time domain, leaving only responses triggered by the impact device (e.g. the impact hammer). This is achieved by impact-synchronous time averaging (ISTA) prior to performing FFT operation. In the time block averaging of ISTA, each time block is initiated by the impulse generated from the force trace of the impact. Taking a sufficient number of averages, the periodic responses caused by cyclic loads and ambient forces, which are non-synchronous in phase to the time block, will diminish, while the synchronous component, namely responses triggered by the impact, will be preserved. The modal parameter extraction follows EMA procedures. Therefore, ISMA is prospective in the development of a real-time damage identification scheme for continuous structural health monitoring.

Recently, machine learning techniques have received wide acceptance for locating and quantifying damage, which is often cooperated with various damage-sensitive features. Currently, supervised learning is the most favorable machine learning algorithms used in damage detection. The back-propagation (BP) network is one of the algorithms used in machine learning. The network is trained using a set of labeled training samples, and the trained network will have the ability to identify the location and the severity of the damage. However, it is difficult to obtain the complete training samples of all damage scenarios in

many practical applications, which limits the application of supervised learning methods. Meanwhile, the unsupervised learning methods help to find previously unknown patterns in the data set without pre-existing labels. Cluster analysis is a typical unsupervised learning method that is often used. However, these previous studies utilizing unsupervised learning usually focused more on detection instead of identifying the specific damage state. Also, the number of classes usually needs to be previously defined in these clustering algorithms, which has limited its practicality in real-life applications in which the damage scenarios are usually unknown in the first place. A new hierarchical clustering method based on complex network theory was thus proposed and developed by Newman and Girvan (2004), Newman (2004) and Zhang et al. (2013), which has the ability to discover the community structure in networks and divide them into densely connected clusters. The modularity Q is then defined to evaluate the quality of network division and is maximized in the process of hierarchical clustering. The clustering process is automatically terminated when the modularity reaches its maximum, and the clustering result will be obtained. Considering the good performance of the new hierarchical clustering algorithm, it may also have its potential in unsupervised vibration-based damage detection practices.

1.2 Motivation

The downstream modal data (i.e. post-processed parameters from FRFs) used in previous vibration-based damage detection methods are usually found to be deficient in damage sensitivity and noise robustness. Meanwhile, although the upstream data of FRF is rich in information and can be more advantageous in damage identification, it can be further improved in two aspects. First, FRF is mainly obtained through EMA so far, which can only be carried out when the tested object is in shut-down mode and is not practical for real-time application in the working environment. ISMA provides a prospective alternative to extract FRFs when the system is in operation and its application in damage

identification is yet to be explored. Second, there is a need to look for suitable signal processing methods to extract damage-sensitive features from FRF, as the raw FRF data are too complex to be directly applied while the improperly-selected features may be less sensitive and lead to bad performance. In this work, the signal processing methods named principal component analysis (PCA) and waveform chain code analysis (WCC) are employed.

Machine learning is a powerful tool for pattern recognition in damage identification problems, and is therefore adopted in this work. However, damage identification based on supervised learning relies on the labeled training data and suffers from the incompleteness of training samples. Meanwhile, the current unsupervised methods in damage detection are either limited to detecting the existence of damage, or in need of the number of desired clusters in advance. This study is also designated to address these problems.

1.3 Objectives of research

This research aims to develop real-time damage identification schemes based on FRF change utilizing ISMA and machine learning methods, making it possible to identify the structural damage of in-service machines. The main objectives of the proposed work can be summarized as follows:

1. To investigate the performance of the de-noising technique in ISMA in generating clean and stationary comparable FRFs under the operational condition for damage identification scheme.
2. To develop an optimized operational damage identification scheme utilizing de-noised FRF feature and supervised machine learning.

3. To develop an operational unsupervised damage identification scheme utilizing PCA-reduced FRFs and WCC analysis.

1.4 Outline of thesis

This thesis is organized as follows. Chapter 2 presents a review on techniques of vibration-based damage detection. In this chapter, the background theories involved in this study are also illustrated. The methods of this study are elaborated in Chapter 3, which includes the research flow, the experimental set-up and the design of experiment and procedures. The implementation of ISMA and the damage identification schemes based on machine learning are explained in detail. Then, the results are presented and discussed in Chapter 4. Finally, Chapter 5 summarizes the conclusions and provides a discussion for future work.

CHAPTER 2: LITERATURE REVIEW AND BACKGROUND THEORIES

2.1 Literature review

2.1.1 Introduction

Mechanical machines face structural damage problems due to various loads and other external factors during their service life. Structural damage can severely affect the safety and functionality of the structure and lead to significant economic loss. Vibration-based damage detection techniques are very popular in structural health monitoring because they can detect damage in large and complex structures. This literature research work presents a review of the techniques of vibration-based damage detection. Section 2.1.2 presents a comprehensive discussion on the damage detection methods based on various modal parameters. Section 2.1.3 reviews a novel modal analysis technique named impact-synchronous modal analysis, which would be prospective in extracting dynamic features for damage identification during the in-service condition. Section 2.1.4 discusses different machine learning techniques used in damage detection. The summary of the review and research problems are included in section 2.1.5.

2.1.2 Vibration-based damage detection techniques using modal parameters

The fundamental principle of vibration-based damage detection is that structural damage leads to alterations in the physical properties like stiffness, mass and damping. Consequently, the changes in the modal parameters of the system will also be observed. As the modal parameters obtained by modal analysis offer promising alternatives for damage detection, they can be regarded as damage indicators and used to detect the initiation and development of fatigue damage. In this section, damage detection methods based on various modal parameters are discussed.

2.1.2.1 Natural frequency

Damage usually leads to a decrease in the natural frequency, which is mainly attributed to the reduction of the structural stiffness. The correlation between damage and the natural frequency change can therefore be used in structural health monitoring and damage detection. As a global modal property of the structure, the natural frequency is easy to acquire and the measurement error is also much smaller than that of other modal parameters (e.g. the mode shape). Thus, structural damage detection based on natural frequency change is convenient to carry out. Cawley and Adams (1979) simulated a single damage condition of the structure and applied the natural frequency change to localize the damage. Hearn et al. (1991) found that the ratios of the changes in natural frequencies normalized with respect to the largest frequency change are independent of severity for small deterioration and can be directly used to indicate the location of structural damage. Morassi and Rovere (1997) used an optimality criterion to locate the notch of a steel frame by matching the first few natural frequencies, and pointed out the importance of some working hypotheses in damage identification. The natural frequency of the structure is advantageous in that it is independent of the choice of the position of the measurement point as a global property of a structure. Meanwhile, its shortcomings are summarized as follows. First, the natural frequency reflects the global characteristics of the structure, which is not sensitive to local damage (Hou & Xia, 2021). Second, the change in the natural frequency does not always specially indicate a specific location of the damage, for instance, the natural frequency cannot make a judgment on the location of damage when it occurs at two symmetrical positions (Salawu, 1997). Third, natural frequencies of lower modes are usually not sensitive enough to small cracks, and sometimes even remain unchanged when small damage occurs. On the other hand, although natural frequencies of higher modes reflect small damage information, they are difficult to

measure in real practice. These issues consequently affect the effectiveness and practicability of damage identification.

2.1.2.2 Mode shape

The mode shape is more sensitive to damage compared with the natural frequency. Damage identification based on mode shape change is advantageous in determining the location of damage, for the mode shape can reflect the changes in the displacement at the corresponding position of the structure. Sensitive damage indicators have been constructed using the vibration mode shape in previous studies, such as the modal assurance criterion (MAC) and the coordinate modal assurance criterion (COMAC). The MAC value describes the global similarity of two mode shapes while the COMAC is a pointwise measure of the difference between two mode shapes (Carden & Fanning, 2004). The MAC was used to reflect the mode shape change in Srinivasan and Kot's work (1992). It was found that this mode shape based feature was more sensitive to damage than natural frequencies for a shell structure. In Baghiee et al.'s study (2009) on the damage of the reinforced concrete beam specimens, the efficiency of MAC and COMAC methods was investigated. The results showed that MAC can reflect the overall stiffness change of the structure but cannot determine the stiffness changes in each degree of freedom (DOF). Meanwhile, COMAC may detect the changes in beam stiffness at DOF, and is rather able to detect, locate or quantify damage and effectiveness of strengthening. Although the mode shape based methods are more effective for detecting local damage, there are still some deficiencies. The change in the mode shapes is sometimes masked by measurement errors, which may cause fault alarms in the structural damage identification. The modal data acquired can be insufficient due to a limited number of measurement points, while a large number of measurement points can be uneconomical or impractical. The change in the mode shape caused by structural damage is more obvious in the higher-order modes, which, however, is difficult to measure with high accuracy in real practice.

2.1.2.3 Mode shape derivatives

The mode shape derivatives can be applied to damage detection as an alternative to the direct use of the mode shape. Pandey et al. (1991) introduced the mode shape curvature, which is the second derivative of the mode shape, to damage detection for the first time. The finite element models of cantilevered and simply supported beams were established and the changes in mode shape curvatures were studied by numerical simulation. Chance et al. (1994) found that numerically calculating curvature from mode shapes may cause unacceptable errors, and better results were achieved when the mode shape curvature was directly obtained through the measured strain. Baghiee et al.'s study (2009) showed that the curvature-based COMAC values appeared to be more precise in identifying crack zones in reinforced concrete beams than other methods. Yet, the accuracy relies on the technique used in calculating the curvatures and denoising of the experimental data. J. Maeck et al. (1999) proposed that the stiffness can be directly obtained from measured modal displacement derivatives, based on which the damage location and intensity can be predicted. In Z. Ismail et al.'s work (2006), a local stiffness indicator was constructed using the fourth derivative of the mode shape based on the equation of the Euler beam, and was used to locate the damage in reinforced concrete beams.

2.1.2.4 Strain energy

The modal strain energy (MSE) change is also used in damage detection. The MSE is formed by the product of the stiffness matrix and the second power of mode shape, which incorporates the system vibration behavior and physical properties (S. Q. Wang & Xu, 2019). Therefore, the MSE can also be used to indicate structural damage. Kim and Stubbs (1995) used a damage indicator based on the ratio of MSE of elements before and after the damage to locate and size damage in an experimental plate girder. Shi and Law (1998) developed a scheme to locate damage based on comparing MSE in each structural element before and after the occurrence of damage. However, the performance was

greatly influenced by measurement noise and incompleteness of measured modes. A damage identification scheme with damage localization and quantification using MSE change was proposed afterwards (Shi et al., 2000). It was reported that the results of single damage quantification were satisfying, whereas those of multiple damage quantification were not good under the same noise level. Guo and Li (2014) proposed a modal strain energy equivalence index for damage detection, which is based on the energy equivalence theory that the change in MSE and the energy dissipation caused by damage should be equivalent. In Dewangan et al.'s work (2020), the strain energy method was applied to damage detection in a wind turbine gearbox.

2.1.2.5 Frequency response function

Frequency response refers to the quantitative measure of the output spectrum of a system or device in response to a stimulus. FRF describes the correspondence between the input and output of the system at different frequencies, and is generally expressed in the form of complex functions. Compared with other dynamic features, FRF, as upstream modal data, is acquired directly in real time from the vibration transducer and then fast-Fourier transform (FFT). On the other hand, the modal extraction process of other modal parameters may affect the credibility of the results and prone to more errors because these modal parameters are originally retrieved from the raw FRFs. Therefore, the damage detection methods which directly use the FRF can be beneficial. However, the challenge is that, although it is of rich information, the full-size FRF is usually difficult to be directly processed because of its large size. Also, the intuitive features of the FRF plot (e.g. the magnitude and abscissa of its peaks) sometimes are not that sensitive to low severity damage, which are not suitable for damage identification either. Mathematical processing is therefore necessary to reduce the dimension of data and obtain more sensitive features. Samman et al. (1994a, 1994b) have looked into four techniques in processing the waveform of FRF, namely the waveform chain code (WCC) method, the adaptive

template matching (ATM) method, the signature assurance criterion (SAC) method and the equivalent level of degradation system (ELODS) method. Experimental results showed that the WCC method performed well in detecting cracks in the laboratory bridge, and proves its effectiveness in extracting sensitive features. In recent years, more damage identification methods have been developed using FRF, incorporated with various algorithms, for instance, Park and Park (2003) proposed a damage localization technique, where a damage index was calculated using the incomplete FRF in certain frequency ranges. Zhou et al. (2017) used hierarchical clustering analysis and similarity measure in their damage detection approach. Li et al. (2011) developed a damage identification method combining PCA-compressed residual FRF and artificial neural networks to identify defects.

2.1.3 Impact-synchronous modal analysis

Generally, in vibration-based damage identification methods, modal parameters of a structure need to be extracted from the raw vibration signals at the first stage, which is known as structural modal analysis. Usually, modal analysis is carried out through EMA, where the parameters are identified using the collected input and output signals when artificial excitation is exerted. EMA has proved to be an effective method of extracting structural dynamic characteristics. However, considering that ambient noise in the working environment may lead to measurement error of FRFs, EMA can only be carried out on static structures. When the tested structure is in operation, the ambient excitation and random noise cannot be neglected, which differs significantly from laboratory conditions. This reduces the practicality of EMA, especially for tested machines with high downtime costs. The OMA was proposed as an alternative to the classic EMA. Instead of using artificial excitation devices, OMA makes use of the freely available ambient excitation caused by natural excitation sources on or near the test structure (Parloo et al., 2005). In this way, the test structure can remain in its operating condition during the test.

Compared with EMA, the knowledge of the input in OMA is replaced by the assumption that the input is a realization of a stochastic process. The disadvantages of OMA are also obvious. First, the excitation should satisfy some prior hypothesis, for example, submitting to the gaussian white noise model (Dackermann et al., 2014). Second, since the ambient forces that excite the structure are not measured, FRF, which is rich in information on the dynamics behavior of the system is no longer available due to lacking knowledge of input.

A novel method named impact-synchronous modal analysis (ISMA) (A. G. A. Rahman et al., 2011) was thus proposed, where the input force and output response can be measured when the system is in operation. When ISMA is performed while the machine is in the running condition, both the responses caused by cyclic loads and random noise are filtered out in the time domain, leaving only responses triggered by the impact hammer. This is achieved by utilizing the impact-synchronous time averaging (ISTA) prior to performing the fast Fourier transform (FFT) operation (A. G. A. Rahman et al., 2014; A. G. A. Rahman et al., 2011). In time block averaging of ISTA, each time block is initiated by the impulse generated from the force trace of the impact hammer. Taking a sufficient number of averages, the periodic responses caused by cyclic loads and ambient forces, which are non-synchronous in phase to time block, will diminish. Meanwhile, the synchronous component, namely the responses triggered by the impact hammer, will be preserved. The following modal parameter extraction procedure is the same as EMA.

ISTA was first proposed by Rahman et al. (2011) aiming to quickly increase the signal-to-noise ratio of the response obtained while the machine is in operation. Unlike the usual spectrum averaging which is done in the frequency domain after FFT, ISTA is essentially based on time-synchronous averaging where averaging takes place in the time domain

prior to the FFT operation. Yet, despite the similar averaging principle, ISTA is also different from the conventional time synchronous averaging techniques that are commonly used. In the conventional time synchronous averaging techniques, signal acquisition from a rotating machine is triggered at the same phase angle and the averaging process is expected to eliminate all the nonsynchronous and random components, only leaving behind the running speed component and its harmonics. However, ISTA is targeted at an opposite problem, for it aims to eliminate all the cyclic load components, the harmonics and random noise, which are nonsynchronous to the triggering impacts. Consequently, the waveform achieved from ISTA will only contain the response of the system to the impact force.

Some follow-up work has also been conducted so far in order to study the factors governing the performance of ISMA and improve the effectiveness of this technique. To summarize, it is found that the performance of ISMA is mainly affected by the following four factors. These factors are (1) the number of averages; (2) the phase synchronization effect between the response due to impacts and that due to cyclic load; (3) the windowing function and (4) the level of impact force (Chao et al., 2016; Lim et al., 2019).

It was pointed out that the exponential window is an effective way to minimize leakage and attenuate non-synchronous components and noises (Chao et al., 2016). On the other hand, with the information of the calculated cyclic force, a suitable impact force level that excites the structure could be previously decided before ISMA is performed. It was found that a better result of FRF estimation can be achieved when the exponential window with an appropriate decay rate in ISMA is used, together with a higher impact force. Yet, the impact force should be well below the non-linearity force limit (Chao et al., 2016).

To enhance the performance of ISMA, the frequency of the impacts should not synchronize with the frequency of the cyclic load. One feasible way to avoid phase

synchronization is to randomly perform impacts with a frequency that differs from the cyclic load. The effectiveness of averages taken in determining the modal parameters of a motor-driven structure was demonstrated. It was shown that the responses caused by the cyclic load can be evidently removed by increasing the number of averages. This is because the random impacts make the phase angles of the cyclic components take random values in different time blocks. With the number of averages increasing, the cyclic components are more likely to be offset by averaging operations because of the randomness of phase angles. Consequently, phase synchronization is more likely to be attenuated. However, (A. G. A. Rahman et al., 2014) also pointed out that a large number of impacts may be needed in ISMA for the FRF estimation and modal parameter determination of the system, especially when the running speed is close to the natural frequency so that the cyclic load component is dominant because of resonance. This will cause ISMA to have limitations in practical applications. The main reason for the limitation is that the phase angle distribution is the lack of control with the manual impact hammer. To handle this problem, an auto impact device was introduced (Ong et al., 2018), which realized the control of impact timing. This device can apply impacts at controlled time intervals so that the impacts are avoided in synchronization with the responses from the cyclic load components. With a minimal number of impacts, all the responses contributed by unknown sources of the force contained in the acceleration response are filtered out when the phase of the periodic responses is not consistent with the impact signature for every impact applied. Thus, synchronization of phase between impacts and components is avoided through the use of the auto impact device to enhance the estimation of FRF (Lim et al., 2018; Ong et al., 2018).

ISMA has been tested in the real industry application by Rahman et al. (2013), performed on a diesel fuel pump package at an offshore platform in Malaysia to investigate the high vibration problem of the package. The instrumentation and

procedures used in the real industry application were similar to those in the laboratory condition. The only difference was that the impact hammer was replaced with a larger size model in the test. The modal parameters, namely natural frequencies, mode shapes, and damping of the pump were successfully determined using ISMA, without shutting down the pump. It was found that the excitation frequency was close to the natural frequency, which caused the resonance of the structure. Their study proved the feasibility of ISMA in solving practical problems.

As ISMA is a newly developed technology, its application in the field of engineering has yet to be explored. Nevertheless, considering its good performance in the previous experimental studies, it may have a good prospect. Specially, in damage identification problems, ISMA can be applied to extracting the dynamic features that are used as damage indicators.

2.1.4 Machine learning in damage identification

In the past decades, machine learning techniques have received wide acceptance for damage identification (Hossain et al., 2017), which is often incorporated with various damage indicators..

Supervised learning is the most commonly used in the training of artificial neural networks that solve pattern classification problems in damage identification. If the samples in N -dimensional Euclidean space need to be divided into M categories, the classification problem can be mathematically described as: to divide the N -dimensional Euclidean space into M decision regions so that the samples sharing some common features are classified into the same category. The manually defined discriminant function is conventionally used in classification problems, which, however, can be rather difficult to construct in complex situations. Meanwhile, artificial neural networks (ANNs), which are inspired by human biological neural networks and can learn to improve their

performance from experience, can be employed as an alternative. Taking the typical back-propagation (BP) network as an example, in damage identification problems, the network is trained using a set of labeled training samples (i.e. the selected damage indicators labeled with the corresponding damage states), and the trained network will have the ability to identify the damage scenarios when the damage indicators of new samples are input to it. This idea is shared in many specific supervised learning methods, such as the multi-layer perceptron (MLP), convolutional neural network (CNN), radial basis function (RBF) network, etc.

ANN has gained popularity in damage detection since the 1990s. Elkordy et al. (1994) used a BP network to identify the damage of a five-layer, three-dimensional frame structure by using the variation of mode shapes, which is one of the earliest applications. The MLP neural network was adopted by Rhim and Lee (1995) in their identification scheme. Hadzima-Nyarko et al. (2011) also used MLP neural network to investigate the relationship between the structural parameters and the damage ratio coefficient, for examining the damage level of a bridge. In the early studies, the location and severity of damage were simultaneously identified. In order to accurately identify the damage states, it is necessary to include a variety of damage severities for each possible damage location as training samples. The early schemes suffered from the high diagnostic complexity of large-scale structures, which reduced the training efficiency and accuracy of the neural network. Therefore, the hierarchical identification strategy was proposed; that is, to identify the occurrence, location and extent of damage using different networks in steps. Chen and Kim (1994) used two neural networks in their research; one for identifying the occurrence of damage, and another for determining the location of the damage. Ni et al. (2002) applied the hierarchical identification strategy to monitoring a suspension bridge, which examined the damage location first, and examined the damage severity at the identified location afterwards.

Although supervised learning can classify the damage states of a structure accurately and effectively, it also has disadvantages. It is noted that the labeled training data are necessary for supervised learning methods. However, it is difficult to obtain the complete training samples of all damage scenarios in many practical applications, which limits the application of supervised learning methods. Meanwhile, the unsupervised learning methods help to find previously unknown patterns in the data set without pre-existing labels. The outlier detection, or known as anomaly detection, is usually applied to unlabeled data to identify the items in the dataset that are different from the normal ones (Bull et al., 2019; Goldstein & Uchida, 2016; Zimek & Schubert, 2017). The outlier discordancy of a potential outlier, probably yielded by different mechanisms compared with the rest in the data set, is calculated and compared with a statistically determined threshold to decide whether it is an outlier or not (Rehman et al., 2011). Some studies have adopted outlier analysis for damage detection (Ulriksen et al., 2015; Worden et al., 2000). Cluster analysis is another typical unsupervised learning method that is often used. Park et al. (2008) adopted the k-means clustering pattern recognition algorithm in their electromechanical impedance-based wireless SHM system. Zhou et al. (2017) used hierarchical clustering analysis and similarity measure in their damage detection approach. However, these previous studies utilizing unsupervised learning focused more on detecting the existence of damage instead of identifying the specific damage state. Also, the number of classes usually needs to be previously defined in the classic clustering algorithms, which has limited their practicality in real life applications. A new hierarchical clustering method based on complex network theory was thus proposed and developed by Newman and Girvan (2004), Newman (2004) and Zhang et al. (2013), which has the ability to discover the community structure in networks and divide them into densely connected clusters. The modularity Q is defined to evaluate the quality of network division and is maximized in the process of hierarchical clustering. The

clustering process is automatically terminated when the modularity reaches its maximum, and the clustering result will be obtained. Thus, it may have its potential in vibration-based damage identification practices.

Machine learning has also been used to extract damage-sensitive features. This process is called feature learning. Feature learning seeks for transformations of the raw data as the representations needed for required tasks (e.g. detection or classification) from raw data (Janssens et al., 2016). Principal component analysis (PCA) is such an example. PCA transforms a set of variables in the vector space into a set of linearly uncorrelated variables called principal components by orthogonal transformation and is often used for feature component extraction and dimensionality reduction of high-dimensional data (Ma et al., 2019). Zang et al. (2001) employed PCA in their damage detection method to compress the full-size FRF data and construct the input to artificial neural networks. Li et al. (2011) used PCA to compress the residual FRF, which is the difference in the FRF data from the intact and the damaged structure. Besides PCA, some other feature learning methods have started to be applied in damage identification in recent years. For example, Wang et al. (2018) applied dictionary learning in bearing fault detection, illustrating that more descriptive features can be learned from the raw data. CNNs were used by Janssens et al. (2016) and the results indicated that, compared with using manually engineered features, better results were achieved with their CNN model. Lin et al. (2017) also used deep CNNs for automatic feature extraction. It is noted that feature learning was proven to work well for noisy signals, as less important information in the raw signal is omitted. Cao et al. (2017) used auto-associative neural networks (AANNs) in their study, which functioned as a nonlinear principal component analysis tool to extract damage features. Results showed that their damage identification scheme was of robustness against noise.

2.1.5 Summary

In this section, a comprehensive literature review of the existing vibration-based damage detection methods, impact-synchronous modal analysis and damage identification methods based on machine learning techniques is presented.

During the last decades, efforts have been made to develop vibration-based damage identification schemes using various modal parameters. These methods have shown promising results and are still under fast advances. Yet, limitations have also been observed in the classic modal parameter-based methods. For example, the natural frequency cannot always specially indicate a specific location of the damage and is usually not sensitive to the low-severity damage. The processing procedure of mode shape-based methods is complicated, which may affect the credibility of the results and prone to more errors. Compared with other dynamic features, damage identification directly using FRFs can be advantageous mainly in two aspects. First, FRF is directly acquired in real time from sensor hardware with FFT. Second, FRF is rich in modal information and many modal parameters are originally retrieved from the raw FRFs. However, mathematical processing is needed for dimension reduction of raw FRF data and extracting more sensitive features, which is still an issue to be studied.

Currently, EMA and OMA are two main techniques that are used to extract modal parameters. However, the lack of knowledge of the input forces in OMA does affect the accuracy of parameters extracted, and FRF is no longer available in this method. Meanwhile, EMA can only be carried out in the static condition, which limits the application scope of the current damage identification methods using FRF. A novel method named ISMA was thus developed, which makes it feasible to extract FRFs when the system is in operation. The ISMA technique has proved to be effective in obtaining FRFs and other modal parameters from running machines. Therefore, it is prospective in

the development of a real-time damage identification scheme for continuous structural health monitoring.

The machine learning techniques applied to damage identification have also been reviewed in this chapter. A considerable amount of research has been carried out over the years, covering both fields of supervised learning and unsupervised learning. In supervised learning, the neural network is trained using a set of labeled training samples, and the trained network will have the ability to identify the location and the extent of the damage. The large size of raw FRF data leads to a large number of sensors hardware and input nodes in the neural network, which is less cost-effective and computationally efficient and sometimes may cause problems of training convergence. To handle this problem, the FRF changes in some selected frequency ranges are used as the input features to reduce the input size of the network. The optimization of measurement points in terms of sensors hardware used can be further achieved to make the supervised damage identification scheme more cost-effective.

Meanwhile, the unsupervised learning methods help to find previously unknown patterns in the data set without pre-existing labels. Single FRF may not be effective sometimes while FRFs with multiple measurement points are too complex. It is noted that PCA is an effective tool for dimensional reduction and can help to compress the multiple FRFs while preserving important dynamic characteristics at the same time. Besides, the WCC characterizes a waveform by its scaled relative slope and curvature and performs well in detecting cracks in the laboratory bridge and proves its effectiveness in extracting sensitive features. Specially, a new hierarchical clustering method based on complex network theory can discover the community structure in networks and automatically determine the number of clusters, which gains an advantage over conventional clustering algorithms where the number of clusters needs to be predefined. WCC analysis can be

used to further extract a more damage-sensitive feature from the PCA-reduced FRF and then classified using the hierarchical cluster analysis to develop a sensitive and automated damage detection system. The work can be further enhanced through the post-screening of the alarmed damage state to develop a complete operational damage identification scheme.

2.2 Background theories

The theoretical background is illustrated in this section. 2.2.1 introduces the principle of ISMA and explains how the FRF is obtained with this method. 2.2.2-2.2.4 are the signal processing methods applied to extracting FRF damage features in this work. 2.2.5 and 2.2.6 introduces the two machine learning algorithms used in this work, namely the supervised BP network and the unsupervised hierarchical clustering.

2.2.1 FRF measurement using ISMA

The dynamic equation of a system with n DOF is given by

$$\mathbf{M}\ddot{\mathbf{x}}(t) + \mathbf{C}\dot{\mathbf{x}}(t) + \mathbf{K}\mathbf{x}(t) = \mathbf{f}(t) \quad (2.1)$$

\mathbf{M} , \mathbf{C} , \mathbf{K} are $n \times n$ matrixes and they represent the mass, damping and stiffness matrices respectively. The n -dimensional vector $\mathbf{f}(t)$ is the external force. $\mathbf{x}(t)$, $\dot{\mathbf{x}}(t)$ and $\ddot{\mathbf{x}}(t)$ are the n -dimensional structural displacement, velocity and acceleration vectors respectively.

Fourier transform is conducted to transform the dynamic equation from the time domain to the frequency domain as

$$(-\omega^2\mathbf{M} + j\omega\mathbf{C} + \mathbf{K})\mathbf{X}(\omega) = \mathbf{F}(\omega) \quad (2.2)$$

where ω refers to the frequency. The FRF matrix $\mathbf{H}(\omega)$ is defined as

$$\mathbf{H}(\omega) = (-\omega^2 \mathbf{M} + j\omega \mathbf{C} + \mathbf{K})^{-1} \quad (2.3)$$

so that

$$\mathbf{X}(\omega) = \mathbf{H}(\omega)\mathbf{F}(\omega) \quad (2.4)$$

The element of the x -th row and y -th column of the FRF matrix indicates the acceleration response of the x -th DOF when a unit excitation is exerted on the y th DOF. The existence of damping causes the elements of the FRF matrix to be complex numbers, which can be expressed in the form of magnitude and phase. In the real practice, this transformation of signals from the time domain to the frequency domain is usually implemented by FFT algorithm.

In the operation of ISMA, ISTA is performed on the time-domain signals directly obtained from the sensors before FFT. The impacts are created by the automated impact device with a time interval T_0 . The sampling of the signal is triggered by the impact force input to the analyzer. The process of ISTA is mathematically described as

$$x^{avg}(t) = \frac{1}{N} \sum_{k=0}^{N-1} x(t + kT_0) \quad (2.5)$$

where $x^{avg}(t)$ is the averaged vibration signal in time domain, N is the total number of impacts, $x(t)$ is the vibration signal in time domain, k is the number of impacts and T_0 is the time interval between the impacts. The signal $x(t)$ can be represented as

$$x(t) = x^{ir}(t) + x^c(t) + x^n(t) \quad (2.6)$$

where $x^{ir}(t)$ is the impact response, $x^c(t)$ is the cyclic load with its harmonics and $x^n(t)$ is the random noise. Therefore,

$$x^{avg}(t) = \frac{1}{N} \sum_{k=0}^{N-1} x^{ir}(t + kT_0) + \frac{1}{N} \sum_{k=0}^{N-1} x^c(t + kT_0) + \frac{1}{N} \sum_{k=0}^{N-1} x^n(t + kT_0) \quad (2.7)$$

Since the trigger is synchronized with the repetition rate of the impact, the first item (i.e. the average of the impact response) will be preserved. Meanwhile, the second item (i.e. the running speed component), which is non-synchronized with the trigger, will be diminished by the averaging process, so will be the last item of random noise. Therefore, only the item of the impact response $\frac{1}{N} \sum_{k=0}^{N-1} x^{ir}(t + kT_0)$ will remain in ISTA, and the result is equivalent to the average of pure impact response signals.

Then the FFT is performed on the impact response obtained through ISTA using the averaged input signal to acquire the FRF of the test system, which follows the procedure of conventional EMA methods.

2.2.2 FRF change

Structural damage leads to alterations in the FRF. A straightforward way to describe this change is to directly calculate the absolute difference in the magnitude of FRF in a certain frequency interval. The measure of the FRF change δ is thus introduced to quantify this difference in comparison with the FRF measured at the undamaged state, which is defined as

$$\delta_i = \sum_{j=1}^m |h_i(\omega_j) - \tilde{h}_i(\omega_j)| \quad (2.8)$$

where $\{\omega_1, \omega_2, \dots, \omega_m\}$ is the equidistantly discretized sequence of the considered frequency range and $h_i(\omega_j)$ is the FRF magnitude of the i -th measurement point at the frequency ω_j . $\tilde{h}_i(\omega_j)$ is the FRF magnitude which is previous measured at the undamaged condition and functions as the reference.

2.2.3 PCA-reduced FRF

In order to obtain the global dynamic properties of the test structure, the modal analysis is often conducted with multiple measurement points, which leads to large size of FRF data. Performing PCA on multiple FRFs aims to reduce the data size while preserving principal modal information.

In this study, modal analysis is carried out with a fixed impact point and n measurement points at different locations. The FRF magnitude measured at the i -th measurement point is denoted as $\mathbf{h}_i = [h_i(\omega_1), h_i(\omega_2), \dots, h_i(\omega_m)]^T, i = 1, 2, \dots, n$. $\{\omega_1, \omega_2, \dots, \omega_m\}$ is the equidistantly discretized sequence of frequency and $h_i(\omega_j)$ is the FRF magnitude of the i -th measurement point at the frequency ω_j . The output of PCA-reduced FRF $\mathbf{p} = [p(\omega_1), p(\omega_2), \dots, p(\omega_m)]^T$ can be expressed as

$$\mathbf{p} = \sum_{i=1}^n \alpha_i \mathbf{h}_i \quad (2.9)$$

where $\boldsymbol{\alpha} = (\alpha_1, \alpha_2, \dots, \alpha_n)^T$ is a unit vector satisfying

$$\|\boldsymbol{\alpha}\| = \sqrt{\alpha_1^2 + \alpha_2^2 + \dots + \alpha_n^2} = 1 \quad (2.10)$$

\mathbf{p} is an m -dimensional vector and the j -th element is

$$p(\omega_j) = \sum_{i=1}^n \alpha_i h_i(\omega_j), \quad j = 1, 2, \dots, m \quad (2.11)$$

In PCA process, $\boldsymbol{\alpha}$ is determined so as to maximize the variance of the m elements of \mathbf{p} , that is,

$$\boldsymbol{\alpha} = \arg \max_{\boldsymbol{\alpha}} \sum_{j=1}^m \left(p(\omega_j) - \frac{1}{m} \sum_{j=1}^m \sum_{i=1}^n \alpha_i h_i(\omega_j) \right)^2 \quad (2.12)$$

According to the theories of PCA (Jolliffe & Springer-Verlag, 2002), α is the eigenvector corresponding to the maximum eigenvalue of the correlation matrix, which can be figured out through linear algebra methods. With the value of α obtained, \mathbf{p} is finally expressed by

$$\mathbf{p} = (\mathbf{h}_1, \mathbf{h}_2, \dots, \mathbf{h}_n) \alpha \quad (2.13)$$

In this study, the coefficient α will be computed in the beginning through the above method using a set of reference FRFs measured at undamaged state. Then \mathbf{p} of each sample will be calculated by matrix multiplication of Eq. (2.13) as the PCA-reduced FRF.

This procedure not only reduces the size of the original data but is also helpful for the following identification work. Here, a linear combination of all the FRF sequences with a larger variance is obtained. Linear combination means the resonant peaks will also be preserved. A larger variance of the PCA-reduced FRF usually means larger fluctuation of its curve and, in another word, the resonant peaks are more distinct. As these peaks carry some weightage of the dynamic characteristics of the system, the mode behavior in this PCA-reduced FRF could be then used in damage identification.

2.2.4 WCC analysis

The WCC reflects the changes in the scaled relative slope and curvature of some signal waveforms in comparison with a benchmark signal. Specially in this work, the WCC analysis would be performed on the PCA-reduced FRF $\mathbf{p} = [p(\omega_1), p(\omega_2), \dots, p(\omega_m)]^T$. To introduce the concept of WCC, the PCA-reduced FRF can be re-expressed as an equidistantly discretized signal $\mathbf{u} = (u_1, u_2, \dots, u_m)^T$ so that

$$u_i = p(\omega_i), \quad i = 1, 2, \dots, m \quad (2.14)$$

Similar to the definition of \mathbf{u} , the benchmark signal, denoted as $\tilde{\mathbf{u}}$, refers to the PCA-reduced FRF independently measured under the undamaged state. The slope $\mathbf{s} = (s_1, s_2, \dots, s_{m-1})^T$ of \mathbf{u} is defined by forward differencing as

$$s_i = u_{i+1} - u_i, \quad i = 1, 2, \dots, m - 1 \quad (2.15)$$

Denote the maximum value of slope as s_{max} . The elements of \mathbf{s} are then normalized into the scaled relative slope as $\mathbf{s}^{rs} = (s_1^{rs}, s_2^{rs}, \dots, s_m^{rs})^T$, and

$$s_i^{rs} = \frac{50 \times s_i}{s_{max}}, \quad i = 1, 2, \dots, m - 1 \quad (2.16)$$

s_i^{rs} is scaled to 50 so that the scaled relative slope range from -50 to 50. Then, the signal \mathbf{u} is compared with the benchmark signal $\tilde{\mathbf{u}}$ using the slope differential values, \mathbf{s}^{dv} , which are defined as follows

$$s_i^{dv} = |s_i^{rs} - \tilde{s}_i^{rs}|, \quad i = 1, 2, \dots, m - 1 \quad (2.17)$$

s_i^{dv} takes value in the range from 0 to 100. \tilde{s}^{rs} is the scaled relative slope of $\tilde{\mathbf{u}}$ and is derived with the same procedure of (2.15) and (2.16). The benchmark is regarded as the signal of the ‘standard state’ and functions as the reference for other signals. Once \mathbf{s}^{dv} is figured out, the area under the curve of slope differential value \mathbf{s}^{dv} , denoted as a_s can be calculated to quantify differences between the signal \mathbf{u} and the benchmark $\tilde{\mathbf{u}}$. Considering that \mathbf{s}^{dv} is an equidistantly discretized sequence, a_s can be computed as the sum of the series

$$a_s = \sum_{i=1}^{m-1} s_i^{dv} \quad (2.18)$$

a_s defined by (2.15)-(2.18) is regarded as the damage-sensitive WCC feature.

2.2.5 BP network

A typical three-layer BP network is employed in this work, which is shown in Figure 2.1. The network is composed of the input layer, hidden layer and output layer. In the input layer, each neuron corresponds to an input variable. The hidden layer is for computational purposes. Each of the output neurons computes an output variable. The neurons are connected to the neurons in the next layer by weights.

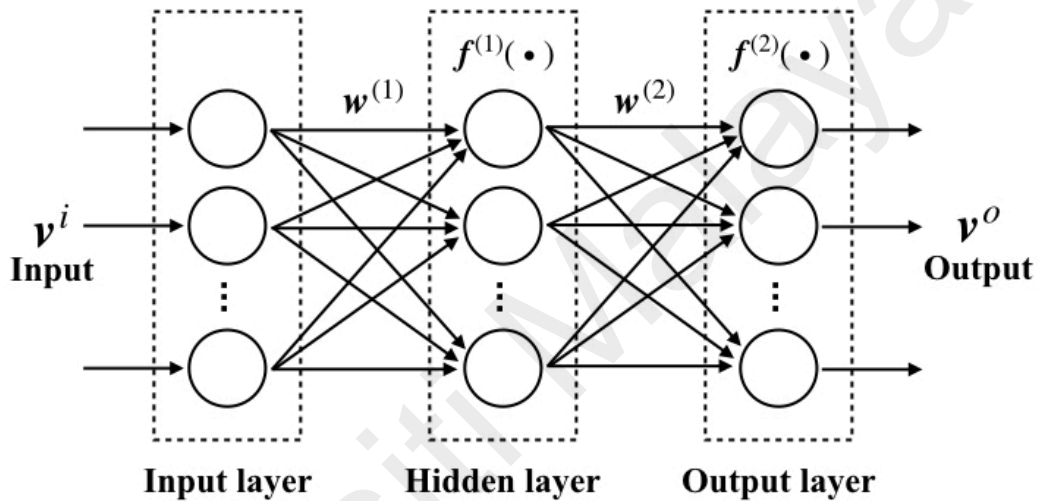


Figure 2.1: Structure of three-layer BP network

The back-propagation is a supervised learning algorithm for learning the weights of the BP network. The network is trained using pairs of input/target samples. Each pair includes an input vector v^i and the corresponding target vector v^t . As shown in Figure 2.1, $w^{(1)}$ is the weight matrix connecting the input layer and the hidden layer, and $f^{(1)}(\cdot)$ is the activation function of the hidden layer. $w^{(2)}$ is the weight matrix connecting the hidden layer and the output layer, and $f^{(2)}(\cdot)$ is the activation function of the output layer. The output of the network with respect to v^i is denoted as v^o . The BP learning algorithm consists of the forward propagation and the back-propagation procedures. In the forward propagation, the input signals pass from the input layer to the output layer via the hidden

layer. Considering the p -th pair of training sample $(\mathbf{v}_p^i, \mathbf{v}_p^t)$, the output of the hidden layer is

$$\mathbf{a}_p = \mathbf{f}^{(1)}(\mathbf{w}^{(1)}\mathbf{v}_p^i) \quad (2.19)$$

And the predicted output of the network can be written as

$$\mathbf{v}_p^o = \mathbf{f}^{(2)}(\mathbf{w}^{(2)}\mathbf{a}_p) \quad (2.20)$$

The loss of the model on this pair of the training sample is the cost of the difference between the output \mathbf{v}^o and the target \mathbf{v}^t , which is denoted as $L(\mathbf{v}^t, \mathbf{v}^o)$. The least square error and cross entropy are commonly used as the loss function. The overall performance on the training set is defined as

$$J = \frac{1}{N} \sum_{p=1}^N L(\mathbf{v}_p^t, \mathbf{v}_p^o) \quad (2.21)$$

where N is the total number of training sample pairs. The goal is to find the appropriate weights $\mathbf{w}^{(1)}$ and $\mathbf{w}^{(2)}$ to minimize J . To accomplish this goal, the back-propagation algorithm follows an iterative, gradient descent update rule (Brunton & Kutz, 2019; Goodfellow et al., 2016; Nielsen, 2015). In each iteration, $\mathbf{w}^{(1)}$ and $\mathbf{w}^{(2)}$ are respectively updated with increments of

$$\Delta \mathbf{w}^{(1)} = -\epsilon \nabla_{\mathbf{w}^{(1)}} J = -\frac{\epsilon}{N} \sum_{p=1}^N \nabla_{\mathbf{w}^{(1)}} J_p \quad (2.22)$$

$$\Delta \mathbf{w}^{(2)} = -\epsilon \nabla_{\mathbf{w}^{(2)}} J = -\frac{\epsilon}{N} \sum_{p=1}^N \nabla_{\mathbf{w}^{(2)}} J_p \quad (2.23)$$

ϵ is the learning rate which is determined by the specific learning methods and J_p is the value of $L(\mathbf{v}_p^t, \mathbf{v}_p^o)$. On the other hand, according to (2.19) and (2.20), the output of the network \mathbf{v}_p^o is computed as

$$\mathbf{v}_p^o = \mathbf{f}^{(2)} \left(\mathbf{w}_2 \mathbf{f}_1(\mathbf{w}^{(1)} \mathbf{v}_p^i) \right) \quad (2.24)$$

$\nabla_{\mathbf{w}^{(1)}} J_p$ and $\nabla_{\mathbf{w}^{(2)}} J_p$ can be computed based on the chain rule. Introduce the gradient of the input values of the output layer $\mathbf{g}_p^{(2)}$ as

$$\mathbf{g}_p^{(2)} = \nabla_{\mathbf{a}_p} J_p = \mathbf{f}^{(2)'} \odot \nabla_{\mathbf{v}_p^o} J_p \quad (2.25)$$

and the gradient of the input values of the hidden layer $\mathbf{g}_p^{(1)}$ as

$$\mathbf{g}_p^{(1)} = \mathbf{f}^{(1)'} \odot \left[\mathbf{w}^{(2)\top} \mathbf{g}_p^{(2)} \right] \quad (2.26)$$

where \odot is the Hadamard product of two vectors. $\mathbf{g}_p^{(1)}$ and $\mathbf{g}_p^{(2)}$ are known as error signals. It is noted that the error signals pass backward from the output layer to the hidden layer, and this is the so-called back-propagation. The gradient of the weights $\mathbf{w}^{(2)}$ and $\mathbf{w}^{(1)}$ are then computed by

$$\nabla_{\mathbf{w}^{(2)}} J_p = \mathbf{g}_p^{(2)} \mathbf{a}_p^\top \quad (2.27)$$

$$\nabla_{\mathbf{w}^{(1)}} J_p = \mathbf{g}_p^{(1)} \mathbf{v}_p^{i\top} \quad (2.28)$$

With the gradient of the weights obtained, the values of the weights can be updated according to (2.22) and (2.23). The next iteration starts with the updated weights of the network. The procedure continues until the stopping conditions are met.

2.2.6 Hierarchical cluster analysis based on complex network theory

The procedure of the hierarchical clustering based on complex network theory (Newman, 2004; Newman & Girvan, 2004; Zhang et al., 2013) is shown as follows. A vector set consisting of n elements $S = \{\mathbf{n}_1, \mathbf{n}_2, \dots, \mathbf{n}_n\}$ is considered. A complex network with n nodes is built based on the set S , where the vector \mathbf{n}_i is regarded as the coordinate of a node. n is the amount of the nodes in the network and, namely the total number of samples. \mathbf{n}_i ($i = 1, 2, \dots, n$) is the i -th node in the network. The weight of the edge between any two nodes in the network \mathbf{n}_i and \mathbf{n}_j , which shows the strength of connection, is defined as

$$w(\mathbf{n}_i, \mathbf{n}_j) = \begin{cases} \exp[-\sigma d(\mathbf{n}_i, \mathbf{n}_j)], & i \neq j \\ 0, & i = j \end{cases} \quad (2.29)$$

where $d(\mathbf{n}_i, \mathbf{n}_j)$ is the Euclidean distance between \mathbf{n}_1 and \mathbf{n}_2 . As $d(\mathbf{n}_i, \mathbf{n}_j) > 0$ when $i \neq j$, $w(\mathbf{n}_i, \mathbf{n}_j)$ takes value from 0 to 1, and the weight decreases when the distance between the nodes increases. Also, the weight of edge is strengthened for a smaller value of distance, which is determined by the positive strength parameter σ . In this study, σ takes the value of 50. When S is divided into r disjoint clusters, the partition is written as $\mathcal{C} = \{C_1, C_2, \dots, C_r\}$ such that $\bigcap_{i=1}^r C_i = S$. The community structure of the complex network is described by (S, \mathcal{C}) . The class similarity between any two disjoint clusters of nodes C_x and C_y ($1 \leq x \neq y \leq r$) is defined as

$$e_{xy} = \frac{L_{xy}}{L} \quad (2.30)$$

where

$$L = \frac{1}{2} \sum_{\mathbf{n}_i, \mathbf{n}_j \in C} w(\mathbf{n}_i, \mathbf{n}_j) \quad (2.31)$$

$$L_{xy} = \frac{1}{2} \sum_{\mathbf{n}_i \in C_x, \mathbf{n}_j \in C_y} w(\mathbf{n}_i, \mathbf{n}_j) \quad (2.32)$$

The class similarity matrix of the partition \mathcal{C} is defined as

$$\mathbf{e} = \begin{bmatrix} e_{11} & e_{12} & \cdots & e_{1r} \\ e_{21} & e_{22} & \cdots & e_{2r} \\ \vdots & \vdots & \ddots & \vdots \\ e_{r1} & e_{r2} & \cdots & e_{rr} \end{bmatrix} \quad (2.33)$$

It is noted that the class similarity matrix is symmetric. The modularity Q is then defined to evaluate the quality of network division as

$$Q = \sum_{x=1}^r \left[e_{xx} - \left(\sum_{y=1}^r e_{xy} \right)^2 \right] = \sum_x e_{xx} - \sum_x \left(\sum_y e_{xy} \right)^2 \quad (2.34)$$

Any change in the structure of the community will lead to the change in the class similarity matrix and the value of Q . High value of Q represents a good division and our goal is to optimize Q from possible divisions. The strategy follows the agglomerative hierarchical clustering algorithm, where each node starts in its own cluster, and pairs of clusters are merged upwards to form a binary, hierarchical cluster tree. Before talking about this algorithm, we first look into how the merging of clusters influences the value of Q . Suppose C_g is merged by $C_e, C_f \in \mathcal{C}$ so that $C_g = C_e \cup C_f$. Then

$$e_{gg} = \frac{L_{gg}}{L} = \frac{1}{L} (L_{ee} + L_{ff} + 2L_{ef}) = e_{ee} + e_{ff} + 2e_{ef} \quad (2.35)$$

For $x \neq e, f$

$$e_{xg} = \frac{L_{xg}}{L} = \frac{1}{L} (L_{xe} + L_{xf}) = e_{xe} + e_{xf} \quad (2.36)$$

Similarly,

$$e_{gx} = e_{ex} + e_{fx} = e_{xe} + e_{xf} = e_{xg} \quad (2.37)$$

Considering that the merger of the cluster C_e and C_f does not change the structure of the rest part of the network, the class similarity between any other clusters still remains unchanged. Thus, the increment of Q caused by the merging of C_e and C_f can be calculated by

$$\Delta Q_{ef} = 2e_{ef} - 2 \sum_x e_{xe} \sum_x e_{xf} \quad (2.38)$$

If the merger of the cluster C_e and C_f is effective, the modularity Q should increase after the merger, and that means $\Delta Q_{ef} > 0$.

In the initial state S , consisting of n nodes in total, is divided into q clusters and each cluster only includes one node. Then we repeatedly merge the clusters together in pairs, and choose the join that results in the greatest increase in the modularity Q as the final decision of this step; that is, in another word, maximizing the value of ΔQ among all the $n(n-1)/2$ possible ways of merger. The greatest increase of Q in this step is denoted as ΔQ_{max} . Now there are $n-1$ clusters left after the first merger. The merging step is then repeated until there is only one cluster left. ΔQ_{max} of each step is recorded. The progress of the algorithm can be represented as a dendrogram, a tree that shows the order of the joins. Cuts through the dendrogram at different levels give divisions of the network into larger or smaller numbers of clusters and we can select the best cut by looking for the maximal value of Q . In fact, with the procedure going on, ΔQ_{max} is positive at first, and then turns negative after the modularity Q reaches its maximum. Therefore, the dendrogram can be cut right before ΔQ_{max} turns negative and the best division of the network is obtained.

CHAPTER 3: METHODOLOGY

3.1 Introduction

In this chapter, the methodology of this work is elaborated. Section 3.2 introduces the research flow and the scope of this work. The experimental set-up is described in section 3.3, which includes the experimental equipment specifications, models and settings, etc. In section 3.4, the design of the experiment and procedures are explained in detail.

3.2 Research flow and scope

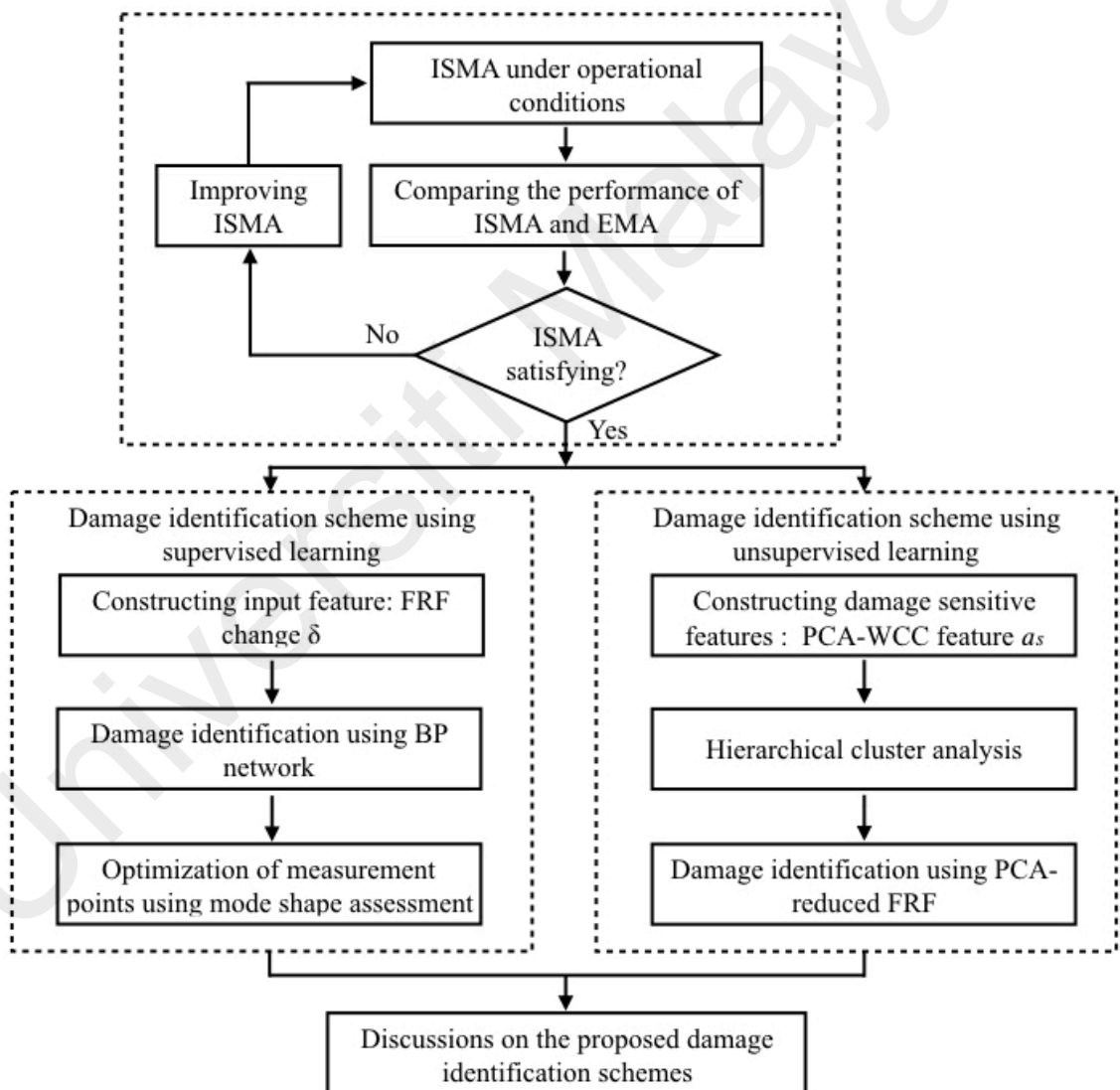


Figure 3.1: Flow chart

Following the main objectives as stated in Chapter 1, the study is mainly composed of three parts: (1) investigating the performance of ISMA in generating clean and stationary

comparable FRFs under the operational condition for damage identification; (2) development of an optimized operational damage identification scheme using FRF change and supervised machine learning; (3) development of an operational unsupervised damage identification scheme utilizing PCA-reduced FRFs and WCC analysis. The flow chart of this work is shown in Figure 3.1.

The ISMA was performed at the first stage to obtain the FRF and other modal parameters under the operational condition. The performance of ISMA was compared with that of EMA. The ISMA data would be further used for damage identification if they were verified to be static comparable.

In the supervised learning method, the input of the ANN was constructed by the FRF changes obtained from multiple measurement points, and the measurement points were then optimized by mode shape assessment. The FRF change is more informative than traditional modal properties such as the natural frequency because it makes use of modal information over a frequency range rather than at a certain frequency. However, it is noted that if the measurement point is located at the nodal point, the FRF curve will be relatively flat and the FRF change at that point cannot effectively reflect the damage. Therefore, it is more reliable to use multiple measurement points. If some measurement point fell on the nodal line, the damage could still be reflected by other measurement points. On the other hand, through mode shape assessment, it is possible to help us avoid placing the accelerometers at nodal points so as to optimize the number and locations of measurement points and make the supervised damage identification scheme more cost-effective in terms of hardware. The BP network was employed as the learning algorithm, which is one of the most effective and widely-used methods to solve classification problems. With the virtue of ISMA and FRF-based damage features, damage identification under the operation condition can be easily realized using this popular classification approach.

In the unsupervised learning method, features for hierarchical cluster analysis were extracted using PCA and WCC analysis. Performing PCA on FRF can not only reduce the size of the raw data, but also clearly preserve the resonant peaks of the original FRF curves, which contain rich modal information. WCC analysis, which is sensitive to the horizontal translation of peaks, helps to extract damage-sensitive features from the PCA-reduced FRF. Clustering of these features in terms of different damage scenarios were achieved by hierarchical cluster analysis based on complex network theory, which could automatically determine the number of clusters so that it did not need to be predefined. Then, the post-screening on the PCA-reduced FRF of the alarmed damage state helps to develop a complete operational damage identification scheme.

Additionally, the proposed damage identification methods based on supervised learning and unsupervised learning were compared and discussed.

3.3 Experimental set-up

A rectangular Perspex plate was investigated in this study to simulate the vibration behavior of an automobile, which is shown in Figure 3.2. The plate specimen has length, width and thickness of 480 mm, 200 mm and 9 mm, respectively, and weighs 1.1kg. The four corners of the plate were fixed to the aluminum supports, connected by two layers of steel sheets and screws. The FlexiForce A201 force sensors were placed between the two layers of steel sheets to measure the pressure attributed to the preload of the screws. The plate was symmetrically divided into nine points according to Figure 3.3. Five accelerometers (Wilcoxon Research model S100C) were placed at point #2, #4, #5, #6 and #8. The suspension/spring components of car wheels were simulated by the aluminum supports, where structural damage is assumed to take place and the sensors cannot be placed because of the existence of wheels. The automobile chassis can be modeled as a rectangular plate for the following reasons. First, the shape of a typical automobile chassis

is similar to that of a rectangular plate. Second, the ground supports simulate similar boundary conditions as those of the suspension/spring components of automobile wheels. Third, they show similar dynamic behaviors, the first three mode shapes of them are heaving, rolling and pitching. An automated impact device (AID) was used to create impacts at the edges of the plate and the ground support to analyze its dynamic behavior under the vertical impact from the automobile wheels. The AID was driven by the excitation voltage with a short period to automatically create periodic impacts towards the test system. EMA and ISMA were performed respectively under stationary and in-service conditions. The harmonic excitation was created by an electric motor and external power amplifier (LDS model PA25E) to simulate the in-service condition. National Instrument-Universal Serial Bus (NI-USB 9234) signal acquisition module was used to acquire dynamic signals from the accelerometers and LabVIEW 2013 was used for signal processing. The sampling rate was 2048 Hz and the block size was 4096 samples, which provided a frequency resolution of 0.5 Hz and data acquisition time of 2 seconds. ANNs were realized by MATLAB Neural Network Toolbox.

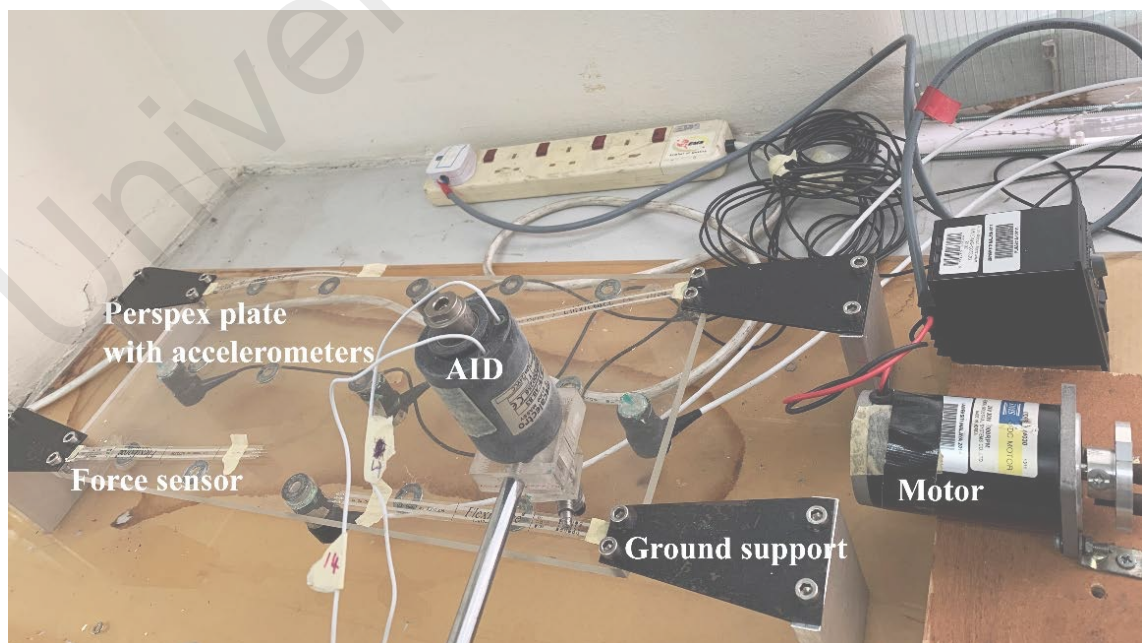


Figure 3.2: Experimental set-up

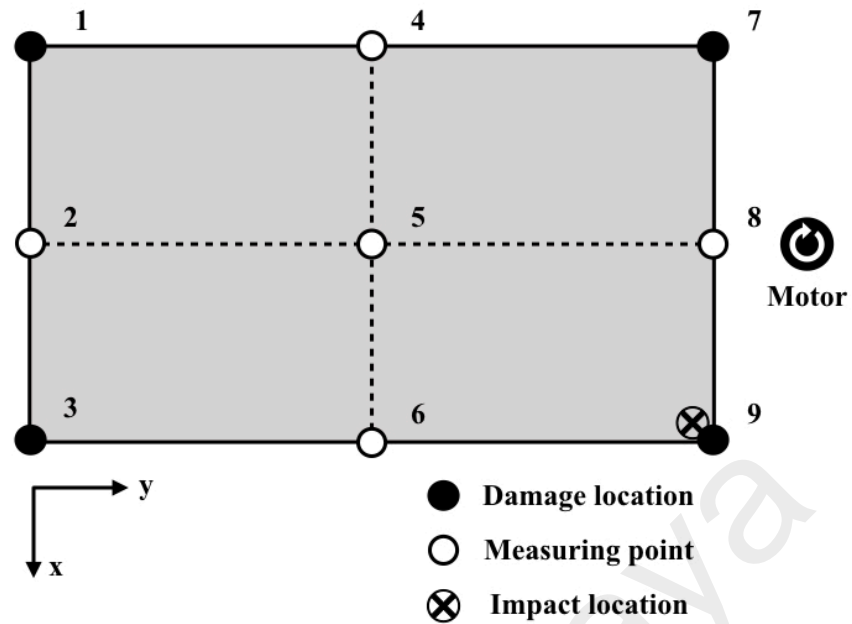


Figure 3.3: Measurement points, damage location and impact location

In this work, damage conditions were simulated by removing or loosening the corresponding screws that fix the plate to the ground support, and the force sensors helped quantitatively control the severity of damage. When the screws were loosened, the pressure between the steel plate and the Perplex plate also decreased. The reading of the force sensor, which was proportional to the pressure, also decreased. The force sensors were calibrated so that the sensor reading could reach the maximum 150 when the screws were firmly tightened. In the undamaged (UD) cases, all the four damage points were firmly screwed and the pressure of each point was 150. Three severity levels of damage were created, namely high damage (HD), moderate damage (MD) and low damage (LD) conditions. The LD conditions were created by slightly loosening the screws of the damage point so that the point was still screwed, yet with pressure of 40. It will be shown later that the damage can be clearly detected using the PCA-WCC features when the pressure is reduced to 40 or below. In the MD conditions, the screws were loosened to an extent that the pressure just reduced to 0. The HD conditions were created by removing

the screws of the damage point. As damage could occur at each corner of the plate, there were four potential damage points, namely points #1, #3, #7 and #9. Table 3.1 shows the list of all the scenarios along with their descriptions.

Table 3.1: List of damage scenarios and descriptions

Damage scenario	Description
UD	All four 4 points of the screws were tightened with pressure of 150
LD1	Screws at point #1 were slightly loosened with pressure of 40, as for points #3, #7 and #9 were tightened with pressure of 150
LD3	Screws at point #3 were slightly loosened with pressure of 40, as for points #1, #7 and #9 were tightened with pressure of 150
LD7	Screws at point #7 were slightly loosened with pressure of 40, as for points #1, #3 and #9 were tightened with pressure of 150
LD9	Screws at point #9 were slightly loosened with pressure of 40, as for points #1, #3 and #7 were tightened with pressure of 150
MD1	Screws at point #1 were loosened with 0 pressure, as for points #3, #7 and #9 were tightened with pressure of 150
MD3	Screws at point #3 were loosened with 0 pressure, as for points #1, #7 and #9 were tightened with pressure of 150
MD7	Screws at point #7 were loosened with 0 pressure, as for points #1, #3 and #9 were tightened with pressure of 150
MD9	Screws at point #9 were loosened with 0 pressure, as for points #1, #3 and #7 were tightened with pressure of 150
HD1	Screws at point #1 were removed, as for points #3, #7 and #9 were tightened with pressure of 150
HD3	Screws at point #3 were removed, as for points #1, #7 and #9 were tightened with pressure of 150
HD7	Screws at point #7 were removed, as for points #1, #3 and #9 were tightened with pressure of 150
HD9	Screws at point #9 were removed, as for points #1, #3 and #7 were tightened with pressure of 150

3.4 Design of experiment and procedures

3.4.1 Modal analysis using ISMA de-noising method under operational condition

ISMA was performed on a rectangular Perspex plate in this study. A harmonic excitation of 35 Hz was created by an electric motor and external power amplifier to

simulate the operational condition. ISMA was carried out using the AID with lab-scale linear solenoids and calibrated force transducer as input excitation. Accelerometers were used to measure the output response due to the impacts to obtain FRFs which are rich in information on the dynamic behavior of the plate. The number of averaging for ISTA was set as 10. In the experiment, the FRF data of the five measurement points (#2, #4, #5, #6 and #8) were collected with excitation at point #9. The FRFs in the frequency range of 0~100 Hz were saved with resolution of 0.5 Hz.

To evaluate the performance of ISMA, the FRF data measured using ISMA under the operational condition were qualitatively and quantitatively compared with those measured using conventional EMA method in the static state. Frequency response assurance criterion (FRAC) was used to describe the similarity between the two FRFs, which is defined as (Shin, 2016)

$$FRAC = \frac{|\{H^a\}^H \{H^b\}|^2}{(\{H^a\}^H \{H^a\})(\{H^b\}^H \{H^b\})} \quad (3.1)$$

where $\{H^a\}$ and $\{H^b\}$ are the equidistantly discretized sequences of the FRFs to be compared. FRAC ranges from 0 to 1 and high similarity is indicated when the value approaches 1.

Afterwards, the natural frequency and mode shape of the plate were respectively extracted from the EMA and ISMA FRF. Recall that there are no accelerometers deployed at the points #1, #3, #7 and #9, which means the FRF is not available at the corners of the plate. Nevertheless, the full mode shapes can still be obtained through interpolation using the displacement at the adjacent measurement points. Considering the first three common mode shapes of this type of structure are usually heaving, rolling and pitching, where there is no obvious bending effect, the points at the corners can be interpolated with the displacement of the three points adjacent to it. For example, with the assumption that the

points #1, #2, #4 and #5 are coplanar, the displacement of point #1 can be obtained by interpolation as

$$\Psi_1 = \Psi_2 + \Psi_4 - \Psi_5 \quad (3.2a)$$

where Ψ_x is the displacement at the point # x . In this way, the displacement of points #3, #7 and #9 can also be obtained as

$$\Psi_3 = \Psi_2 + \Psi_6 - \Psi_5 \quad (3.2b)$$

$$\Psi_7 = \Psi_4 + \Psi_8 - \Psi_5 \quad (3.2c)$$

$$\Psi_9 = \Psi_6 + \Psi_8 - \Psi_5 \quad (3.2d)$$

The mode shape of the plate, $\Psi = (\Psi_1, \Psi_2, \dots, \Psi_9)^T$, was thus available for the first three modes. The MAC was applied to describe the similarity between the mode shapes obtained by EMA and ISMA, which is defined as (Pastor et al., 2012)

$$MAC = \frac{|\Psi^{aH}\Psi^b|^2}{(\Psi^{aH}\Psi^a)(\Psi^{bH}\Psi^b)} \quad (3.3)$$

where Ψ^a and Ψ^b are the mode shapes to be compared. MAC ranges from 0 to 1 and high similarity between the compared mode shapes is indicated when the value approaches 1.

3.4.2 Development of operational damage identification scheme using supervised learning

A three-layer feed-forward back-propagation (BP) network was employed in the method proposed in this section. The input of the network was constructed using the FRF change at multiple measurement points.

The BP network was constructed with sigmoid hidden neurons and soft-max output neurons. The input vector of the network was constructed with the FRF changes of multiple measurement points, and each element δ_i corresponded to the FRF change of a the i -th measurement point as defined in (2.8). The one-hot vectors were used as the target vectors to indicate the corresponding damage scenario of each sample. The input size of the network corresponded to the number of the considered measurement points while the size of output layer corresponded to the total number of damage scenarios. The number of neurons in the hidden layer was set as 10. The performance of the network on any set of input-target samples was evaluated by cross-entropy, which is defined as

$$J = \frac{1}{N} \sum_{p=1}^N -\mathbf{v}_p^t \cdot \log \mathbf{v}_p^o \quad (3.4)$$

where N is the total number of input-target samples in the set, \mathbf{v}_p^t is the target of the p -th sample and \mathbf{v}_p^o is the output of the network with respect to the input of the p -th sample \mathbf{v}_p^i (Goodfellow et al., 2016).

The training samples were obtained by EMA. The 13 damage scenarios list in Table 3.1 were considered. A total of 140 sets of FRF data were measured using EMA, of which 20 sets were measured under the undamaged scenario and 10 sets were measured under each damaged scenario. Thus, there were 140 EMA input-target samples created with 13 classes. In the training process, 80% of the EMA samples were divided into the training set and the rest were divided into the validation set. Scaled conjugate gradient back-propagation was used as the training method of the network. The training was terminated when the performance gradient on the validation set reached 1.0E-06. The trained network was then tested using the ISMA testing samples. Similar to the acquisition of EMA samples, the 140 ISMA testing samples were obtained from FRF measured by ISMA and also included all the 13 damage scenarios. The testing results were evaluated

by the cross entropy and percentage accuracy. The cross entropy was calculated according to (3.4). The percentage accuracy of damage identification is defined as

$$\eta = \frac{\text{number of testing samples with correct results}}{\text{number of all testing samples}} \times 100\% \quad (3.5)$$

More detailed testing results were illustrated by confusion matrices. The confusion matrix summarizes the performance of a classification algorithm. It is a two-dimensional matrix. Each row of the matrix represents the objects the classifier assigns, while each column represents the objects in the actual class. It is easy to see whether the objects are mislabeled with the help of the confusion matrix. When the identified class is the same as the actual class, the classification is correct, otherwise the object is misclassified (Sammut & Webb, 2011).

The settings of the BP network are summarized in Table 3.2.

Table 3.2: Settings of three-layer BP network

Input layer	Number of neurons	Corresponding to number of measurement points
Hidden layer	Neuron type	Sigmoid hidden neurons
	Number of neurons	10
Output layer	Neuron type	Soft-max output neurons
	Number of neurons	Corresponding to number of damage scenarios to be classified
Training	Division of samples	Training set 80%, validation set 20%
	Performance	Cross-entropy
	Method	Scaled conjugate gradient back-propagation
	Stopping condition	Performance gradient on the validation set reached 1.0E-06

In this study, the frequency range for FRF change calculation was determined at the first stage with the reference of FRF figures. Then, all the five measurement points were used for training and testing the network, and the testing results were evaluated to verify the effectiveness of the proposed damage identification scheme. Afterwards, optimization of the measurement points was carried out with mode shape assessment. Finally, the scheme was tested and evaluated with the reduced number of measurement points.

3.4.3 Development of operational damage identification scheme using unsupervised learning

An unsupervised damage identification scheme is proposed in this section, combining PCA, WCC analysis and hierarchical cluster analysis based on complex network theory.

The feature extraction procedure is described as follows. First, PCA was conducted on the raw FRF data to obtain the PCA-reduced FRF. The dimension of the multiple FRF was thus reduced. Afterwards, WCC analysis was performed on the PCA-reduced FRF to calculate its sequence of slope differential values. The complete frequency range was then divided into several frequency segments in terms of the vibration modes. Finally, the WCC features, namely the areas under the slope differential value curves, were respectively calculated in these frequency segments. To further look into the sensitivity of the WCC analysis, the PCA-WCC features were compared with the shift of the corresponding resonant peaks under six levels of damage severities. The damage severity was determined by the preload of the screws at the damage points. Recalling that the pressure was 150 when the screws were completely tightened, the screws at the damage point were loosened so that the pressure respectively reduced to 120, 100, 80, 60, 40 and 20. In this way, six levels of low-severity damage were thus created.

The hierarchical cluster analysis based on complex network theory was applied as the unsupervised learning method in this work, which can automatically divide data points

into densely connected clusters without previously setting the number of clusters. A total of 140 sets of FRF data were measured using ISMA under 13 damage scenarios as shown in Table 3.1, of which 20 sets were measured under the undamaged scenario and 10 sets were measured under each damaged scenario. The full frequency range was divided into several frequency segments in terms of the vibration modes. The damage-sensitive PCA-WCC features were obtained from the ISMA FRF data in each frequency segment and normalized as

$$a_{s \text{ norm}} = \frac{a_s}{a_{s \text{ max}}} \quad (3.6)$$

where $a_{s \text{ max}}$ is the maximum of a_s among all the samples. The normalized PCA-WCC features of all the selected segments were combined into a vector, which was regarded as the coordinate of a node in a complex network. Hierarchical clustering was then conducted to sort the nodes of samples into several categories, automatically finding the number of clusters by maximizing the modularity Q to execute the damage detection scheme.

The clustering results of the new hierarchical clustering method were compared with those of the conventional k-means clustering. The adjusted Rand index (ARI) was used as the measure of agreement between the clustering results and the actual classes of samples. Given a set of samples S with n elements, suppose $\mathcal{X} = \{X_1, X_2, \dots, X_r\}$ is the partition of S based on the actual classes of samples and $\mathcal{Y} = \{Y_1, Y_2, \dots, Y_s\}$ is the clustering result such that $\bigcap_{i=1}^r X_i = \bigcap_{j=1}^s Y_j = S$ and $X_i \cap X_{i'} = Y_j \cap Y_{j'} = \emptyset$ ($1 \leq i \neq i' \leq r, 1 \leq j \neq j' \leq s$). Let n_{ij} be the number of samples that both belong to the class X_i and the cluster Y_j , and let a_i and b_j be the number of objects in the class X_i and the cluster Y_j respectively. The notations are shown in Table 3.3.

Table 3.3: Notation for comparing two partitions

$x \backslash y$	Y_1	Y_2	\dots	Y_r	Sums
X_1	n_{11}	n_{12}	\dots	n_{1r}	a_1
X_2	n_{21}	n_{22}	\dots	n_{2r}	a_2
\vdots	\vdots	\vdots	\ddots	\vdots	\vdots
X_s	n_{s1}	n_{s2}	\dots	n_{sr}	a_s
Sums	b_1	b_2	\dots	b_r	n

Then the ARI is calculated as (Hubert & Arabie, 1985)

$$ARI = \frac{\sum_{ij} \binom{n_{ij}}{2} - [\sum_i \binom{a_i}{2} \sum_j \binom{b_j}{2}]/\binom{n}{2}}{\frac{1}{2} [\sum_i \binom{a_i}{2} + \sum_j \binom{b_j}{2}] - [\sum_i \binom{a_i}{2} \sum_j \binom{b_j}{2}]/\binom{n}{2}} \quad (3.7)$$

ARI $\in [-1,1]$ and a larger value means that the clustering result is more consistent with the real classes.

Any alarmed damage state was diagnosed for its damage severity and location through PCA-reduced FRFs and corresponding mode shapes. Then further observation and analysis were carried out on the PCA-reduced FRF of the plate-like structure. As the PCA-reduced FRF has similar resonant peaks to the common FRFs, the shift in the abscissa and the magnitude of the peaks were discussed. The relation between the change in the resonant peaks and the damage states was studied with the reference of mode shape assessment to develop a complete operational damage identification scheme.

CHAPTER 4: RESULTS AND DISCUSSION

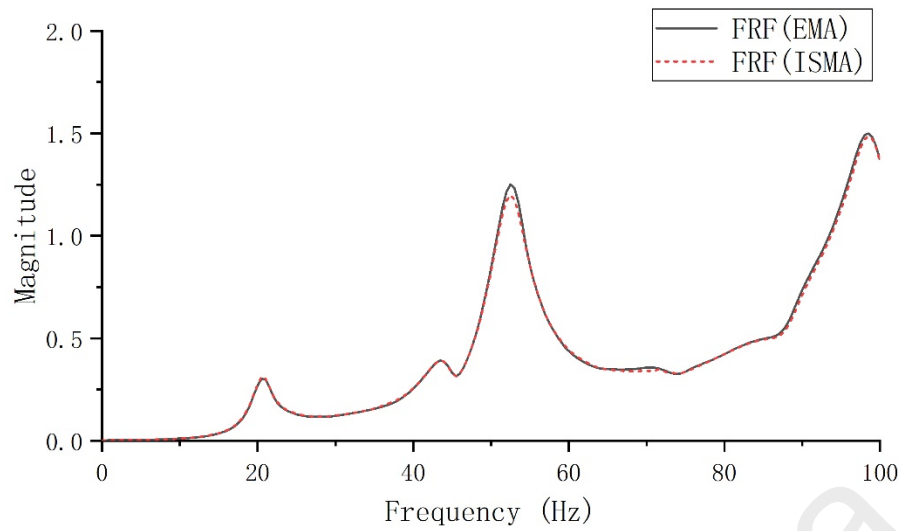
4.1 Introduction

This research was conducted according to the proposed procedures described in Chapter 3, and the results are presented accordingly in this chapter. Section 4.2 shows the results of the modal analysis using ISMA under the operational condition. The performance of ISMA is compared with that of EMA. Section 4.3 presents the results of the operational damage identification scheme using supervised learning. The scheme is evaluated with the reduced number of measurement points with optimization of the measurement points carried out through mode shape assessment. Section 4.4 presents the results of the operational damage identification scheme using unsupervised learning, which includes the results of the hierarchical clustering and further analysis on the PCA-reduced FRF of the plate-like structure. Section 4.5 is the comparison between the supervised learning and unsupervised learning methods developed in this work. The results in each section are elaborated and discussed throughout this chapter.

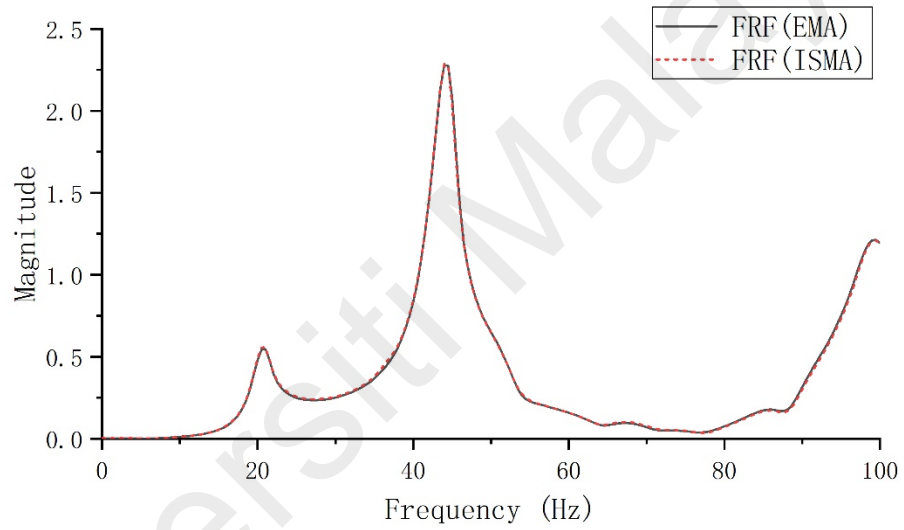
4.2 Modal analysis using ISMA de-noising method under operational condition

4.2.1 Measurement of FRF using ISMA under operational condition

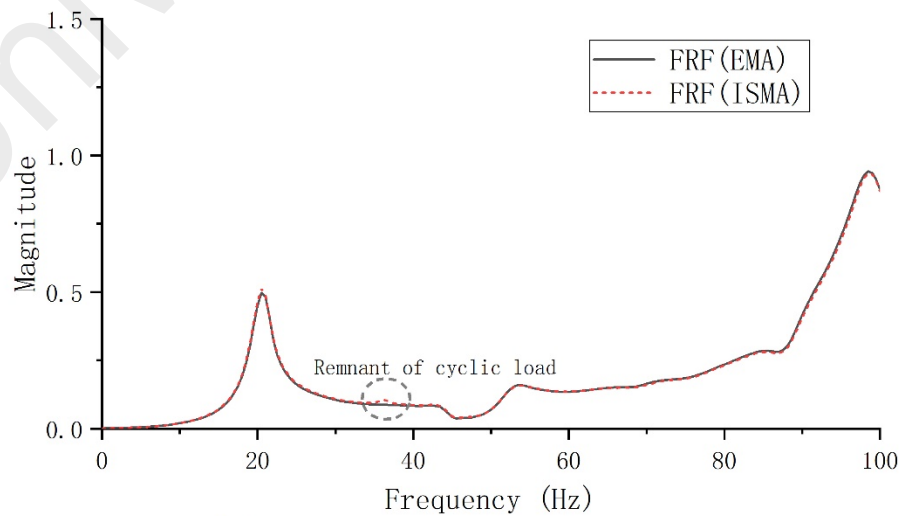
Modal analysis was respectively conducted under stationary condition using EMA, and under in-service condition using the ISMA de-noising method. The FRFs measured using EMA and ISMA under the undamaged scenario are compared in Figure 4.1 as an example.



(a) FRFs measured at point #2 in UD

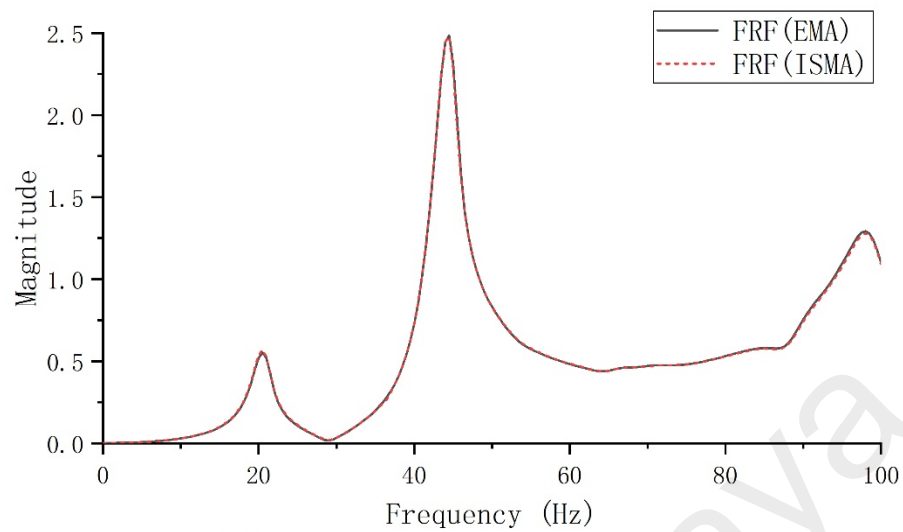


(b) FRFs measured at point #4 in UD

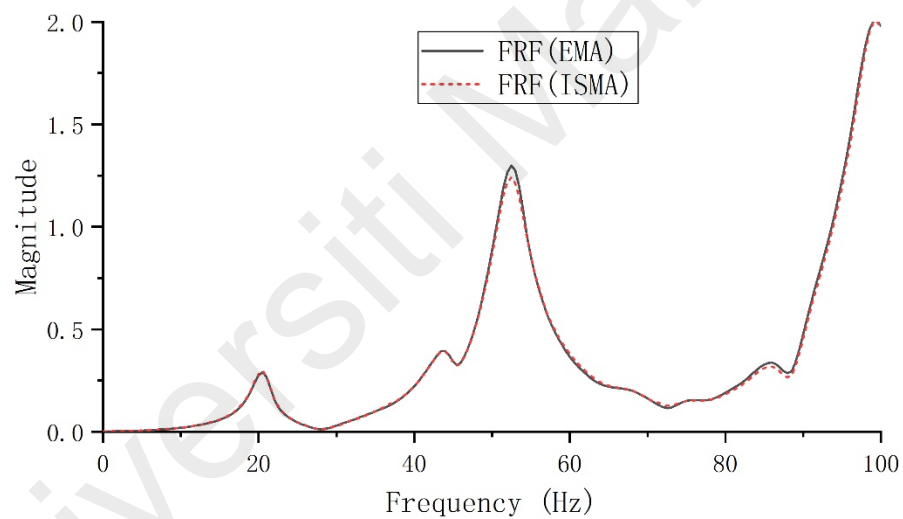


(c) FRFs measured at point #5 in UD

Figure 4.1, continued



(d) FRFs measured at point #6 in UD



(e) FRFs measured at point #8 in UD

Figure 4.1: EMA and ISMA FRFs measured in UD scenario

It is observed from Figure 4.1 that the frequency range 0~100 Hz covers the first three vibration modes and part of the fourth mode, which are respectively near 20 Hz, 44 Hz, 53 Hz and 98 Hz. The FRF curves measured by EMA and ISMA almost overlap in the Figure 4.1, except for some minor differences attributed to residual noise and measurement error. The remnant of the cyclic load can only be observed in the FRF

measured at the point #5 at around 35 Hz, which, however, has become very inconspicuous due to the suppression of ISTA. Besides, the curves of FRF measured at other locations are very smooth at the frequency of cyclic load, indicating that the cyclic components have been well diminished by ISTA. Table 4.1 shows the FRAC between the FRFs measured by these two means under all scenarios. The value of FRAC is always higher than 0.993, which indicates very high similarity between the FRFs obtained, proving that the de-noising method of ISMA provides static comparable FRF data under in-service conditions.

It is noted that the first three modes are completely included in the recorded frequency range according to Figure 4.1. Considering that it is more convenient to obtain modal features of lower modes with higher accuracy, and that the first three mode shapes of such type of plate-like structure are usually heaving, rolling and pitching, the following work mainly focuses on the first three vibration modes of the plate.

Table 4.1: FRAC between the FRFs measured by EMA and ISMA

Damage scenario	Measurement point of FRF				
	#2	#4	#5	#6	#8
UD	0.9998	0.9997	0.9997	0.9999	0.9996
LD1	0.9997	0.9997	0.9998	0.9998	0.9998
LD3	0.9998	0.9998	0.9998	0.9999	0.9997
LD7	0.9996	0.9997	0.9993	0.9997	0.9996
LD9	0.9998	0.9997	0.9997	0.9997	0.9997
MD1	0.9994	0.9991	0.9992	0.9994	0.9996
MD3	0.9992	0.9990	0.9993	0.9993	0.9994
MD7	0.9990	0.9987	0.9980	0.9995	0.9991
MD9	0.9994	0.9990	0.9993	0.9989	0.9991
HD1	0.9999	0.9999	1.0000	0.9999	0.9999
HD3	0.9996	0.9935	0.9990	0.9993	0.9997
HD7	0.9989	0.9990	0.9983	0.9986	0.9992
HD9	0.9985	0.9973	0.9989	0.9986	0.9984

4.2.2 Acquisition of natural frequencies and mode shapes

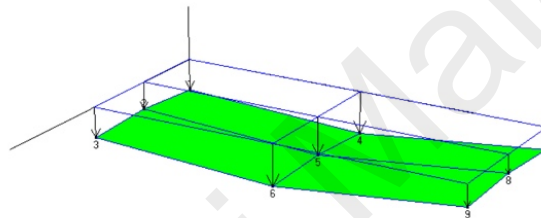
The natural frequencies of the first three modes are shown in Table 4.2. It can be seen that the natural frequencies decrease when damage occurs, and the higher severity of damage results in a more significant reduction in the natural frequencies. Table 4.2 also shows that the natural frequency obtained by ISMA is very close to that obtained by EMA, and their difference is always less than 0.2.

Table 4.2: First three natural frequencies of plate obtained by EMA and ISMA

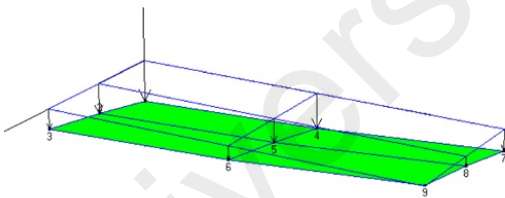
Damage scenario	1 st natural frequency		2 nd natural frequency		3 rd natural frequency	
	EMA	ISMA	EMA	ISMA	EMA	ISMA
UD	20.9	20.9	44.3	44.3	52.6	52.6
LD1	20.7	20.7	43.2	43.3	51.9	51.8
LD3	20.6	20.6	43.5	43.5	51.0	50.9
LD7	20.7	20.7	43.6	43.7	51.3	51.3
LD9	20.9	20.9	43.4	43.5	52.2	52.2
MD1	20.6	20.5	42.1	42.0	51.6	51.6
MD3	20.3	20.3	41.2	41.2	48.6	48.6
MD7	20.5	20.5	41.9	41.9	49.8	49.7
MD9	20.5	20.5	40.5	40.5	51.5	51.7
HD1	17.0	17.0	34.3	34.3	50.8	50.9
HD3	16.0	16.0	33.9	34.1	46.2	46.1
HD7	16.4	16.4	34.1	34.1	47.3	47.3
HD9	17.4	17.4	35.1	35.1	50.1	50.2

The first three mode shapes of the plate are shown in Figure 4.2. It can be seen from the figure that the mode shapes obtained by interpolation can still clearly reflect the effect of damage. The first mode is the heaving motion. When there is no damage, the plate moves in translation along the vertical direction and the four vertices of the plate are displaced equally. When damage takes place at any corner of the plate, the plate is tilted toward the damage point. The second mode is rolling. In the undamaged condition, the plate rolls around the longitudinal axis. The four vertices are displaced with almost the same amplitude, but points #1, #7 and points #3, #9 are of opposite phases. Damage can cause the deflection of the nodal line (the longitudinal axis). When damage occurs at point #1 or #9, the displacement at points #1 and #9 is larger than that at points #3 and #7.

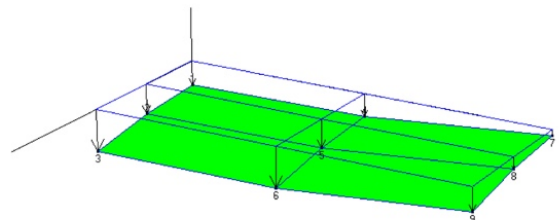
When damage occurs at points #3 or #7, the displacement at points #1 and #9 is smaller than that at points #3 and #7. The third mode is pitching. In the undamaged condition, the four vertices are displaced with almost the same amplitude, but points #1, #3 and points #7, #9 are of opposite phases. Damage can also cause the deflection of the pitch line (the lateral axis). When damage occurs at point #1 or #9, the displacement at points #1 and #9 is smaller than that at points #3 and #7. When damage occurs at points #3 or #7, the displacement at points #1 and #9 is larger than that at points #3 and #7. Although different vibration behaviors are seen under different damage scenarios, overall the first three modes still show the characteristics of heaving, rolling and pitching.



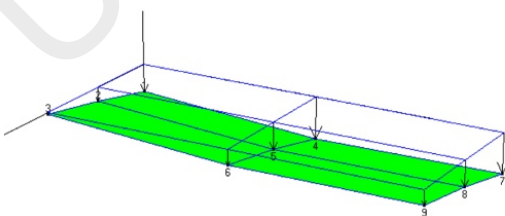
i. Undamaged



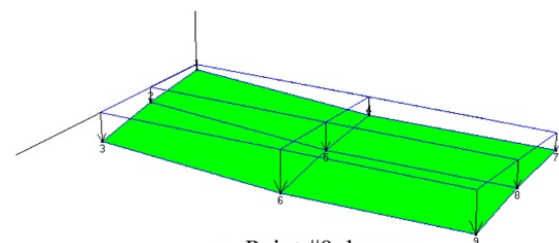
ii. Point #1 damage



iii. Point #3 damage



iv. Point #7 damage



v. Point #9 damage

(a) First mode shapes of plate

Figure 4.2, continued

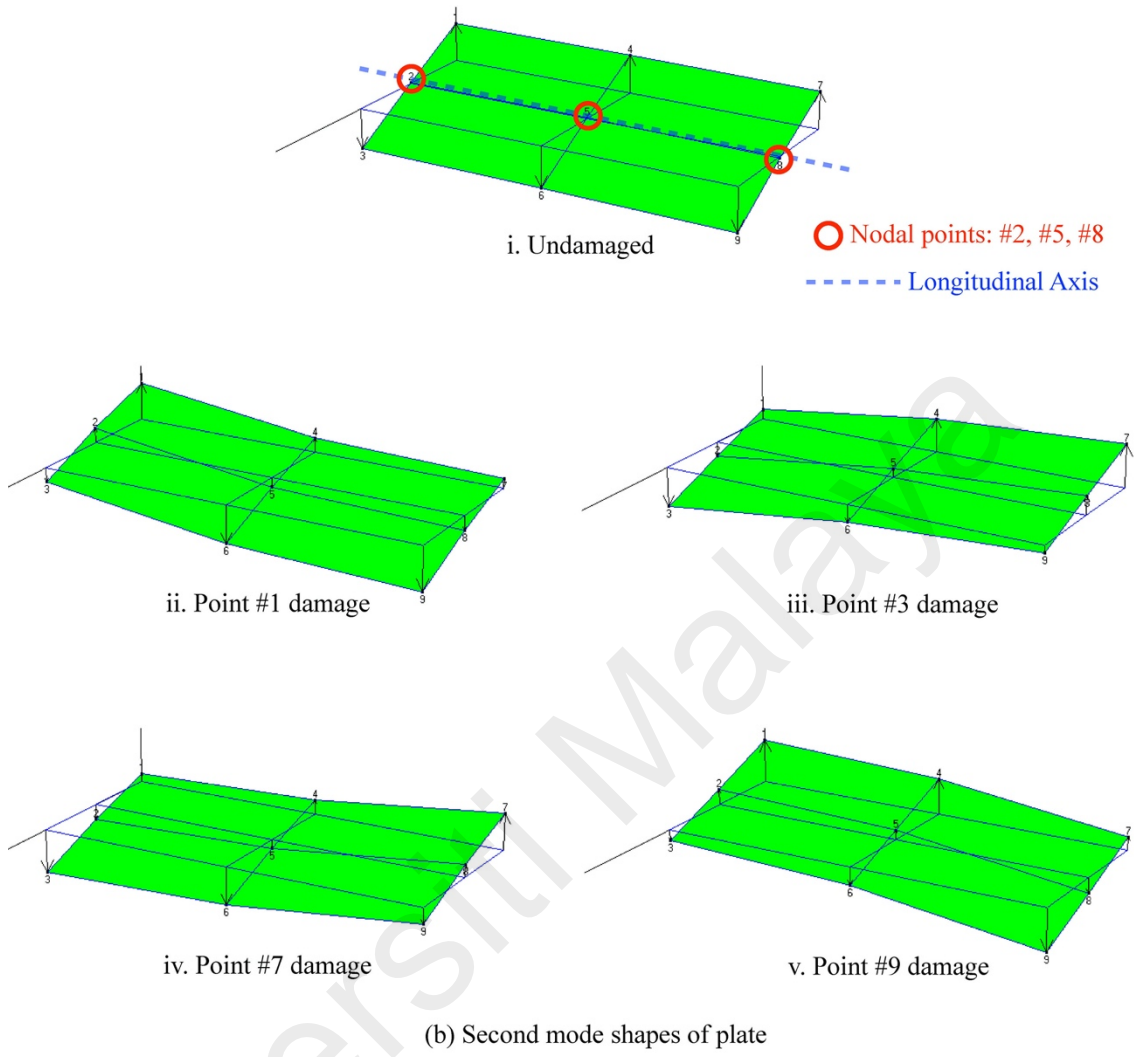


Figure 4.2, continued

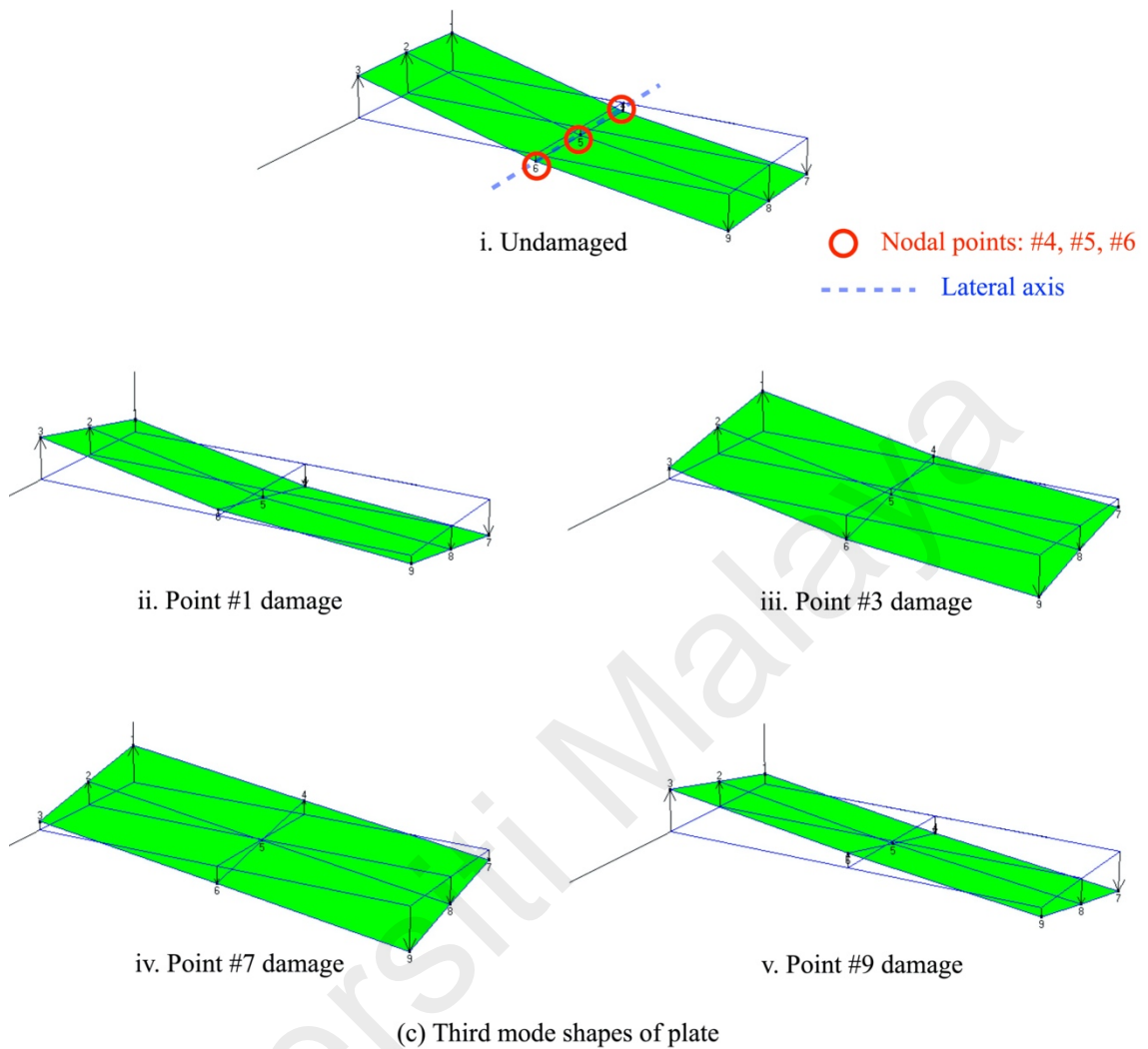


Figure 4.2: First three mode shapes of plate with different damage locations

Table 4.3 compares the MAC between the mode shapes obtained by EMA and ISMA data under all scenarios. The results show that the value of MAC between the mode shapes obtained by these two methods is higher than 0.997. This indicates that the denoising method of ISMA can also provide static-comparable mode shapes during the in-service condition.

In fact, the natural frequency and mode shape obtained in the modal analysis are retrieved from the FRF. Since ISMA offers static-comparable FRF as discussed in 4.2.1,

the natural frequency and mode shape can therefore be obtained accurately under the operational condition.

Table 4.3: MAC between mode shapes obtained by EMA and ISMA

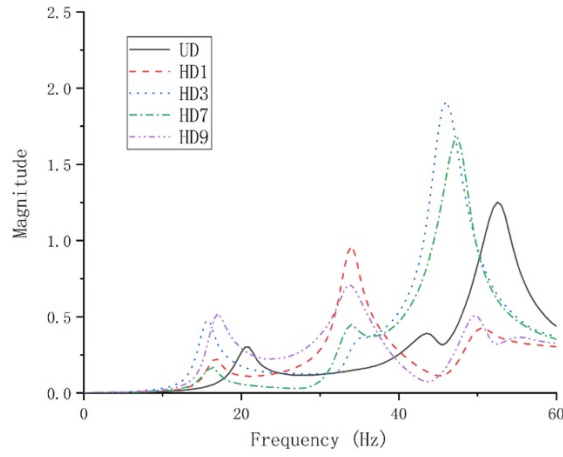
Damage scenario	Vibration mode		
	1 st mode	2 nd mode	3 rd mode
UD	0.99995	0.99997	0.99996
LD1	0.99996	0.99982	0.99954
LD3	1.00000	1.00000	0.99989
LD7	0.99998	0.99997	0.99983
LD9	0.99998	0.99999	0.99991
MD1	0.99998	0.99990	0.99974
MD3	0.99996	0.99993	0.99938
MD7	0.99999	0.99997	0.99998
MD9	0.99999	0.99987	0.99971
HD1	0.99994	0.99999	0.99976
HD3	0.99996	0.99739	0.99997
HD7	0.99997	0.99999	1.00000
HD9	0.99999	0.99998	0.99884

4.3 Development of operational damage identification scheme using supervised learning

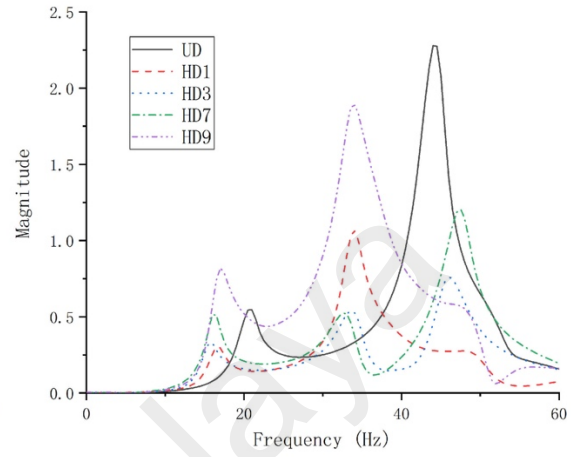
4.3.1 Construction of input feature: FRF change

To construct the input feature, namely the FRF change δ over a frequency segment, the frequency range needs to be determined at first. Figure 4.3 is the FRF graphs of each measurement point under five HD scenarios, which shows the shift of FRFs attributed to different types of damage. The first three modes of vibration are covered in the frequency range of 0~60 Hz. It is noted that FRFs of each damage scenario are unique, and the resonant peaks tend to move left towards the lower frequency range when damage takes place. Along with the shift of the peaks, the value of FRF changes drastically near the natural frequencies. Meanwhile, the change is not so obvious in anti-resonant frequency segments where the FRF curves are relatively flat. It is also observed that some resonant

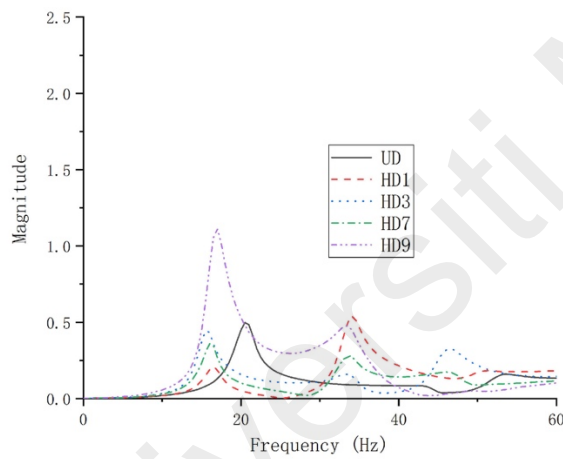
peaks are of rather small magnitudes because the corresponding measurement points are on the nodal line and nearly remain at rest in vibration. For example, point #5, which is located at the center of the plate, is on the nodal line of the second and third modes.



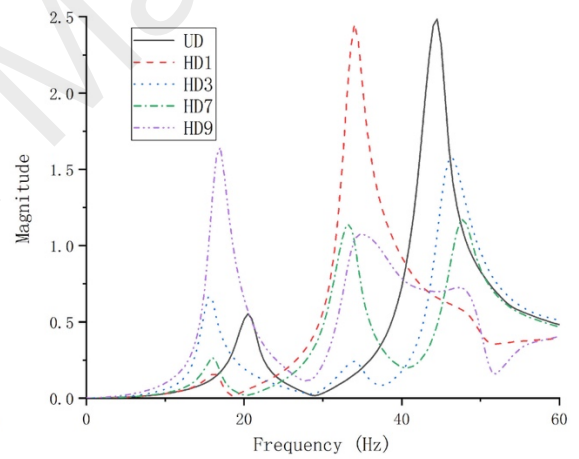
(a) FRF measured at point #2



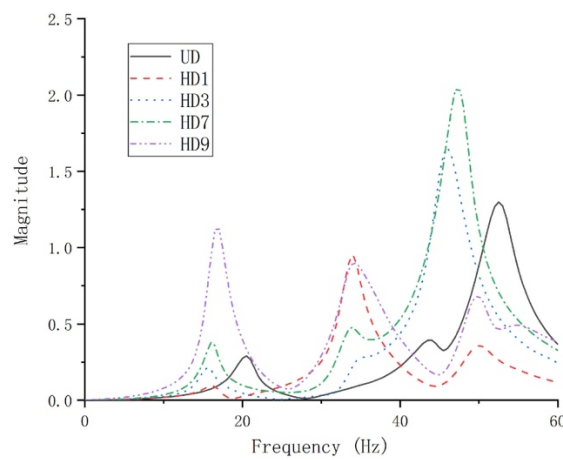
(b) FRF measured at point #4



(c) FRF measured at point #5



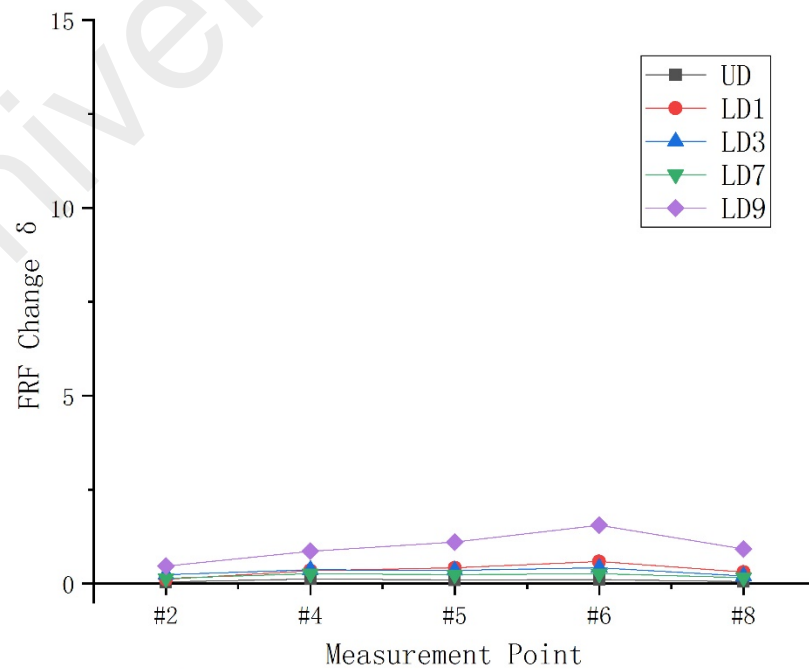
(d) FRF measured at point #6



(e) FRF measured at point #8

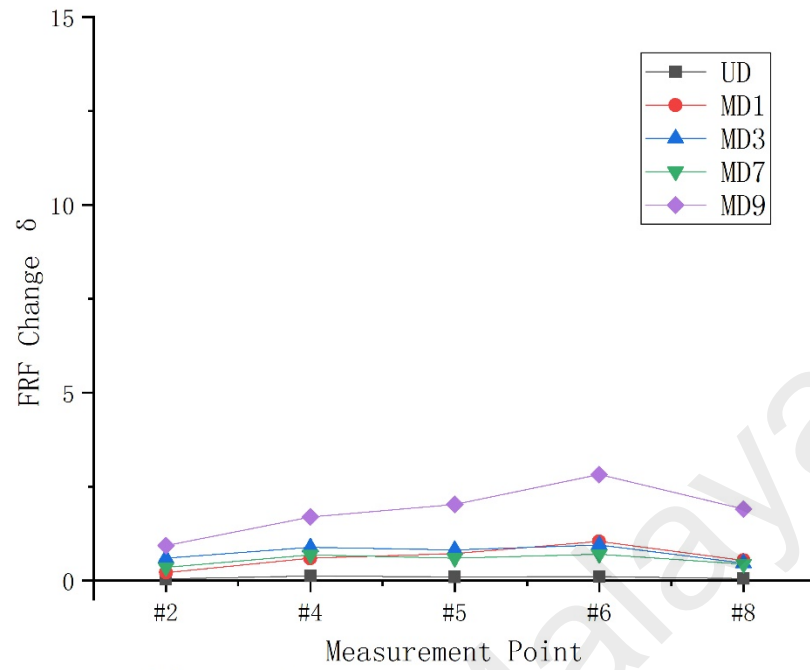
Figure 4.3: Comparison of FRFs of HD scenarios

According to the previous discussion, significant change in FRF is observed near the natural frequencies when damage takes place, which means FRFs are more sensitive to structural damage in these frequency intervals. Therefore, it is sensible to construct input features using the FRF data near the natural frequencies. Three frequency intervals, namely 10~25 Hz, 30~40 Hz and 45~55 Hz were selected, which respectively correspond to the first three vibration modes. The input features were calculated from the FRFs in these frequency intervals. The frequency bands are narrow, which ensures that only the corresponding vibration modes are dominant in these intervals. This makes it feasible to optimize the placement of measurement points by looking into the modal shape of the dominant vibration mode in the selected frequency interval, which will be discussed later in this section. Figure 4.4, Figure 4.5 and Figure 4.6 show the input features of the three frequency intervals (FRF changes in 10~25 Hz, 30~40 Hz and 45~55 Hz) that were calculated using the FRF data of each damage scenario. The input feature vector is of five dimensions that respectively correspond to the FRF change of the five measurement points.

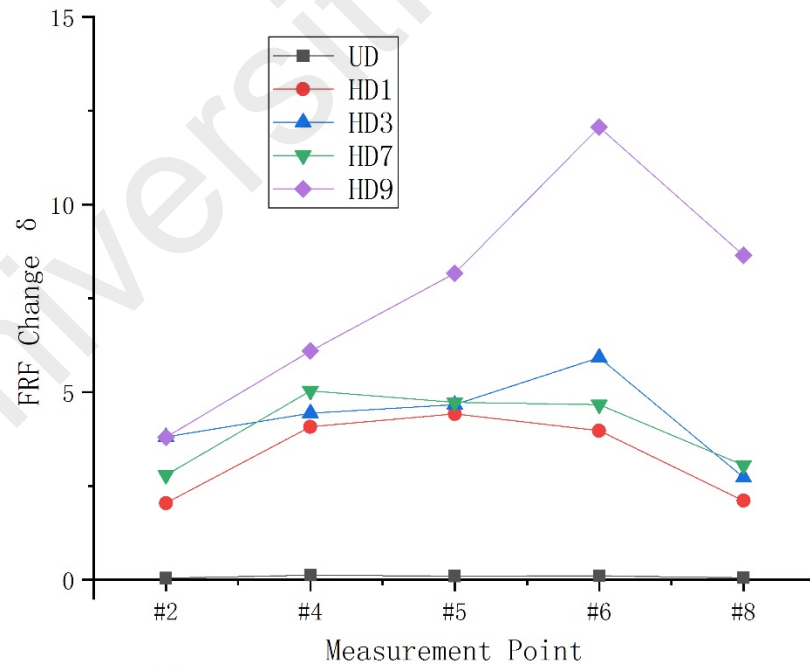


(a) FRF change of LD scenarios in 10-25 Hz

Figure 4.4, continued

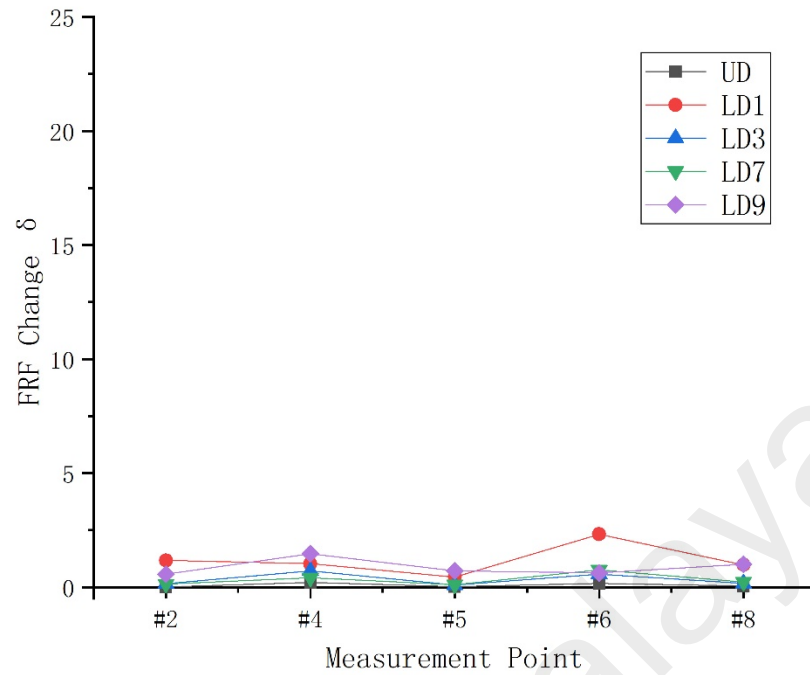


(b) FRF change of MD scenarios in 10-25 Hz

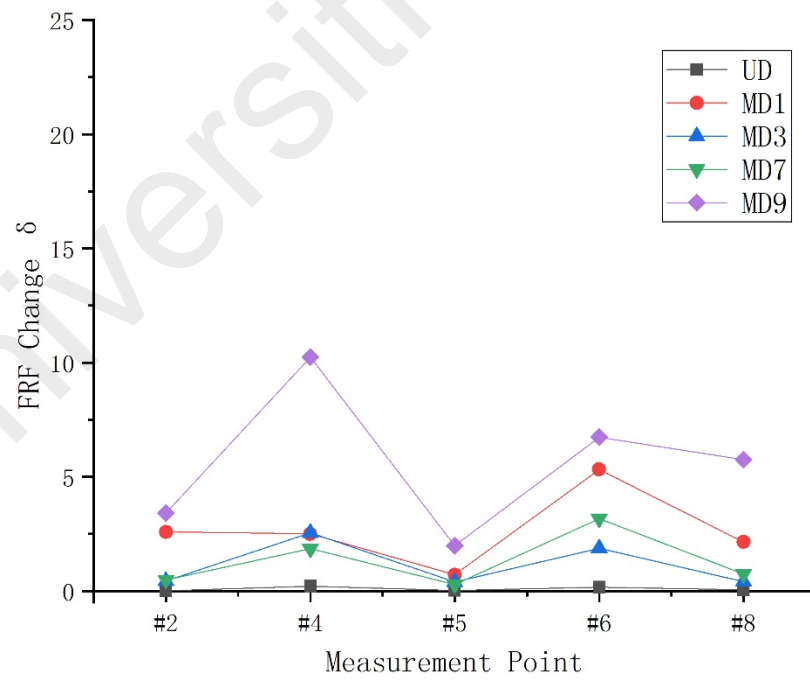


(c) FRF change of HD scenarios in 10-25 Hz

Figure 4.4: Input features of network: FRF change δ in 10~25 Hz

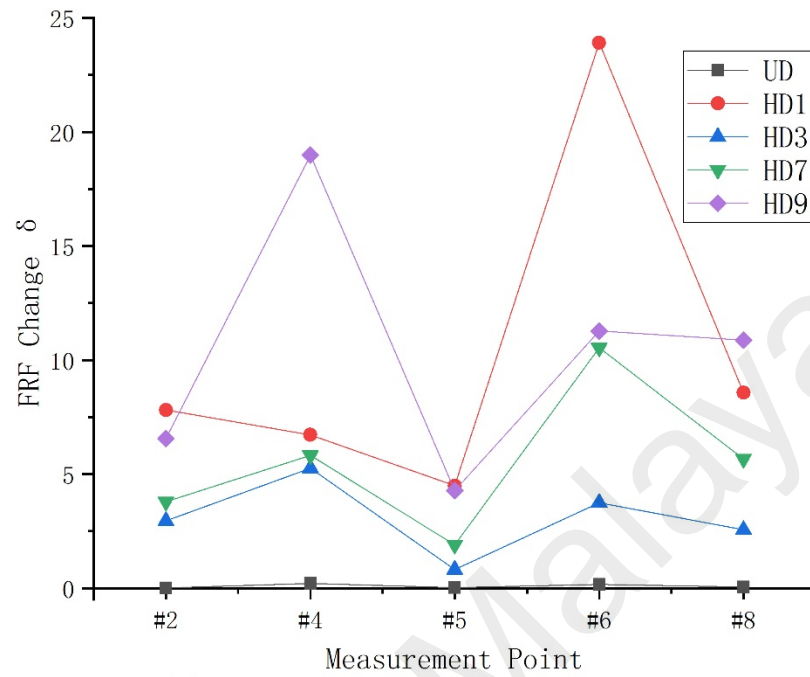


(a) FRF change of LD scenarios in 30–40 Hz



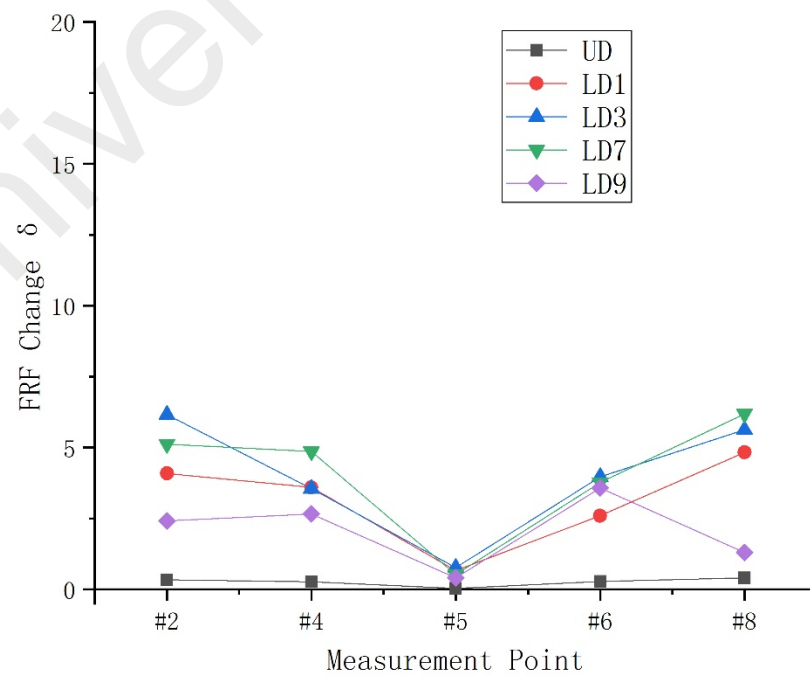
(b) FRF change of MD scenarios in 30–40 Hz

Figure 4.5, continued



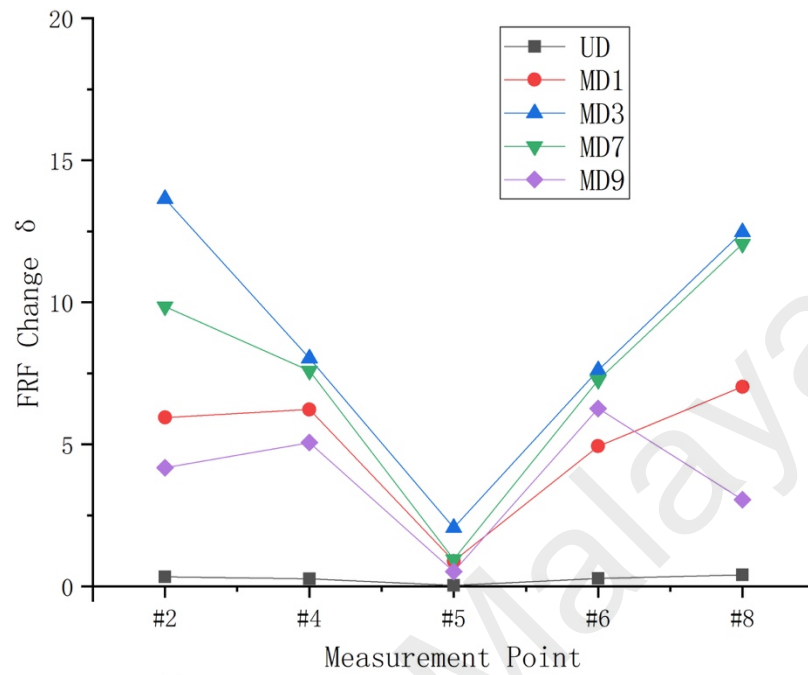
(c) FRF change of HD scenarios in 30~40 Hz

Figure 4.5: Input features of network: FRF change δ in 30~40 Hz

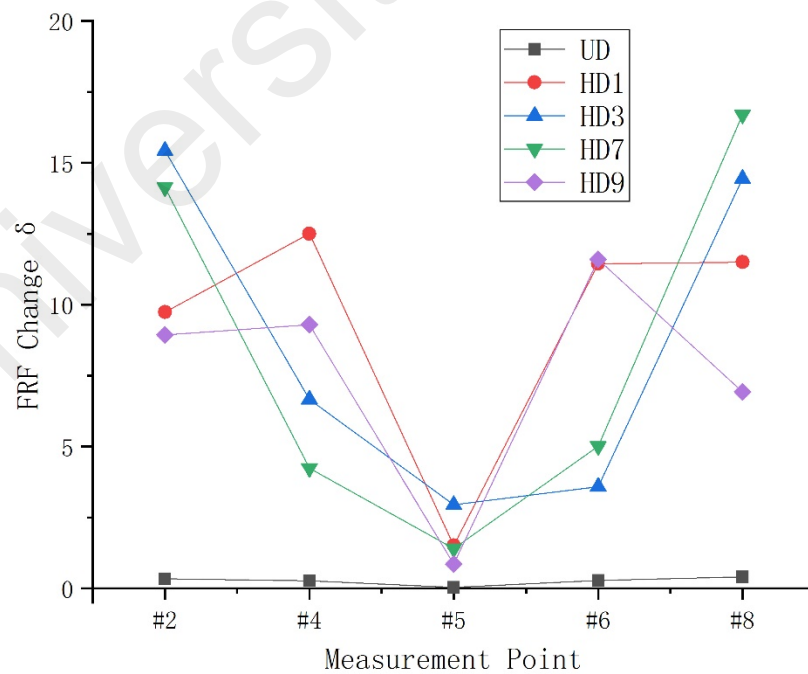


(a) FRF change of LD scenarios in 45~55 Hz

Figure 4.6, continued



(b) FRF change of MD scenarios in 45–55 Hz



(c) FRF change of HD scenarios in 45–55 Hz

Figure 4.6: Input features of network: FRF change δ in 45~55 Hz

When the subplots of Figures 4.4, 4.5 and 4.6 are compared respectively, it can be seen that the more severe damage causes the more obvious changes in FRF. For LD damage, the value of δ at each measurement point is small, and the difference between different damage locations is not obvious. In MD damage, the values of δ start to increase, and the difference between different damage scenarios also becomes obvious. In HD damage, the value of δ is the largest and the variety of δ is most obvious. It can be noted that the sensitivity of FRF at different measurement points to damage also varies, and the sensitivity is also related to the selected frequency range. For example, in the second and third modes, the FRF measured at point #5 is less sensitive to damage than other measurement points. As we will see later, this phenomenon is related to the vibrational shape of the plate.

Tables 4.4, 4.5 and 4.6 show the natural frequencies of the first three modes and the FRF change δ of the five measurement points. Compared with the natural frequency, using FRF change is more advantageous because the FRF is more informative. The natural frequency, as a global property of the structure, is limited in indicating damage location, because damage with different locations may lead to a similar shift in natural frequencies. For example, the first natural frequencies of MD7 and MD9 scenarios are both 20.5 Hz according to Table 4.4. The second natural frequencies of LD3 and LD7 are 34.5 Hz and 34.6 Hz according to Table 4.5, which are also very close and can be difficult to distinguish. In these cases, the damage cannot be located with the natural frequency. Another drawback is that the change in the natural frequency is not very sensitive (Carden & Fanning, 2004; H. L. Chen et al., 1995). For example, even in MD severity cases, the reduction in the first natural frequency can still be as low as 1.4%. Meanwhile, structural damage can be reflected more clearly by changes in FRF. Moreover, sometimes different damage types result in the same natural frequency, but their FRF changes are distinct (e.g. the first mode of MD7 and MD9). This is because the FRF change method involves the

modal information in a frequency range, which is more informative than only using the single natural frequency. Therefore, the damage feature based on FRF change has advantages over natural frequency and is suitable to be used as the input feature for supervised learning.

Table 4.4: Comparison between natural frequency and FRF change of first mode

Damage scenario	1 st natural frequency	Change in natural frequency	FRF change δ in 10~25 Hz				
			#2	#4	#5	#6	#8
LD1	20.7	1.0%	0.12	0.35	0.42	0.59	0.31
LD3	20.6	1.4%	0.24	0.37	0.36	0.42	0.21
LD7	20.7	1.0%	0.14	0.26	0.24	0.27	0.16
LD9	20.9	0.0%	0.47	0.86	1.11	1.56	0.92
MD1	20.6	1.4%	0.21	0.60	0.72	1.05	0.54
MD3	20.3	2.9%	0.60	0.89	0.82	0.95	0.46
MD7	20.5	1.9%	0.35	0.69	0.60	0.70	0.44
MD9	20.5	1.9%	0.93	1.70	2.03	2.82	1.90
HD1	17.0	18.7%	2.04	4.08	4.42	3.97	2.11
HD3	16.0	23.4%	3.81	4.44	4.67	5.92	2.73
HD7	16.4	21.5%	2.79	5.03	4.73	4.67	3.06
HD9	17.4	16.7%	3.80	6.10	8.17	12.07	8.65

Table 4.5: Comparison between natural frequency and FRF change of second mode

Damage scenario	2 nd natural frequency	Change in natural frequency	FRF change δ in 30~40 Hz				
			#2	#4	#5	#6	#8
LD1	43.2	2.5%	1.17	1.03	0.45	2.32	0.98
LD3	43.5	1.8%	0.15	0.72	0.09	0.57	0.17
LD7	43.6	1.6%	0.14	0.41	0.11	0.76	0.22
LD9	43.4	2.0%	0.57	1.47	0.72	0.63	1.01
MD1	42.1	5.0%	2.58	2.50	0.71	5.32	2.15
MD3	41.2	7.0%	0.44	2.54	0.40	1.87	0.42
MD7	41.9	5.4%	0.49	1.86	0.28	3.17	0.74
MD9	40.5	8.6%	3.41	10.24	1.98	6.74	5.76
HD1	34.3	22.6%	7.81	6.72	4.49	23.92	8.57
HD3	33.9	23.5%	2.95	5.26	0.82	3.75	2.57
HD7	34.1	23.0%	3.78	5.82	1.90	10.54	5.67
HD9	35.1	20.8%	6.55	18.99	4.28	11.28	10.88

Table 4.6: Comparison between natural frequency and FRF change of third mode

Damage scenario	3 rd natural frequency	Change in natural frequency	FRF change δ in 45~55 Hz				
			#2	#4	#5	#6	#8
LD1	51.9	1.3%	4.09	3.59	0.67	2.60	4.83
LD3	51.0	3.0%	6.17	3.55	0.77	3.97	5.63
LD7	51.3	2.5%	5.12	4.86	0.52	3.77	6.18
LD9	52.2	0.8%	2.41	2.66	0.41	3.58	1.30
MD1	51.6	1.9%	5.94	6.23	0.89	4.93	7.03
MD3	48.6	7.6%	13.65	8.03	2.06	7.61	12.48
MD7	49.8	5.3%	9.85	7.58	0.95	7.26	12.05
MD9	51.5	2.1%	4.17	5.06	0.52	6.27	3.05
HD1	50.8	3.4%	9.74	12.51	1.51	11.44	11.50
HD3	46.2	12.2%	15.43	6.66	2.95	3.59	14.45
HD7	47.3	10.1%	14.14	4.24	1.40	5.02	16.70
HD9	50.1	4.8%	8.94	9.30	0.86	11.59	6.93

4.3.2 Damage identification using BP network

At this stage, the BP network was trained using the EMA samples, and tested using ISMA samples collected under the in-service condition. All the damage states were included in the training and testing set, including UD, LD, MD and HD scenarios (13 scenarios in total). Table 4.7 shows the testing performance of the network when FRF changes of the five measurement points were used, with the frequency ranges of 10~25 Hz, 30~40 Hz, and 45~55 Hz.

Table 4.7: Performance of damage identification based on BP network using FRF change of five measurement points (UD, LD, MD and HD scenarios)

Frequency range	Sensors	Testing performance	
		Cross entropy	Classification accuracy
10~25 Hz	5 sensors at points #2, #4, #5, #6, #8	5.51E-03	95.7%
30~40 Hz		2.87E-02	95.0%
45~55 Hz		4.73E-04	99.3%

As shown in Table 4.7, the classification accuracy of the testing results is higher than 95%. The accuracy of testing performance reaches 99.3% when the FRF change in 45~55 Hz is used as the input feature, which means the damage identification results are of high accuracy in this case. However, the table can only present the overall performance of damage identification, while Figure 4.7 uses the confusion matrix to specifically compare the results of the network judgment with the actual damage states of the testing samples.

In Figure 4.7, the diagonal cells show the number and percentage of correct classifications by the trained network. Taking Figure 4.7 (a) as an example, 15 UD samples were correctly classified. This corresponds to 10.7% of all 140 testing samples. However, five UD samples were misclassified as LD7, which accounts for 3.6% of all 140 testing samples. Similarly, nine LD7 samples were correctly classified while one LD7 sample was misclassified as UD sample. In addition, the rest samples all distribute in the diagonal cells, indicating that the outputs are consistent with the targets and the damage states of these samples were correctly identified. Overall, 95.7% of the predictions were correct and 4.3% were wrong classifications when FRF change in frequency range 10~25 Hz was used. Similar to the discussion of Figure 4.7 (a), Figure 4.7 (b) shows that three LD3 samples were misclassified as UD and four LD3 samples were misclassified as LD7 when FRF change in frequency range 30~40 Hz was used. Meanwhile, Figure 4.7 (c) shows that one LD9 sample was misclassified as UD when FRF change in frequency range 45~55 Hz was used.

Confusion Matrix

Output Class	UD	15 10.7%	0 0.0%	0 0.0%	1 0.7%	0 0.0%	0 0.0%	0 0.0%	0 0.0%	0 0.0%	0 0.0%	0 0.0%	0 0.0%	93.8% 6.2%	
	LD1	0 0.0%	10 7.1%	0 0.0%	0 0.0%	0 0.0%	0 0.0%	0 0.0%	0 0.0%	0 0.0%	0 0.0%	0 0.0%	0 0.0%	100% 0.0%	
	LD3	0 0.0%	0 0.0%	10 7.1%	0 0.0%	0 0.0%	0 0.0%	0 0.0%	0 0.0%	0 0.0%	0 0.0%	0 0.0%	0 0.0%	100% 0.0%	
	LD7	5 3.6%	0 0.0%	0 0.0%	9 6.4%	0 0.0%	0 0.0%	0 0.0%	0 0.0%	0 0.0%	0 0.0%	0 0.0%	0 0.0%	64.3% 35.7%	
	LD9	0 0.0%	0 0.0%	0 0.0%	0 0.0%	10 7.1%	0 0.0%	100% 0.0%							
	MD1	0 0.0%	0 0.0%	0 0.0%	0 0.0%	0 0.0%	10 7.1%	0 0.0%	0 0.0%	0 0.0%	0 0.0%	0 0.0%	0 0.0%	100% 0.0%	
	MD3	0 0.0%	0 0.0%	0 0.0%	0 0.0%	0 0.0%	0 0.0%	10 7.1%	0 0.0%	0 0.0%	0 0.0%	0 0.0%	0 0.0%	100% 0.0%	
	MD7	0 0.0%	0 0.0%	0 0.0%	0 0.0%	0 0.0%	0 0.0%	0 0.0%	10 7.1%	0 0.0%	0 0.0%	0 0.0%	0 0.0%	100% 0.0%	
	MD9	0 0.0%	0 0.0%	0 0.0%	0 0.0%	0 0.0%	0 0.0%	0 0.0%	0 0.0%	10 7.1%	0 0.0%	0 0.0%	0 0.0%	100% 0.0%	
	HD1	0 0.0%	0 0.0%	0 0.0%	0 0.0%	0 0.0%	0 0.0%	0 0.0%	0 0.0%	0 0.0%	10 7.1%	0 0.0%	0 0.0%	100% 0.0%	
	HD3	0 0.0%	0 0.0%	0 0.0%	0 0.0%	0 0.0%	0 0.0%	0 0.0%	0 0.0%	0 0.0%	0 0.0%	10 7.1%	0 0.0%	100% 0.0%	
	HD7	0 0.0%	0 0.0%	0 0.0%	0 0.0%	0 0.0%	0 0.0%	0 0.0%	0 0.0%	0 0.0%	0 0.0%	0 0.0%	10 7.1%	100% 0.0%	
	HD9	0 0.0%	0 0.0%	0 0.0%	0 0.0%	0 0.0%	0 0.0%	0 0.0%	0 0.0%	0 0.0%	0 0.0%	0 0.0%	0 0.0%	10 7.1%	100% 0.0%
			75.0% 25.0%	100% 0.0%	100% 0.0%	90.0% 10.0%	100% 0.0%	95.7% 4.3%							
		UD	LD1	LD3	LD7	LD9	MD1	MD3	MD7	MD9	HD1	HD3	HD7	HD9	
		Target Class													

(a) Testing results using FRF change in 10-25 Hz

Figure 4.7, continued

Output Class	UD	20 14.3%	0 0.0%	3 2.1%	0 0.0%	87.0% 13.0%								
	LD1	0 0.0%	10 7.1%	0 0.0%	0 0.0%	0 0.0%	0 0.0%	0 0.0%	0 0.0%	0 0.0%	0 0.0%	0 0.0%	0 0.0%	100% 0.0%
	LD3	0 0.0%	0 0.0%	3 2.1%	0 0.0%	100% 0.0%								
	LD7	0 0.0%	0 0.0%	4 2.9%	10 7.1%	0 0.0%	71.4% 28.6%							
	LD9	0 0.0%	0 0.0%	0 0.0%	0 0.0%	10 7.1%	0 0.0%	100% 0.0%						
	MD1	0 0.0%	0 0.0%	0 0.0%	0 0.0%	0 0.0%	10 7.1%	0 0.0%	0 0.0%	0 0.0%	0 0.0%	0 0.0%	0 0.0%	100% 0.0%
	MD3	0 0.0%	0 0.0%	0 0.0%	0 0.0%	0 0.0%	0 0.0%	10 7.1%	0 0.0%	0 0.0%	0 0.0%	0 0.0%	0 0.0%	100% 0.0%
	MD7	0 0.0%	0 0.0%	0 0.0%	0 0.0%	0 0.0%	0 0.0%	0 0.0%	10 7.1%	0 0.0%	0 0.0%	0 0.0%	0 0.0%	100% 0.0%
	MD9	0 0.0%	0 0.0%	0 0.0%	0 0.0%	0 0.0%	0 0.0%	0 0.0%	0 0.0%	10 7.1%	0 0.0%	0 0.0%	0 0.0%	100% 0.0%
	HD1	0 0.0%	0 0.0%	0 0.0%	0 0.0%	0 0.0%	0 0.0%	0 0.0%	0 0.0%	0 0.0%	10 7.1%	0 0.0%	0 0.0%	100% 0.0%
	HD3	0 0.0%	0 0.0%	0 0.0%	0 0.0%	0 0.0%	0 0.0%	0 0.0%	0 0.0%	0 0.0%	0 0.0%	10 7.1%	0 0.0%	100% 0.0%
	HD7	0 0.0%	0 0.0%	0 0.0%	0 0.0%	0 0.0%	0 0.0%	0 0.0%	0 0.0%	0 0.0%	0 0.0%	0 0.0%	10 7.1%	100% 0.0%
	HD9	0 0.0%	0 0.0%	0 0.0%	0 0.0%	0 0.0%	0 0.0%	0 0.0%	0 0.0%	0 0.0%	0 0.0%	0 0.0%	10 7.1%	100% 0.0%
		100% 0.0%	100% 0.0%	30.0% 70.0%	100% 0.0%	100% 0.0%								
	UD	LD1	LD3	LD7	LD9	MD1	MD3	MD7	MD9	HD1	HD3	HD7	HD9	
	Target Class													

(b) Testing results using FRF change in 30-40 Hz

Figure 4.7, continued

Output Class	UD	20 14.3%	0 0.0%	0 0.0%	0 0.0%	1 0.7%	0 0.0%	95.2% 4.8%								
	LD1	0 0.0%	10 7.1%	0 0.0%	0 0.0%	0 0.0%	0 0.0%	0 0.0%	0 0.0%	0 0.0%	0 0.0%	0 0.0%	0 0.0%	0 0.0%	100% 0.0%	
	LD3	0 0.0%	0 0.0%	10 7.1%	0 0.0%	0 0.0%	0 0.0%	0 0.0%	0 0.0%	0 0.0%	0 0.0%	0 0.0%	0 0.0%	0 0.0%	100% 0.0%	
	LD7	0 0.0%	0 0.0%	0 0.0%	10 7.1%	0 0.0%	0 0.0%	0 0.0%	0 0.0%	0 0.0%	0 0.0%	0 0.0%	0 0.0%	0 0.0%	100% 0.0%	
	LD9	0 0.0%	0 0.0%	0 0.0%	0 0.0%	9 6.4%	0 0.0%	100% 0.0%								
	MD1	0 0.0%	0 0.0%	0 0.0%	0 0.0%	0 0.0%	10 7.1%	0 0.0%	100% 0.0%							
	MD3	0 0.0%	0 0.0%	0 0.0%	0 0.0%	0 0.0%	0 0.0%	10 7.1%	0 0.0%	0 0.0%	0 0.0%	0 0.0%	0 0.0%	0 0.0%	100% 0.0%	
	MD7	0 0.0%	0 0.0%	0 0.0%	0 0.0%	0 0.0%	0 0.0%	0 0.0%	10 7.1%	0 0.0%	0 0.0%	0 0.0%	0 0.0%	0 0.0%	100% 0.0%	
	MD9	0 0.0%	0 0.0%	0 0.0%	0 0.0%	0 0.0%	0 0.0%	0 0.0%	0 0.0%	10 7.1%	0 0.0%	0 0.0%	0 0.0%	0 0.0%	100% 0.0%	
	HD1	0 0.0%	0 0.0%	0 0.0%	0 0.0%	0 0.0%	0 0.0%	0 0.0%	0 0.0%	0 0.0%	10 7.1%	0 0.0%	0 0.0%	0 0.0%	100% 0.0%	
	HD3	0 0.0%	0 0.0%	0 0.0%	0 0.0%	0 0.0%	0 0.0%	0 0.0%	0 0.0%	0 0.0%	0 0.0%	10 7.1%	0 0.0%	0 0.0%	100% 0.0%	
	HD7	0 0.0%	0 0.0%	0 0.0%	0 0.0%	0 0.0%	0 0.0%	0 0.0%	0 0.0%	0 0.0%	0 0.0%	0 0.0%	10 7.1%	0 0.0%	100% 0.0%	
	HD9	0 0.0%	0 0.0%	0 0.0%	0 0.0%	0 0.0%	0 0.0%	0 0.0%	0 0.0%	0 0.0%	0 0.0%	0 0.0%	0 0.0%	10 7.1%	100% 0.0%	
		100% 0.0%	100% 0.0%	100% 0.0%	100% 0.0%	90.0% 10.0%	100% 0.0%	99.3% 0.7%								
		UD	LD1	LD3	LD7	LD9	MD1	MD3	MD7	MD9	HD1	HD3	HD7	HD9		
	Target Class															

(c) Testing results using FRF change in 45-55 Hz

Figure 4.7: Testing results of damage identification based on BP network using FRF change of five measurement points (UD, LD, MD and HD scenarios)

From Figure 4.7, it is found that the identification of MD and HD cases, whose damage is of higher severity, is more accurate, and the accuracy reached 100%. Meanwhile, as to the low-severity damage in LD scenarios, the confusion matrices show that the network cannot always correctly determine the location of damage, or mistakes them into the

undamaged category. When damage severity is low, the change in the FRF is minor. Consequently, the values of FRF change δ can be too small to be distinguished. Therefore, the performance of damage identification is not good for LD damage, but may still be effective for MD and HD cases. To verify this, damage identification was then carried out only using UD, HD and MD data (9 damage scenarios). The results are shown in Table 4.8. It is found that the damage states of all the testing samples are correctly identified with 100% accuracy.

Table 4.8: Performance of damage identification based on BP network using FRF change of five measurement points (UD, HD and MD scenarios)

Frequency range	Sensors	Testing performance	
		Cross entropy	Classification accuracy
10~25 Hz	5 sensors at points #2, #4, #5, #6, #8	1.23E-04	100%
30~40 Hz		2.43E-06	100%
45~55 Hz		2.46E-06	100%

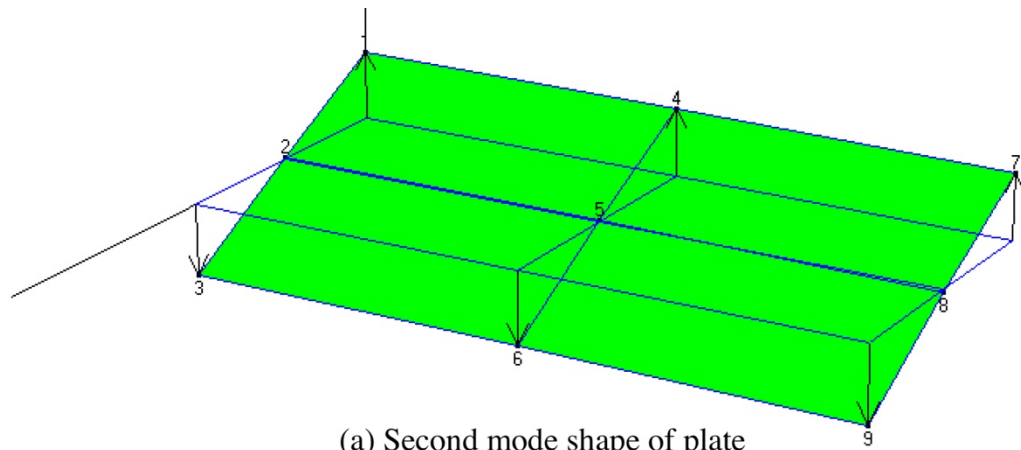
4.3.3 Optimization of measurement points using mode shape assessment

The performance of damage identification is satisfying so far with FRF data measured at all five points of the plate (points #2, #4, #5, #6, #8). However, if the number of measurement points can be reduced, the damage identification scheme will be more cost-effective in terms of the accelerometer hardware and computational complexity of network training. The locations of the measurement points should be kindly taken into consideration, which can influence the performance of the results. Specifically, the measurement points should be avoided on a nodal line. The second vibration mode is first discussed as an example. Figure 4.8 (a) illustrates the second mode shape of the plate, which is dominant in the frequency of 30~40 Hz. The second mode of the plate is the rolling movement around the longitudinal axis. Point #4 and point #6, which are far away from the nodal line, are of a larger amplitude of vibration, while the other three measurement points on the nodal line are nearly at rest in vibration. Correspondingly,

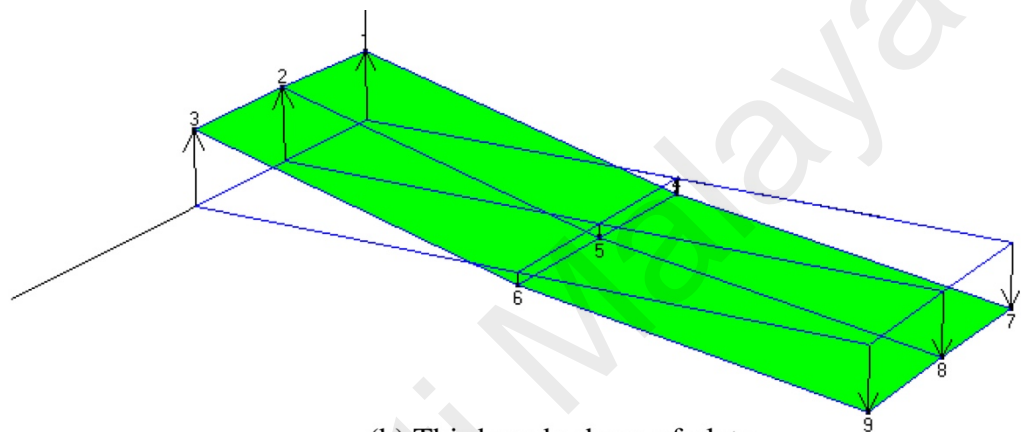
more obvious resonant peaks are seen at the points #4 and #6 in the second mode, and the FRF change δ of these two points is more sensitive to damage. Meanwhile, the flat FRFs of the points #2, #5 and #8 always lead to low values of δ at these points, regardless of the damage status of the plate. Different damage scenarios would not be well distinguished if all the measurement points fall on the nodal. Therefore, the new input feature vector was built with the FRF changes at the points #4 and #6, of which the dimension was reduced to two. Similar to dimension reduction of the second vibration mode, the measurement points can also be optimized when the frequency range of 45~55 Hz is used, which corresponds to the third vibration mode. Figure 4.8 (b) shows the third mode shape of the plate. Different from the second mode, points #2 and #8 are of the largest displacement in this case. Therefore, the FRF change at these two points was used as the input feature. Following the same procedure of 4.3.2, the network was trained using the EMA data and tested using ISMA data in 30~40 Hz. The HD and MD severities were considered, along with UD state. Table 4.9 shows that accuracy of 100% can still be achieved with the number of measurement points reduced to two. Therefore, the optimization of input features is a success. The frequency range of 10~25 Hz is dismissed because the displacements at each measurement point are similar to the heaving mode, and the optimization is not applicable in this case.

Table 4.9: Performance of damage identification based on BP network using FRF change of two measurement points (UD, HD and MD scenarios)

Frequency range	Sensors	Testing performance	
		Cross entropy	Classification accuracy
30~40 Hz	2 sensors at points #4 & #6	2.72E-04	100%
45~55 Hz	2 sensors at points #2 & #8	3.09E-05	100%



(a) Second mode shape of plate



(b) Third mode shape of plate

Figure 4.8: Second and third mode shapes of plate

Comparing the testing performance in Table 4.8 and Table 4.9, it can be observed that the cross entropy increases from $2.43\text{E-}06$ to $2.72\text{E-}04$ for the second mode (30~40 Hz) and increases from $2.46\text{E-}06$ to $3.09\text{E-}05$ for the third mode (45~55 Hz) when the number of measurement points reduces from five to two, indicating a larger error of the outputs. Nevertheless, the classification accuracy remains 100%, which means the increased error caused by the reduction of measurement points does not affect the result of damage identification, and is acceptable. Meanwhile, after the optimization of measurement points, only two accelerometers are needed for damage identification of the test plate, which makes it more cost-effective in terms of the accelerometer hardware and computation.

The damage identification scheme based on supervised learning has also been verified on another Perspex plate (Appendix A.1), with five damage scenarios (UD, HD1, HD3, HD7 and HD9) considered. The FRFs are presented in Appendix A.2. Appendix A.3 shows the FRF changes near the second and third vibration modes, which are the input feature of the BP network. The 100% accuracy shown in Appendix A.4 indicates that the proposed method is also applicable to other plates.

4.4 Development of operational damage identification scheme using unsupervised learning

4.4.1 Construction of WCC features from PCA-reduced FRF

Following the proposed scheme, the PCA-reduced FRF of each sample was obtained from the FRFs measured at five measurement points. Figure 4.9 shows the FRFs at these measurement points in the undamaged condition together with the PCA-reduced FRF derived from them as an example. The resonant peaks of the first three vibration modes are observed in the curve of the PCA-reduced FRF. Figure 4.10 shows the PCA-reduced FRF of all thirteen damage scenarios. It is observed that damage can lead to changes in the shape of PCA-reduced FRF curves, which is similar to the behavior of FRFs.

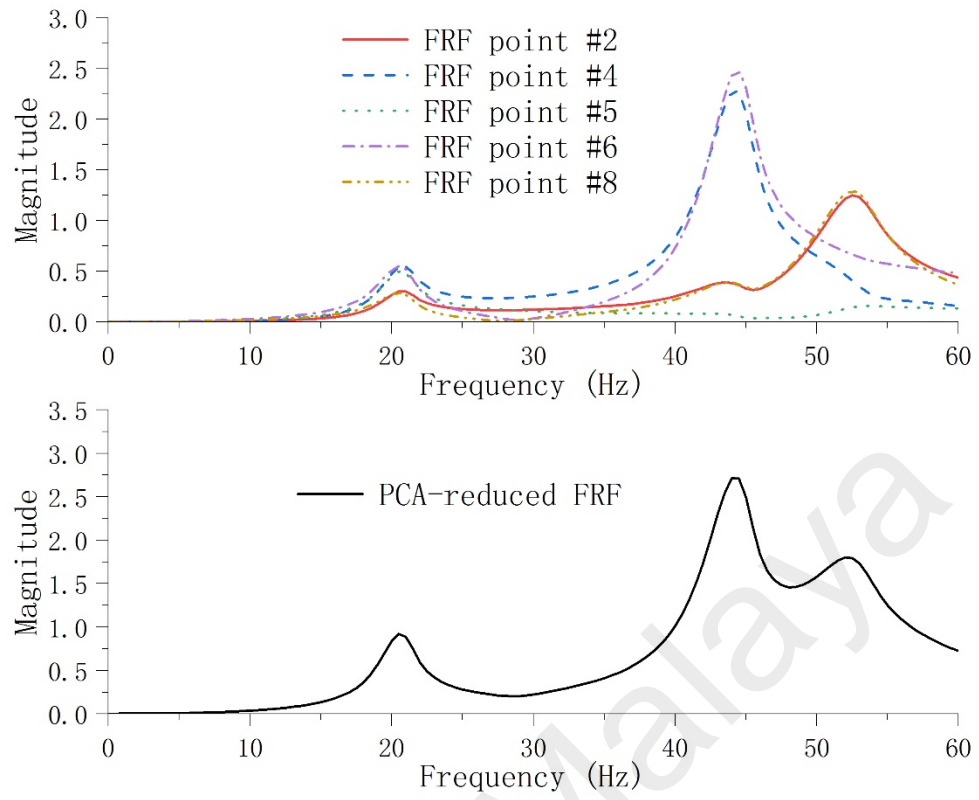
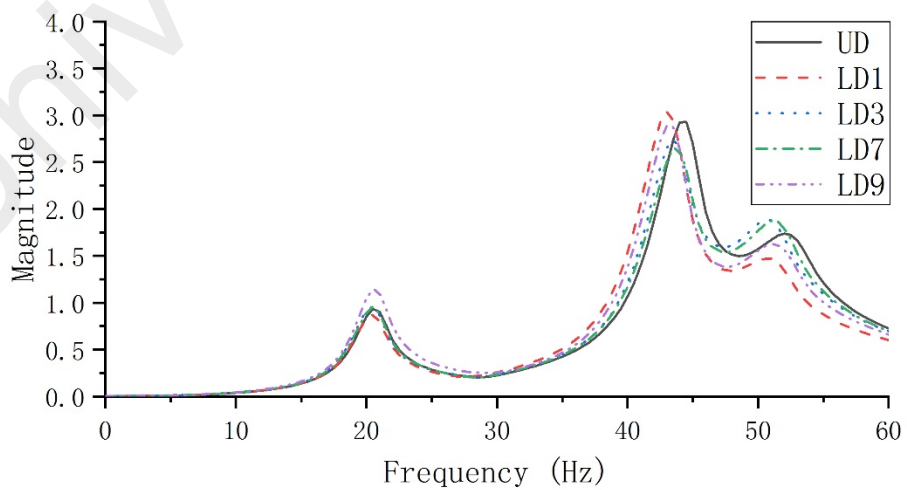
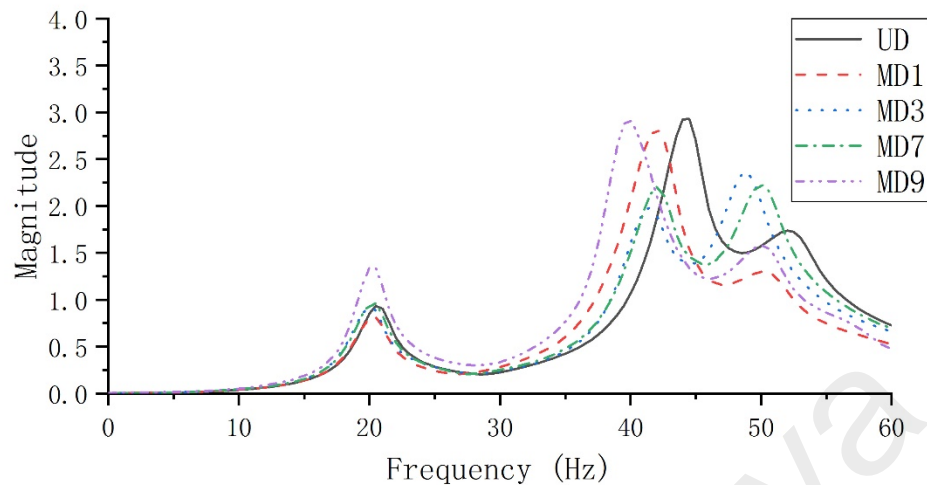


Figure 4.9: FRFs and PCA-reduced FRF of UD scenario

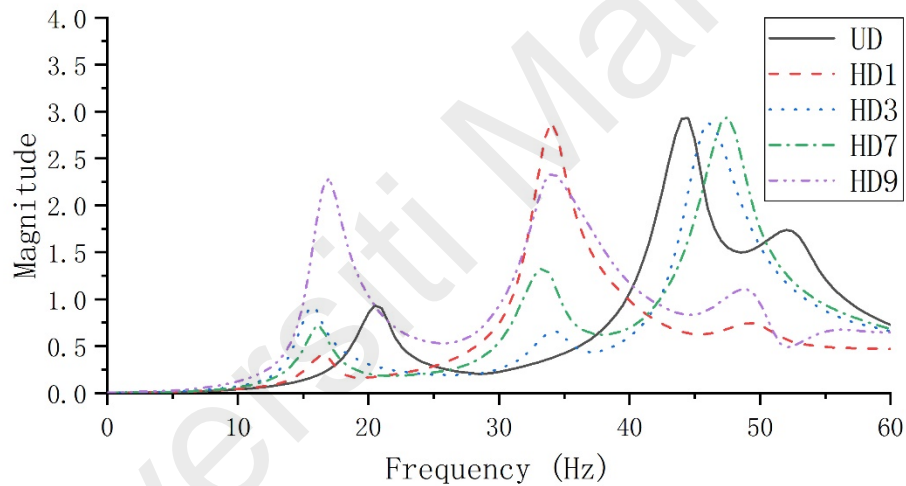


(a) PCA-reduced FRF of LD scenarios

Figure 4.10, continued



(b) PCA-reduced FRF of MD scenarios

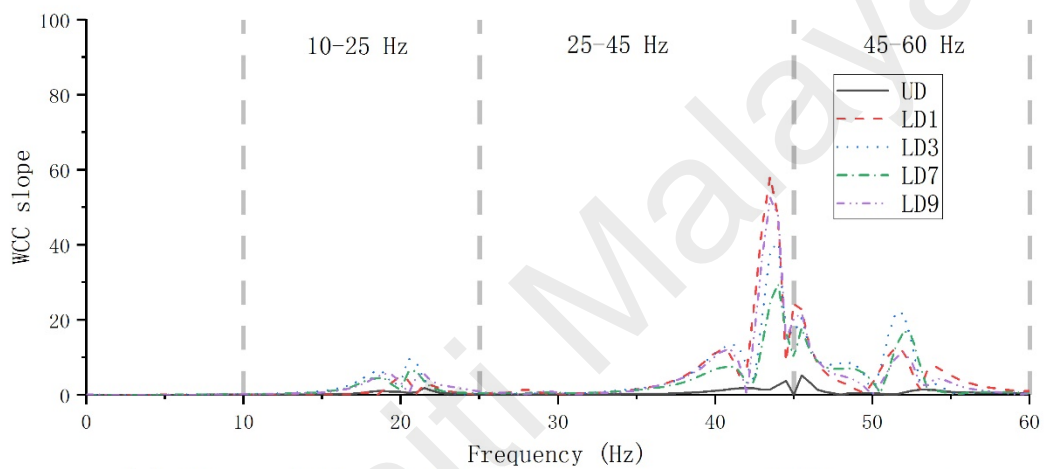


(c) PCA-reduced FRF of HD scenarios

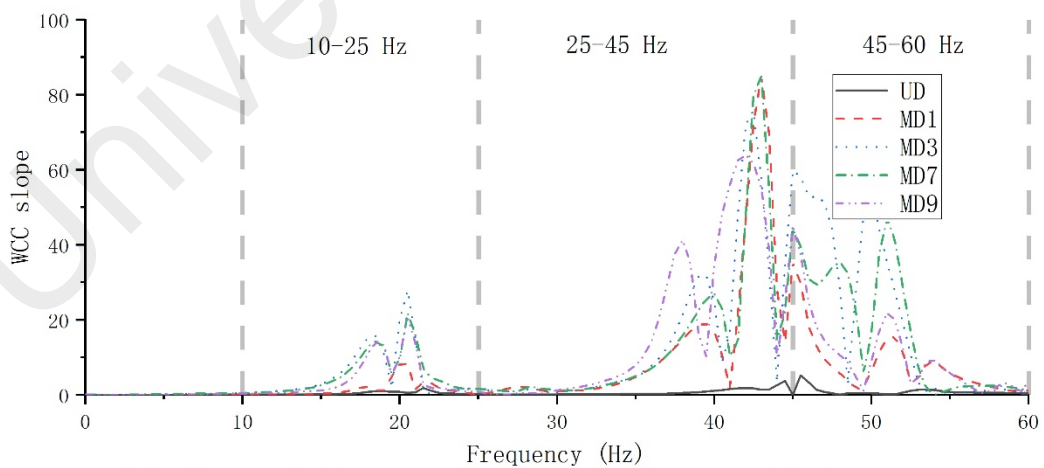
Figure 4.10: PCA-reduced FRF of all scenarios

WCC analysis was then performed on the PCA-reduced FRF. The slope differential value sequences of LD, MD and HD scenarios are plotted in Figure 4.11, in comparison with UD scenario. For the undamaged case, only small fluctuations are observed, which are probably caused by measurement error or noise, indicating that the PCA-reduced FRF of an undamaged scenario is almost identical with that of the benchmark. Meanwhile, the peaks of the damaged slope differential value curves are more distinct, especially near the

natural frequencies, which expressly reflects the shift of the PCA-reduced FRF attributed to structural damage. Three frequency segments, namely 10~25 Hz, 25~45 Hz and 45~60 Hz, were intercepted from the original frequency range. Here 10~25 Hz corresponds to the first mode, 25~45 Hz corresponds to the second mode, and 45~60 Hz corresponds to the third mode. The areas under the curves of slope differential value sequences, as the WCC features, were calculated in each of the three frequency segments and respectively denoted as a_{s1} , a_{s2} and a_{s3} .

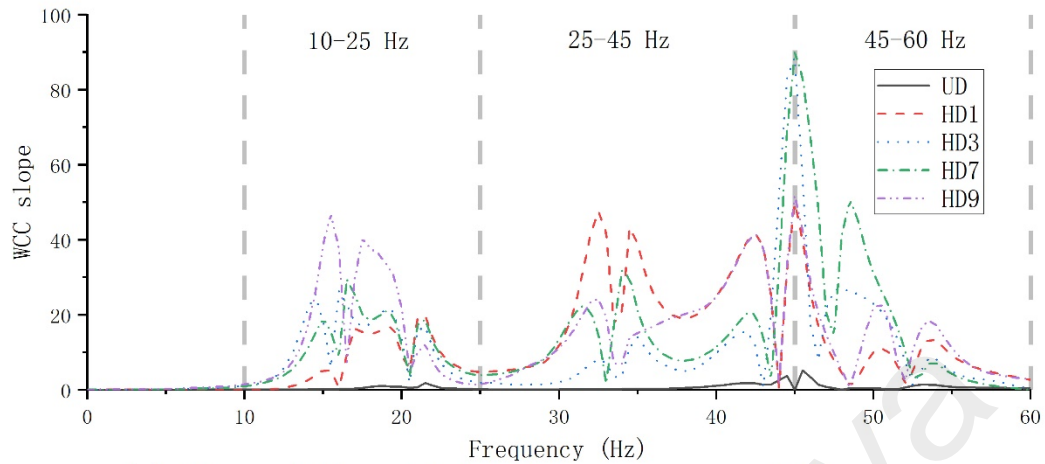


(a) Slope differential value sequences of LD scenarios



(b) Slope differential value sequences of MD scenarios

Figure 4.11, continued



(c) Slope differential value sequences of HD scenarios

Figure 4.11: Slope differential value sequences

To further look into the sensitivity of the WCC analysis, the PCA-WCC features were compared with the horizontal shift of the corresponding resonant peaks in the PCA-reduced FRF under six levels of damage with low severity, which are shown in Tables 4.10, 4.11 and 4.12. It is observed that the horizontal shift of the peaks is very small when damage severity is low. The shift is lower than 5% when there exists nonzero pressure at the damage point, and the shift in the first resonant peak cannot be observed when the pressure is higher than 20 under the current resolution rate. Meanwhile, the PCA-WCC feature a_s shows higher sensitivity. Taking the first mode as an example, although there is no observable shift in the first resonant peak in most cases where the pressure at the damage point is nonzero, the different damage conditions can still result in various values of a_{s1} , which range widely from 14.2 to 98.7. The features of the second and third modes are even more sensitive than the first mode, which respectively range from 41.6 to 559.3, and from 20.8 to 333.5. In fact, for both the PCA-WCC feature a_s and the shift of resonant

peak, the second and third modes tend to be more sensitive than the first mode. However, the feature a_s is more sensitive than the shift of resonant peak.

Table 4.10: Feature a_{s1} in comparison with shift in first resonant peak of PCA-reduced FRF

Damage point	Pressure of damage point	a_{s1}	1 st resonant peak	
			Abscissa of peak	Shift of peak
Point #1	120	14.2	20.5	0%
	100	16.8	20.5	0%
	80	26.1	20.5	0%
	60	36.6	20.5	0%
	40	43.4	20.5	0%
	20	55.4	20.0	2%
Point #3	120	33.2	20.5	0%
	100	61.4	20.5	0%
	80	65.7	20.5	0%
	60	62.6	20.5	0%
	40	77.5	20.5	0%
	20	91.4	20.5	0%
Point #7	120	43.3	20.5	0%
	100	56.6	20.5	0%
	80	65.7	20.5	0%
	60	68.8	20.5	0%
	40	59.5	20.5	0%
	20	98.7	20.5	0%
Point #9	120	17.0	20.5	0%
	100	12.2	20.5	0%
	80	10.2	20.5	0%
	60	10.1	20.5	0%
	40	16.7	20.5	0%
	20	29.1	20.5	0%

Table 4.11: Feature a_{s2} in comparison with shift in second resonant peak of PCA-reduced FRF

Damage point	Pressure of damage point	a_{s2}	2 nd resonant peak	
			Abscissas of peak	Shift of peak
Point #1	120	77.6	44.0	0%
	100	124.6	44.0	0%
	80	241.1	43.5	1%
	60	320.4	43.0	2%
	40	387.8	43.0	2%
	20	559.3	42.0	5%
Point #3	120	66.9	44.0	0%
	100	108.8	44.0	0%
	80	145.9	44.0	0%
	60	163.0	43.5	1%
	40	225.6	43.5	1%
	20	325.0	43.0	2%
Point #7	120	85.9	44.0	0%
	100	113.2	44.0	0%
	80	147.8	44.0	0%
	60	209.4	43.5	1%
	40	275.8	43.5	1%
	20	451.8	42.5	3%
Point #9	120	41.6	44.0	0%
	100	97.3	44.0	0%
	80	147.2	43.5	1%
	60	209.2	43.5	1%
	40	329.7	43.0	2%
	20	541.1	42.0	5%

Table 4.12: Feature a_{s3} in comparison with shift in third resonant peak of PCA-reduced FRF

Damage point	Pressure of damage point	a_{s3}	3 rd resonant peak	
			Abscissas of peak	Shift of peak
Point #1	120	46.4	52.0	0%
	100	81.8	51.5	1%
	80	143.9	51.0	2%
	60	202.2	50.5	3%
	40	237.9	50.5	3%
	20	267.2	50.0	4%
Point #3	120	52.9	52.0	0%
	100	81.4	52.0	0%
	80	121.9	51.5	1%
	60	150.6	51.5	1%
	40	218.1	51.0	2%
	20	333.5	50.0	4%
Point #7	120	55.2	52.0	0%
	100	80.8	52.0	0%
	80	100.2	52.0	0%
	60	148.2	52.0	0%
	40	232.0	51.5	1%
	20	386.4	51.0	2%
Point #9	120	20.8	52.0	0%
	100	47.6	52.0	0%
	80	100.2	51.5	1%
	60	133.0	51.5	1%
	40	190.3	51.0	2%
	20	251.5	50.5	3%

Figure 4.12 clearly illustrates that the location and severity of damage are both the factors that influence the PCA-WCC features. Overall, the value of the PCA-WCC feature increases with the pressure of the damage point decreasing, considering that higher values of a_s refer to larger alterations in the PCA-reduced FRF and larger changes in structural properties. Due to the high sensitivity of the WCC, the measurement error and noise can also lead to the shift in the PCA-reduced FRF and be reflected in the PCA-WCC features. Therefore, even in the undamaged scenario, the value of PCA-WCC is nonzero, yet is usually smaller than damaged scenarios. So it is necessary to delineate a threshold so that damage alarm will only be issued when the PCA-WCC value exceeds it. The dashed line in Figure 4.12 shows the maximum of the a_s among all the collected UD samples. It is found that the a_s measured under the UD scenario may sometimes become larger than the a_s measured when damage takes place. The dashed line, which indicates the upper bound of a_s under UD, can therefore be set as a threshold. Damage can be detected only when the corresponding a_s exceeds the threshold. This means damage can be detected using a_{s2} when the pressure at the damage point is 120 or less (the pressure is reduced by 20% or more). When the pressure is lower than 100 (the pressure is reduced by more than 33.3%), the damage can also be detected by a_{s3} . When the pressure is lower than 40 (the pressure is reduced by 73.3% or more), the damage can then be detected by a_{s1} . Recalling that the LD scenarios in this study correspond to pressure of 40 at the damage point, these PCA-WCC features are all sensitive enough to indicate the LD damage. This also means the MD and HD damage, which are of higher severity, can be detected as well. For cluster analysis, combining a_{s1} , a_{s2} and a_{s3} as the input features could further improve the reliability. Moreover, the combination also helps distinguish the damage with different locations and severity.

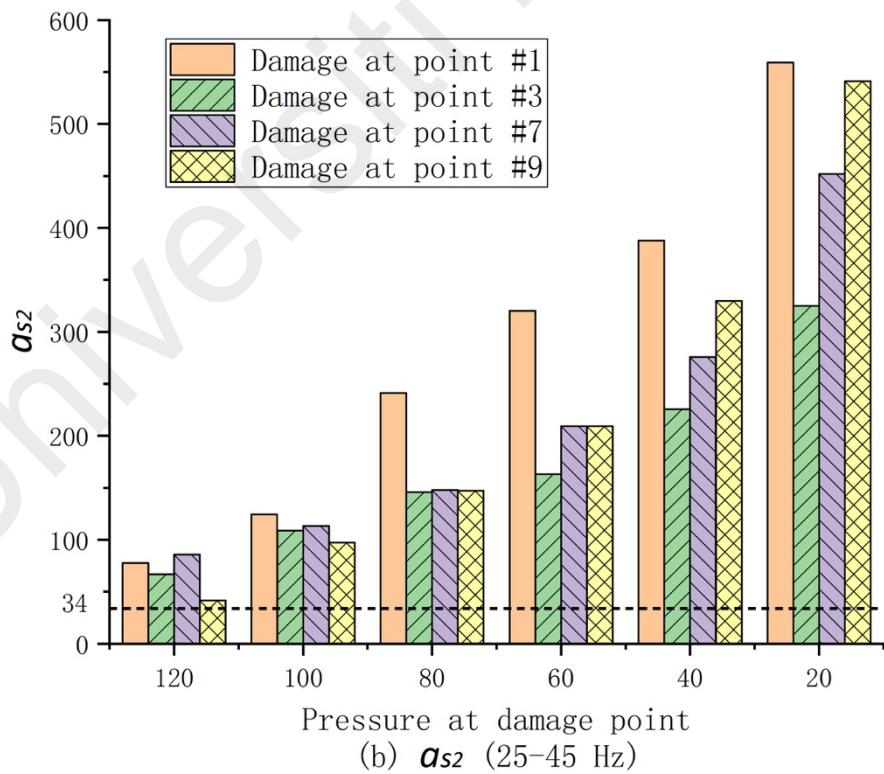
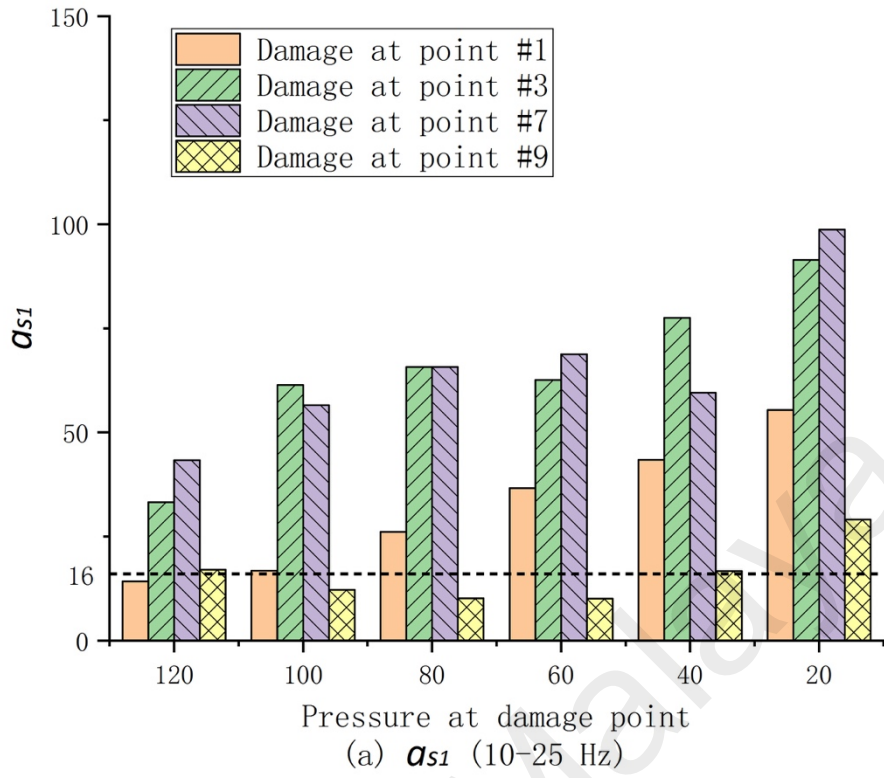


Figure 4.12, continued

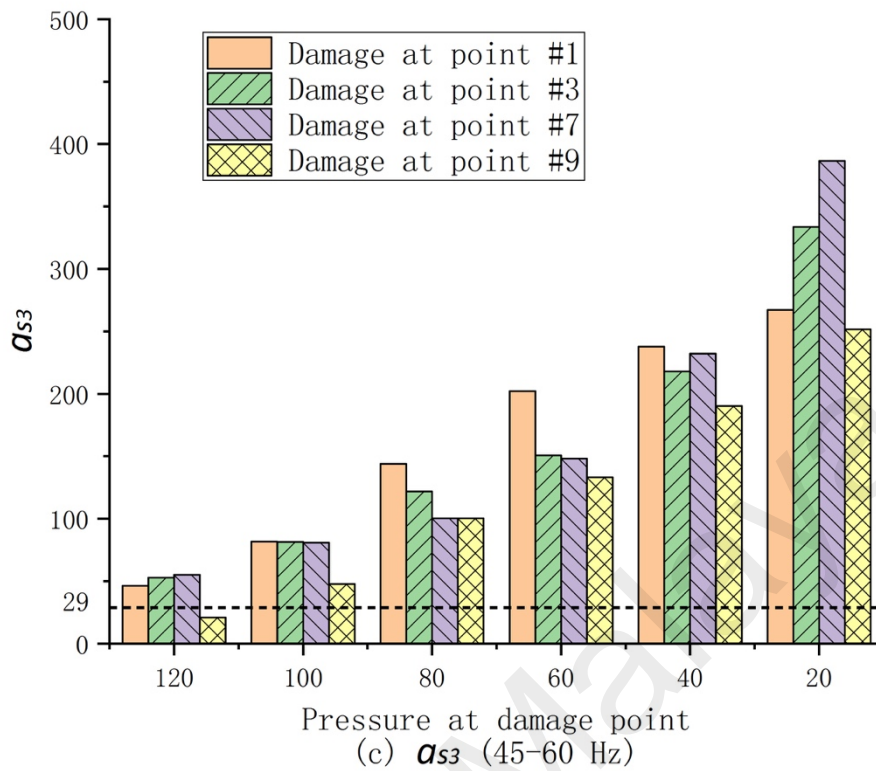


Figure 4.12: PCA-WCC features of different damage states

4.4.2 Hierarchical cluster analysis

The PCA-WCC features of UD, LD, MD and HD samples were normalized and regarded as three-dimensional coordinates of the corresponding node in a complex network. Then, all the nodes of the samples were clustered using the hierarchical clustering method.

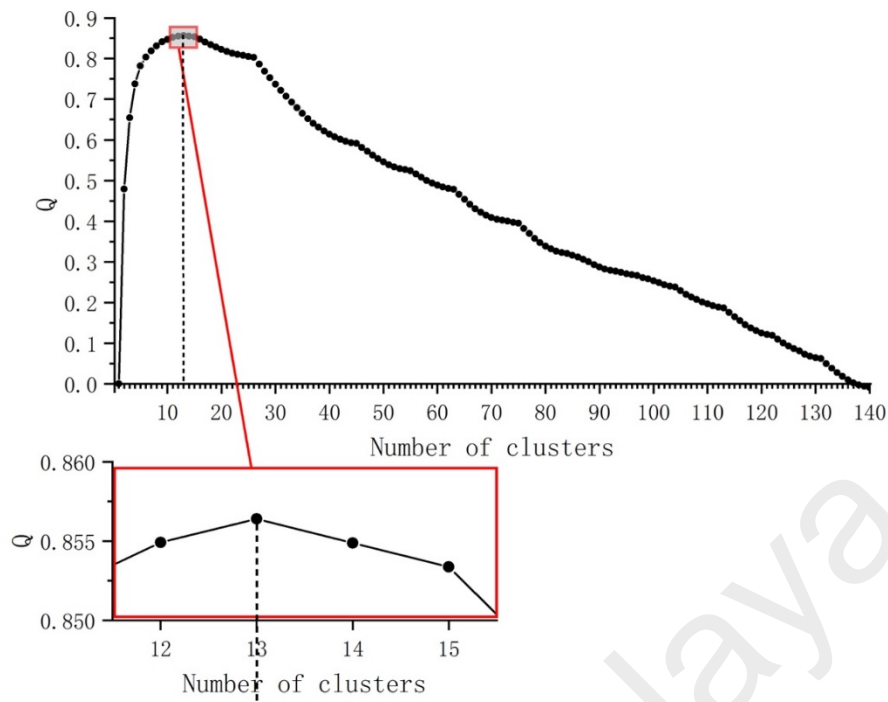


Figure 4.13: Modularity Q in respect to number of clusters

Figure 4.13 shows the modularity Q in respect to the total number of clusters during the merging process and Figure 4.14 is the dendrogram of all the samples. As can be seen from Figure 4.13, the modularity reaches its highest value when the number of clusters is thirteen, when the merging process is terminated. All the samples are therefore divided into thirteen categories. The number of clusters is thus determined as thirteen, which is the same as the actual number of scenarios. In Figure 4.14, the vertical axis of the dendrogram shows the number of each sample, and the samples are linked in pairs from left to right to form the dendrogram. The vertical grey line cuts the tree in the middle, which corresponds to the maximum modularity value and indicates that the algorithm stops merging the remaining clusters and outputs the clustering result. The dendrogram not only reflects the clustering process clearly, but also shows the dissimilarity between the samples. It is noted that the samples within each cluster share the same damage scenario and the thirteen clusters correspond to the thirteen damage scenarios,

respectively. The clustering results are plotted under the coordinates of the normalized PCA-WCC features in Figure 4.15, in which the thirteen clusters can be visually observed. Thus, all the samples are categorized correctly, which proves the effectiveness of the proposed method in the categorization of damage scenarios of the plate structure.

The hierarchical cluster analysis was also tested with the data collected from the new test plate in Appendix A. The PCA-reduced FRF and the WCC slope differential value sequences are respectively shown in Appendix A.5 and Appendix A.6. The PCA-WCC features were calculated in the frequency intervals of 10~20 Hz, 20~40 Hz and 40~60 Hz, as the input of the hierarchical clustering. Appendix A.7 shows that the modularity Q reaches the maximum when the number of clusters is 5, which is the same as the actual number of scenarios. The dendrogram in Appendix A.8 shows that the samples were correctly clustered in terms of their damage scenarios.

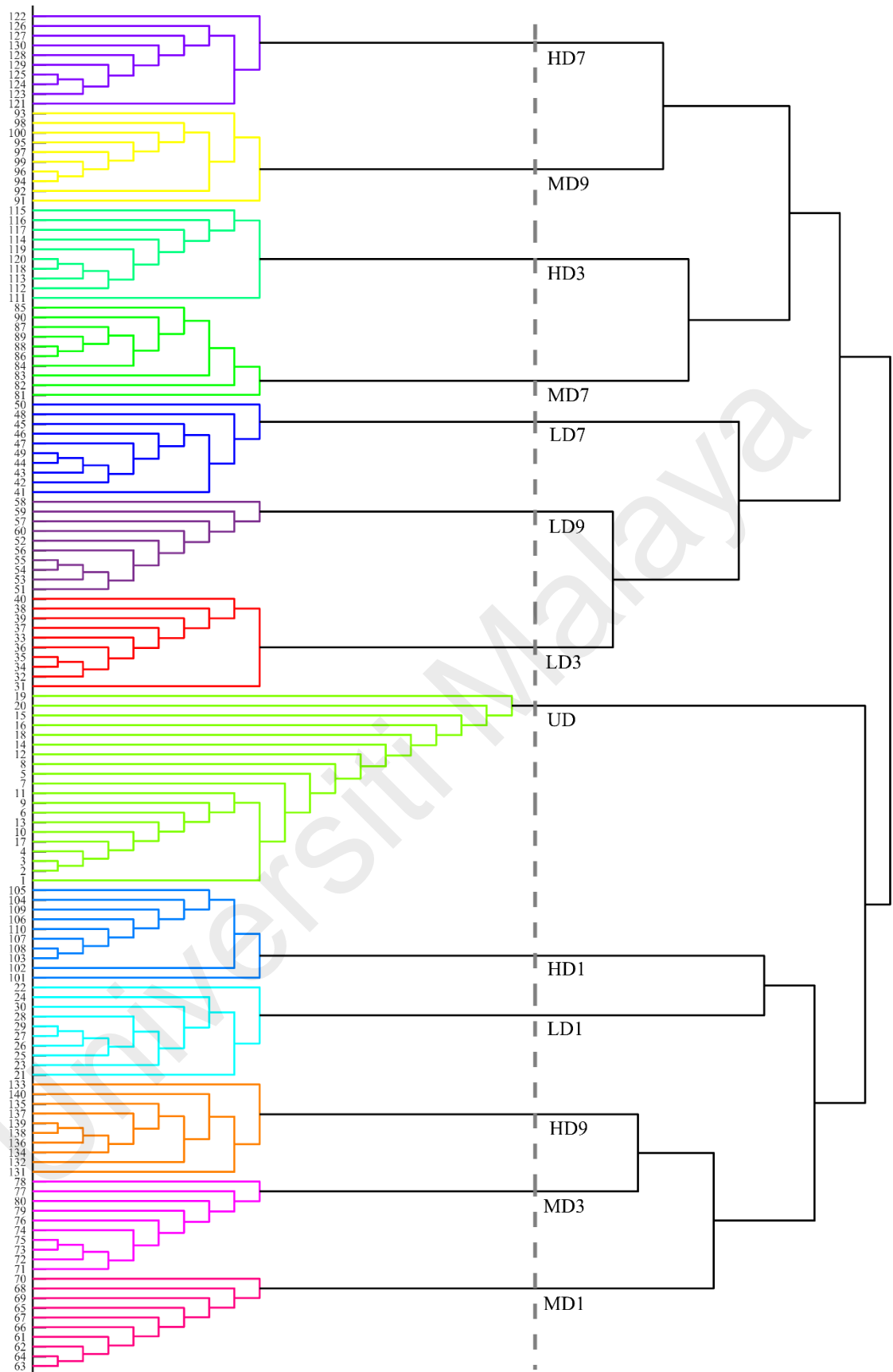


Figure 4.14: Dendrogram

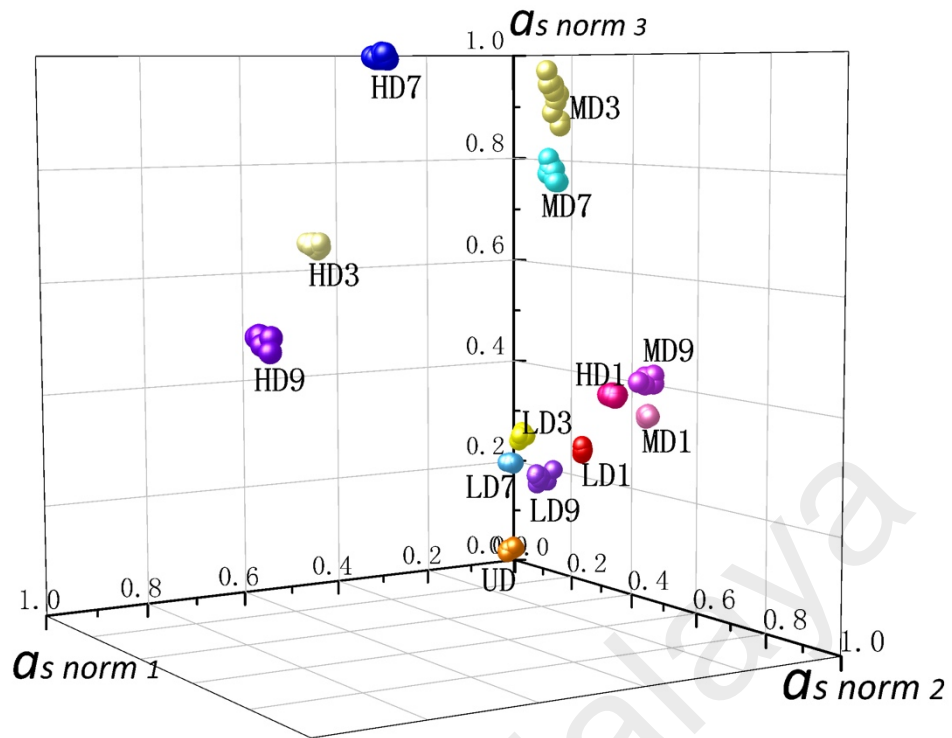


Figure 4.15: Results of hierarchical clustering

The performance of the new hierarchical clustering is then compared with that of the conventional k-means clustering method using ARI, as shown in Table 4.13. ARI takes the value of 1 when the partition based on the actual damage scenarios is consistent with the clustering result. It is noted that no matter how many damage scenarios are included in the samples, the new hierarchical clustering method always gives the correct classification. For k-means clustering, the desired number of clusters, denoted as k , needs to be previously provided. If k is set to match the actual number of damage scenarios n , the ARI of the k-means result can reach or be very close to 1, which is almost as good as the new hierarchical clustering. However, the number of actual damage scenarios is usually not available in reality. A more practical approach is to set $k = 2$, (i.e. healthy and faulty). Then the samples are expected to be classified into two categories by k-means clustering method, the group of UD scenario and the group of other damaged scenarios.

The results in Table 4.13 show that this method is effective when there are fewer types of damage scenarios. However, when more than one level of severity is involved, the performance of k-means clustering is not good. Therefore, the new hierarchical clustering method is more advantageous than the conventional k-means clustering method.

Table 4.13: ARI performance of new hierarchical clustering and k-means clustering

No. of scenarios (n)	ARI performance		
	k-means ($k = 2$)	k-means ($k = n$)	Hierarchical clustering
2 (UD, LD1)	1.00	1.00	1.00
2 (UD, LD3)	1.00	1.00	1.00
2 (UD, LD7)	1.00	1.00	1.00
2 (UD, LD9)	1.00	1.00	1.00
5 (UD, LD)	1.00	1.00	1.00
5 (UD, MD)	1.00	1.00	1.00
5 (UD, HD)	1.00	1.00	1.00
9 (UD, LD, MD)	0.02	0.88	1.00
9 (UD, LD, HD)	0.02	1.00	1.00
9 (UD, MD, HD)	0.62	1.00	1.00
13 (UD, LD, MD, HD)	0.08	0.92	1.00

This unsupervised hierarchical clustering method can be a promising alternative for damage detection. For example, modal analysis can be periodically performed on the monitored structure, and the PCA-WCC features are calculated and saved, followed by cluster analysis carried out on the saved data. In the beginning, the historical data set only includes one cluster of the undamaged samples because the monitored structure is under good condition. When damage occurs, the new samples measured under the damaged state also come in for clustering, which are distinct from the undamaged samples. The data set will be divided into different clusters and damage can therefore be alarmed. It is believed that the proposed detection method is theoretically applicable for any damage types and structures, as long as the damage causes changes in the dynamic characteristics and consequently results in substantial changes in PCA-WCC features.

4.4.3 Damage identification using PCA-reduced FRF

Since hierarchical cluster analysis has categorized the samples into clusters of different damage scenarios, the following work is to specifically identify the damage severity and location of each cluster. The PCA-reduced FRF, which is simple yet preserves important dynamic characteristics, helps to accomplish this goal.

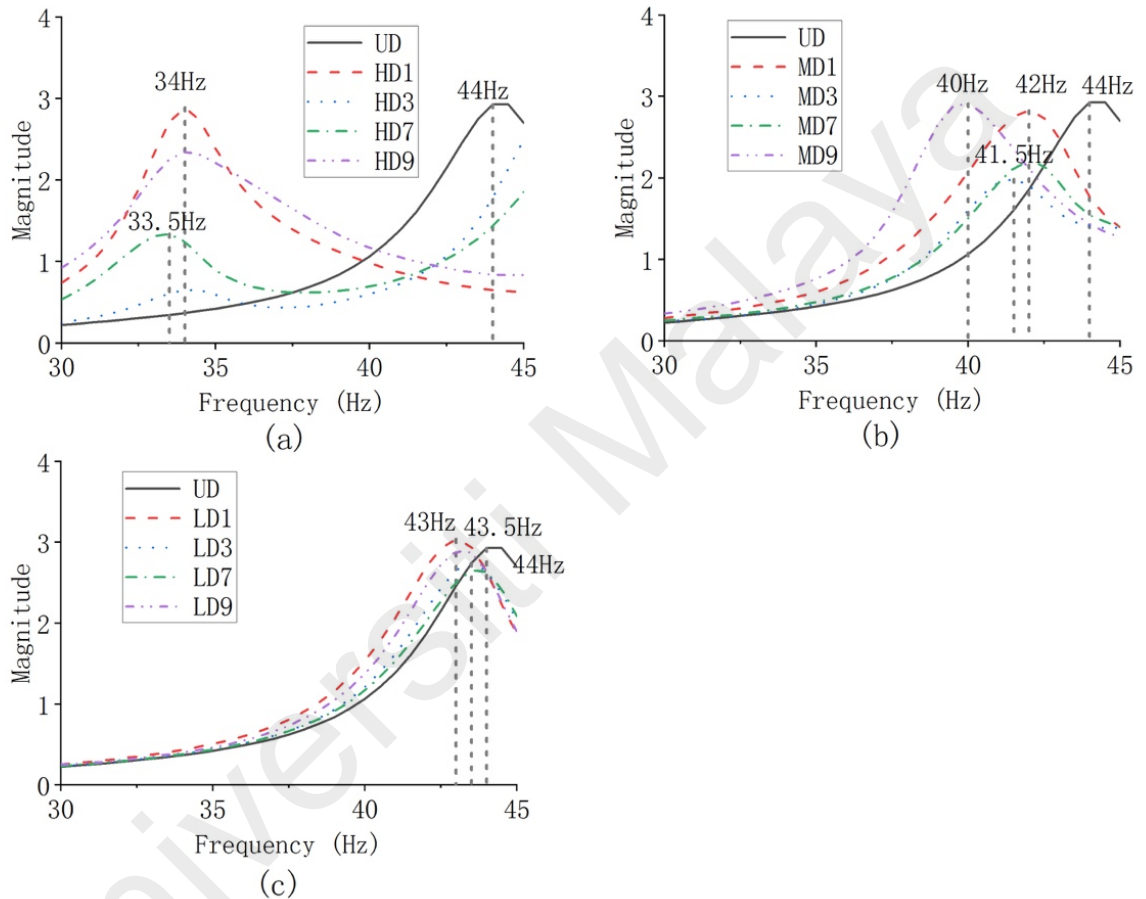


Figure 4.16: Second resonant peaks of PCA-reduced FRFs

It has been discussed in the previous sections that damage leads to the shift of the resonant peaks in the PCA-reduced FRF. This phenomenon can be used to indicate the damage severity. The second resonant peak is a more favorable choice than the first one because of its higher sensitivity. Figure 4.16 shows the second resonant peaks of the PCA-reduced FRFs in the frequency range of 30-45 Hz. As shown in the figure, in the HD

scenarios, the shift becomes more obvious, where these peaks move to the left by more than 10 Hz, and the decreases in their abscissas are approximately 23-24%. While in the MD scenarios, the second resonant peaks move smaller distances, from 2 Hz to 4 Hz, and the abscissas of the peaks decrease by 5-9%. In the LD scenarios, the shift in the second resonant peaks is no larger than 1 Hz, and the abscissas of the peaks decrease by 2% or less. In fact, the abscissa of the resonant peak is the approximation of the corresponding natural frequency. Damage with higher severity causes a greater decrease in the natural frequency, and thus leads to larger shift in the resonant peak. This is helpful in estimating and quantifying the damage severity. In this case, high severity damage states represent the worst damage scenario giving the damage index of 1 (i.e. normalization of the reduction in the abscissa of the resonant peak), and the damage indices of the samples of all the damage scenarios are calculated and shown in Table 4.14. This can help to quantify the low severity damage states with the damage index of as low as 0.05, indicating this scheme is sensitive in damage severity identification.

Table 4.14: Reduction in second natural frequency and damage indices

Damage scenario	Shift of 2nd resonant peak	Percentage shift	Damage index
UD	0	0%	0
HD1	10	23%	0.95
HD3	10	23%	0.95
HD7	10.5	24%	1.00
HD9	10	23%	0.95
MD1	2	5%	0.19
MD3	2.5	6%	0.24
MD7	2	5%	0.19
MD9	4	9%	0.38
LD1	1	2%	0.10
LD3	0.5	1%	0.05
LD7	0.5	1%	0.05
LD9	1	2%	0.10

The damage localization can be carried out using the magnitude of the resonant peaks in PCA-reduced FRFs with the knowledge of the mode shape. Figure 4.17 shows the PCA-reduced FRFs in the frequency range of 10-45 Hz, covering the resonant peaks of the first and second modes. The magnitude of the first and second resonant peaks of different damage scenarios and their changes with reference to the undamaged state are tabulated in Table 4.15. In the table, the change in the magnitude refers to the percentage increase (or decrease) in the magnitude of the resonant peak after the shift of the PCA-reduced FRF compared with the undamaged condition. A positive correlation is found between the displacement at the impact point (i.e. point #9 in this work) in the mode shape plot and the magnitude of the corresponding resonant peak of the PCA-reduced FRF, (i.e. the higher displacement at the impact point corresponds to the larger magnitude of the resonant peak). We first illustrate this correlation using the HD scenarios, where the alterations are more expressive. Figure 4.18 is the first mode shapes of the plate with damage at different locations. The first mode of the plate is the heaving mode and the four vertices of the plate are displaced equally when there is no damage. When damage takes place at any corner of the plate, the plate is tilted toward the damage point as shown in the mode shapes in Figure 4.18.

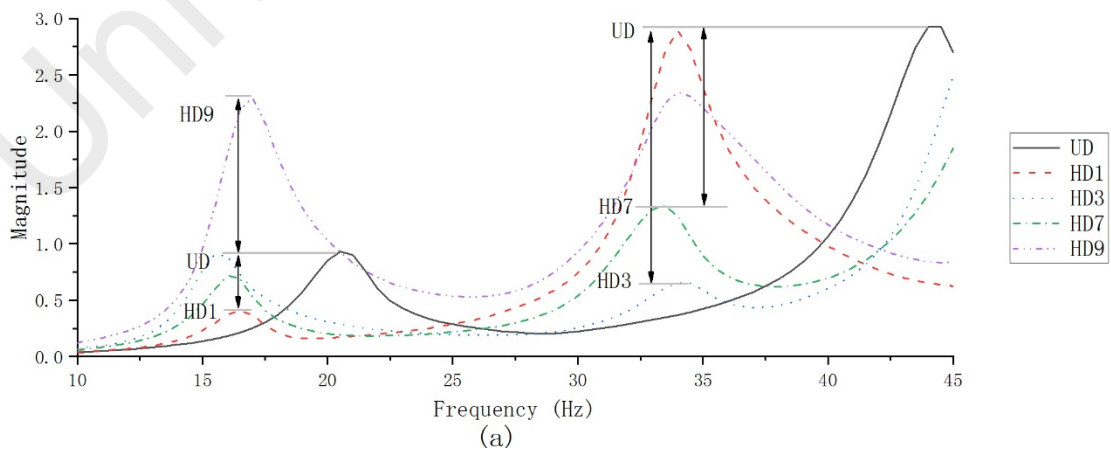


Figure 4.17, continued

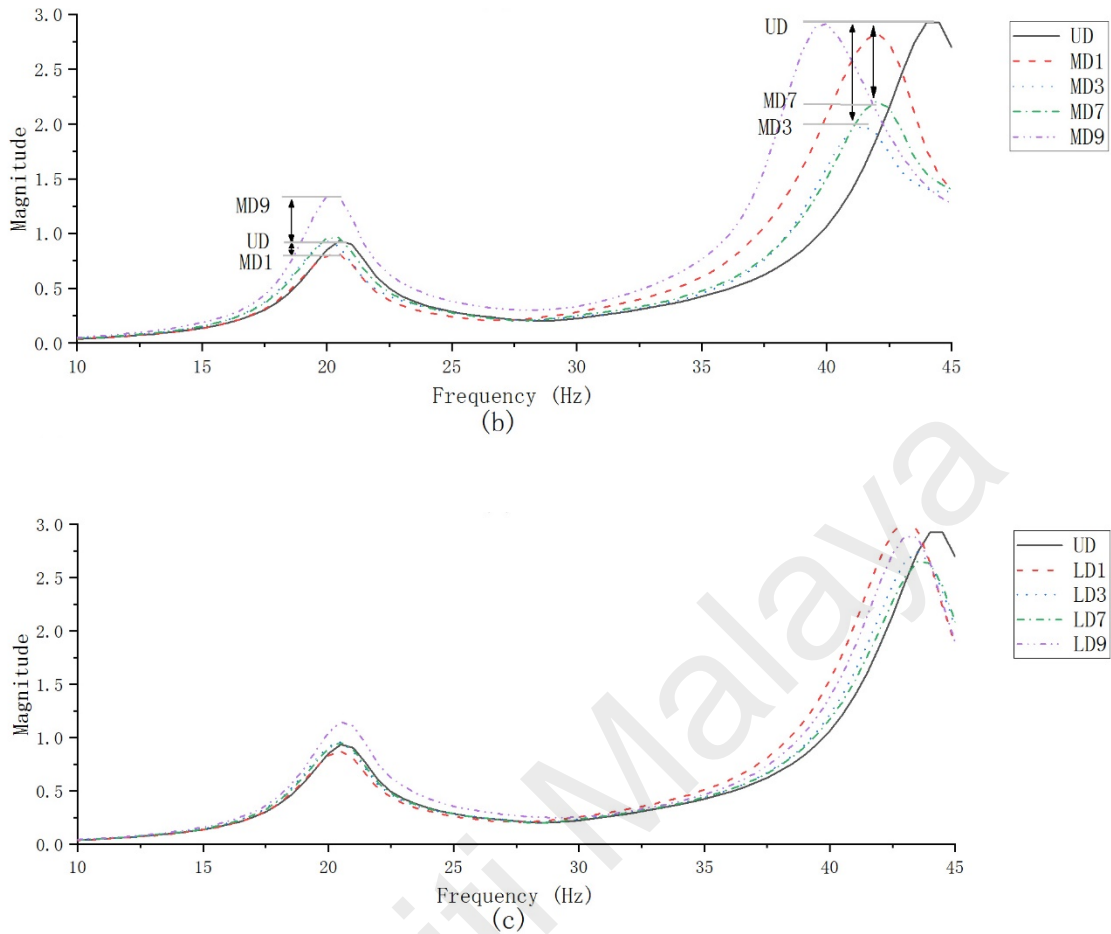


Figure 4.17: First and second resonant peaks of PCA-reduced FRFs

Table 4.15: Magnitude of first and second resonant peaks

Damage scenario	1 st resonant peak		2 nd resonant peak	
	Magnitude	Change in magnitude	Magnitude	Change in magnitude
UD	0.9	0%	2.9	0%
HD1	0.4	-56%	2.9	0%
HD3	0.9	0%	0.7	-76%
HD7	0.7	-22%	1.3	-55%
HD9	2.3	156%	2.3	-21%
MD1	0.7	-22%	2.8	-3%
MD3	0.9	0%	2.0	-31%
MD7	1.0	11%	2.2	-24%
MD9	1.3	44%	2.9	0%
LD1	0.9	0%	3.0	3%
LD3	1.0	11%	2.7	-7%
LD7	1.0	11%	2.7	-7%
LD9	1.1	22%	2.9	0%

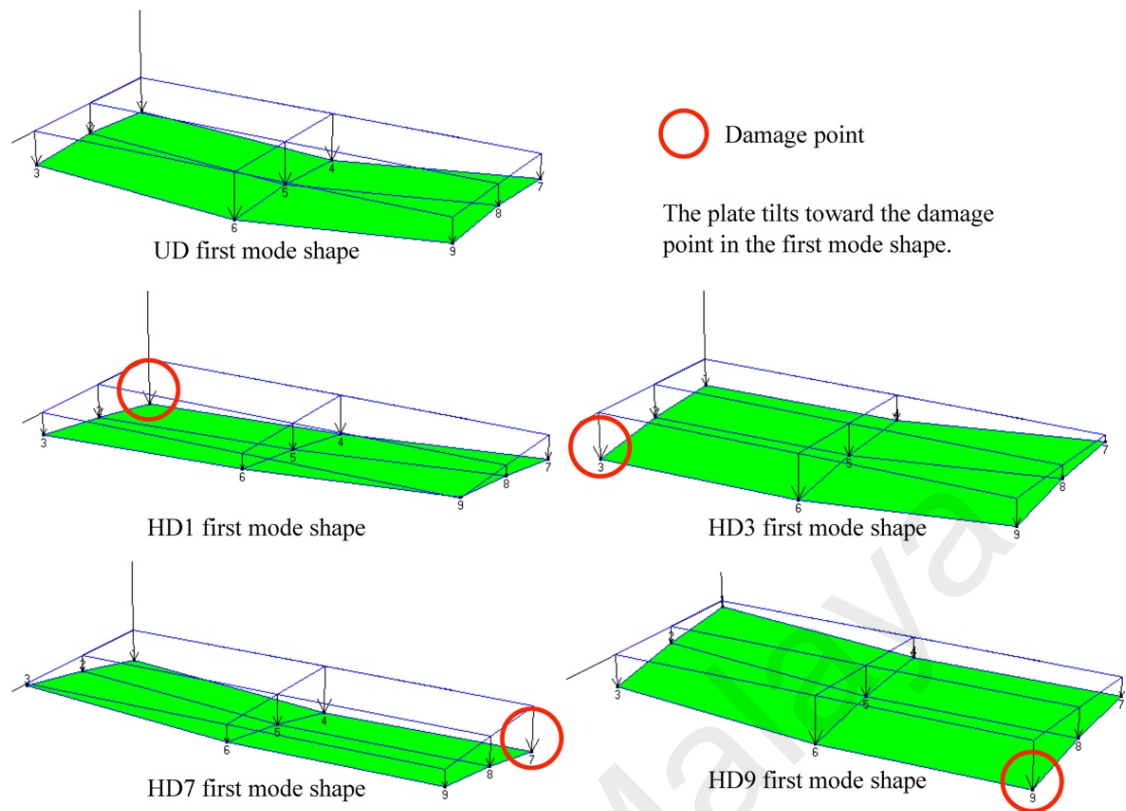


Figure 4.18: First mode shapes of plate under different damage states

Figure 4.19 compares the first mode shapes of the plate with the PCA-reduced FRF, demonstrating the correlation between the displacement and the impact point (i.e. point #9), and the magnitude of the first resonant peak. When damage occurs at the point #9, the displacement of the first mode shape at the impact point #9 is significantly larger than that of the undamaged scenario. Correspondingly, the magnitude of the first resonant peak of HD9 is also greatly increased by 156%, compared with that of UD showing the similar trend with large mode shape displacement at the impact point #9 as described above. Meanwhile, when damage occurs at point #1, which is diagonally opposite to the impact point #9, the plate is tilted toward the point #1 leaving the displacement of the point #9 becomes very small. Correspondingly, this is quantified through the magnitude of the first resonant peak of HD1 which largely decreases by 56%, compared with UD. As to HD3 and HD7, no apparent changes in the displacement of point #9 is observed in the first

mode shapes compared with UD, and the magnitude of the first resonant peaks only changes by 0% and 22%, which are far smaller than the changes in HD1 and HD9. Figure 4.20 shows the second mode shapes of the plate, together with the PCA-reduced FRF near the second resonant peaks. The second mode of the plate is the symmetric rolling movement around the longitudinal axis (as shown in Figure 3.3). Similarly, when damage takes place at any corner of the plate, the plate's rolling movement becomes asymmetric and is tilted toward the damage point as shown in the second mode shapes. It leads to different changes in the displacement at impact point #9 of the second mode shape and makes it suitable to identify and differentiate different damage scenarios. The displacement at point #9 of HD3 is found to be a nodal point with the minimum response while a relatively larger displacement at point #9 is observed in HD7. Correspondingly, a larger decrease is found in the magnitude of the second resonant peak of PCA-reduced FRF in HD3 scenario (i.e. 76% reduction) as compared with UD. Meanwhile, for HD7, the second resonant peak shows relatively lower reduction (i.e. 55%). The same trend of the changes in PCA-reduced FRFs is also found in Figure 4.17 (b) for MD damage. However, as to the LD cases in Figure 4.17 (c), the change in the magnitude of the peaks is not obvious, making it difficult to locate the LD damage, which is the limitation of the PCA-reduced FRF.

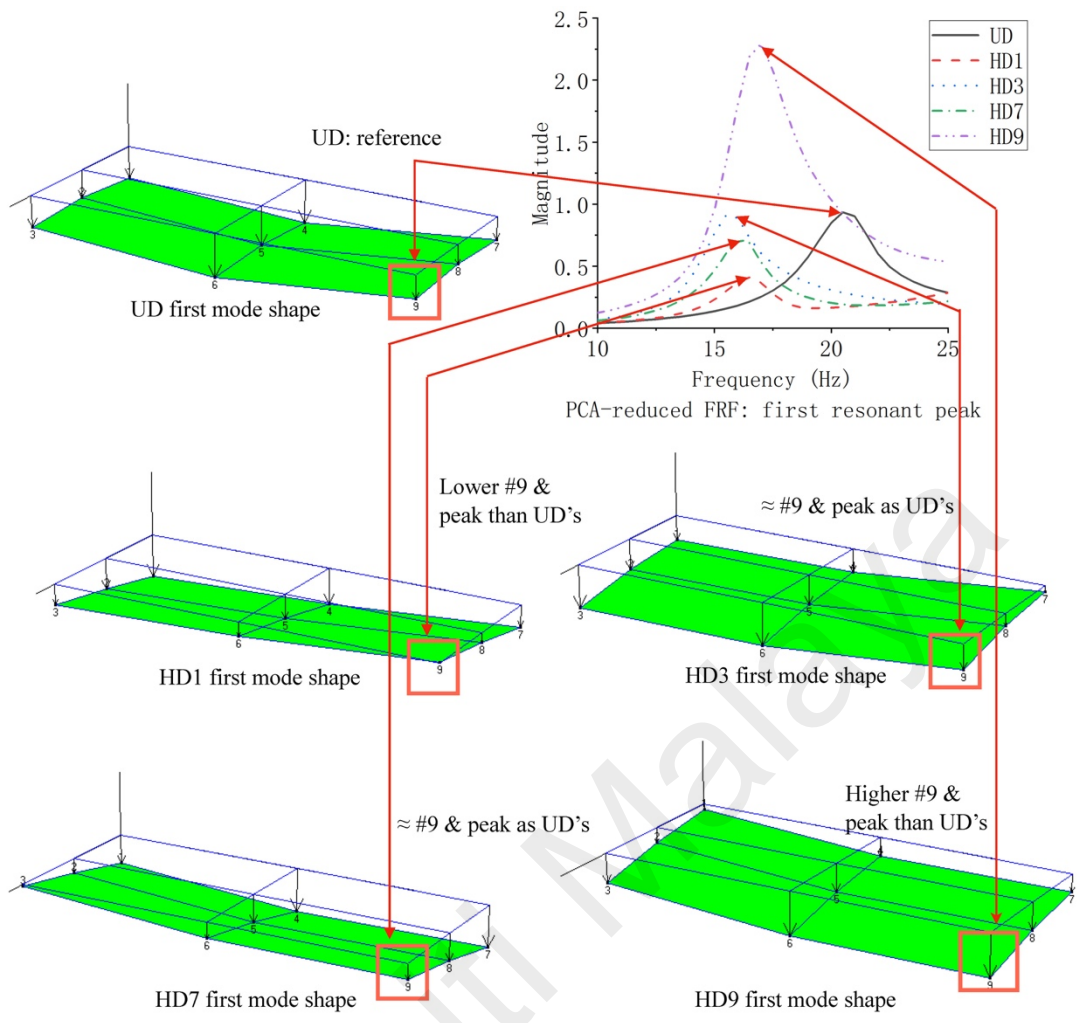


Figure 4.19: First mode shapes of plate with PCA-reduced FRF near first resonant peaks

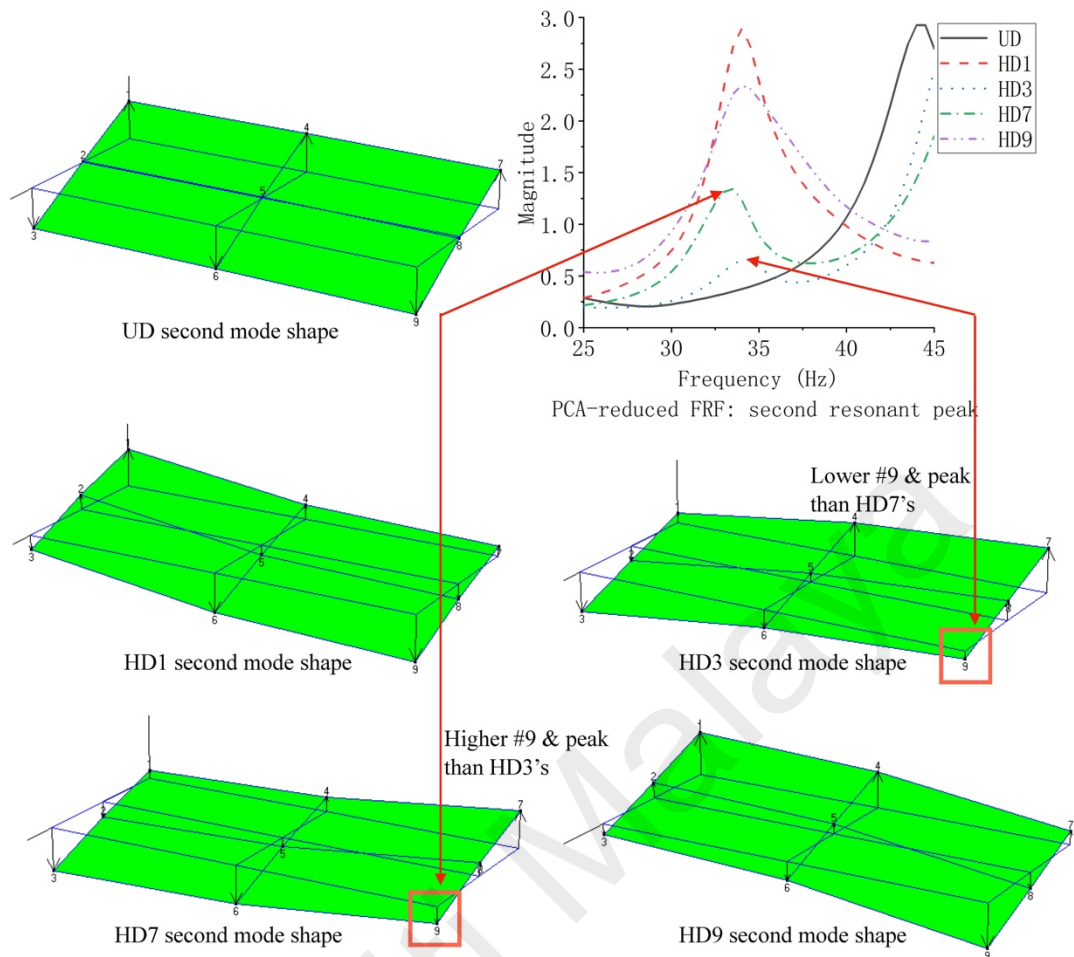


Figure 4.20: Second mode shapes of plate with PCA-reduced FRF near second resonant peaks

To summarize, the HD and MD damage can be located through the first mode shape movement in which the plate tends to tilt toward the damage point. In addition, the changes in the displacement at the impact point #9 of the mode shape show a positive correlation with the magnitude of the resonant peak in the PCA-reduced FRF, making it suitable to quantitatively locate the damages with a higher confidence level. Damage at points #1 and #9 are identified according to the changes in the magnitude of the first resonant peak in the PCA-reduced FRF. When the magnitude of the first resonant peak is found greatly reduced (by more than 50% for HD and more than 20% for MD), the damage location is determined to be point #1. When the magnitude of the first peak is

greatly increased (by more than 100% for HD and more than 40% for MD), the damage location is identified to be point #9. When the magnitude change is small (within 25% for HD and within 15% for MD), the damage location is point #3 or point #7. Subsequently, the second resonant peak is suitable to distinguish damage at point #3 and point #7. When a larger decrease is observed in the magnitude of the second resonant peak (by more than 75% for HD and more than 30% for MD), the damage is located at point #3. Meanwhile, a relatively smaller decrease (less than 60% for HD and less than 25% for MD) in the magnitude of the second resonant peak indicates damage at point #7. The remaining two damage cases are thus identified. The same trend in the magnitude of resonant peaks can also be found from the new test plate according to Appendix A.9, indicating that the damage localization is also applicable to other plates.

4.5 Summary

In the supervised learning based damage identification method proposed in this work, the input features of the network are constructed directly from the measured raw FRFs, which do not require tedious processing, and are more cost-effective in terms of the hardware and network computation after optimization of the measurement points. Besides, the BP network is trained to automatically establish the mapping between the input feature vector and damage state without further analyzing the mechanical properties of the structure, which is more convenient in practice. However, the disadvantage is that it does not work well in identifying damage with low severity. And the complete training samples are necessary for supervised learning, which is not realistic in some practical situations.

The advantages of the unsupervised learning based damage identification method in this study lie in the following two aspects. First, features constructed using PCA and WCC analysis are very sensitive to structural damage. Second, unlike traditional

clustering algorithms where the number of categories needs to be pre-defined, the number of clusters is automatically determined in the new hierarchical clustering algorithm. After the samples are classified into clusters of different damage scenarios, the identification of the damage severity and location of each cluster relies on the analysis of the PCA-reduced FRF and mode shapes.

To summarize, when it is necessary to identify the specific damage location and severity of complex structures, and the complete training samples are available, the supervised learning method using BP network is more suitable. Meanwhile, the new hierarchical clustering method with PCA and WCC analysis is suitable when a set of samples of unknown damage type needs to be categorized and high sensitivity is desired for detection.

Universiti Malaysia

CHAPTER 5: CONCLUSIONS

5.1 Conclusions

In this work, ISMA de-noising technique was successfully applied to extracting FRFs under the in-service condition. Two damage identification schemes were developed using the FRF-based features, incorporated with supervised and unsupervised learning methods respectively. The conclusions are summarized as follows.

The ISMA method is effective in the modal analysis under the operational condition. In the measurement of FRF, the value of FRAC between the FRF obtained by ISMA and EMA exceeds 0.993 in all damage scenarios, which shows very high similarity between the FRFs obtained by these two means, indicating that the de-noising method of ISMA provides static comparable FRF data during the in-service condition. In addition, the natural frequency and mode shape obtained by ISMA are also comparable to EMA results, which means ISMA is also applicable for modal parameter extraction under the in-service condition.

In the proposed damage identification scheme using supervised learning, it has been proved that the trained BP network can successfully identify damage location and severity with the testing data collected by ISMA, which allows the damage identification to be carried out without shutting down the test machine. For HD and MD scenarios of the Perspex plate, an overall accuracy can reach 100% when all five measurement points are used. With the input features optimized by mode shape assessment, 100% accuracy can also be achieved with only two measurement points, which makes the scheme more cost-effective in terms of the accelerometer hardware and computational complexity of network training.

In the proposed damage identification scheme using unsupervised learning, the WCC analysis yields a more sensitive feature that reflects the shift in the PCA-reduced FRF

attributed to structural damage, which are promising alternatives for damage detection. The results of hierarchical cluster analysis show that the samples can be automatically divided into clusters, so that the samples with the same damage scenario are correctly grouped into the same cluster. In terms of damage severity and location identification, it is found that higher severity of damage causes a larger shift in the resonant peaks of the PCA-reduced FRF, and the proposed scheme is sensitive to detect damage severity with damage index as low as 0.05. In addition, for the first and second modes of the plate, the magnitude of the peak in the PCA-reduced FRF is positively correlated with the displacement of the impact point in the corresponding mode shape. These findings help estimate the severity and locate the damage of the test plate.

The supervised learning based damage identification scheme is preferred when it is necessary to identify the specific damage location and severity of complex structures with the complete training samples available. Meanwhile, the unsupervised clustering method with WCC analysis is more suitable when a set of samples of unknown damage types need to be classified and high sensitivity is desired for damage detection.

5.2 Future work

It is noted that the supervised learning method using FRF change is less sensitive in identifying low severity damage. The WCC features, which have been proved more sensitive to damage, can be used instead of FRF change to improve the performance. Meanwhile, the proposed unsupervised learning alone is only good for detecting damage and clustering the measured data in terms of their damage scenarios, rather than indicating the particular damage state of each cluster. Therefore, in the future work, a hybrid method is going to be established, combining the unsupervised damage detection and then supervised damage identification, to explore the quantitative relationship between the WCC features and damage severity and give predictions to the clustering results.

Additionally, this study mainly focuses on the algorithms of the scheme. The current work is only applicable to the plate-like structure which exhibits the same dynamic characteristics as an automobile. In the future work, the proposed method will be further explored on other types of structures (e.g. the beam-like structure and the piping) and on more complex systems (e.g. real rotating machine module where the ambient noise is significant).

Universiti Malaya

REFERENCES

- Baghiee, N., Esfahani, M. R., & Moslem, K. (2009). Studies on damage and FRP strengthening of reinforced concrete beams by vibration monitoring. *Engineering Structures*, 31(4), 875-893. doi:10.1016/j.engstruct.2008.12.009
- Brunton, S. L., & Kutz, J. N. (2019). *Data-Driven Science and Engineering: Machine Learning, Dynamical Systems, and Control*. Cambridge: Cambridge University Press.
- Bull, L. A., Worden, K., Fuentes, R., Manson, G., Cross, E. J., & Dervilis, N. (2019). Outlier ensembles: A robust method for damage detection and unsupervised feature extraction from high-dimensional data. *Journal of Sound and Vibration*, 453, 126-150. doi:10.1016/j.jsv.2019.03.025
- Cao, M. S., Ding, Y. J., Ren, W. X., Wang, Q., Ragulskis, M., & Ding, Z. C. (2017). Hierarchical Wavelet-Aided Neural Intelligent Identification of Structural Damage in Noisy Conditions. *Applied Sciences-Basel*, 7(4), 20. doi:10.3390/app7040391
- Carden, E. P., & Fanning, P. (2004). Vibration based condition monitoring: A review. *Structural Health Monitoring*, 3(4), 355-377. doi:10.1177/1475921704047500
- Cawley, P., & Adams, R. D. (1979). LOCATION OF DEFECTS IN STRUCTURES FROM MEASUREMENTS OF NATURAL FREQUENCIES. *Journal of Strain Analysis for Engineering Design*, 14(2), 49-57. doi:10.1243/03093247v142049
- Chance, J., Tomlinson, G., & Worden, K. (1994). *A simplified approach to the numerical and experimental modelling of the dynamics of a cracked beam*. Paper presented at the Proceedings-SPIE the International Society for Optical Engineering.
- Chao, O. Z., Cheet, L. H., Yee, K. S., Rahman, A. G. A., & Ismail, Z. (2016). An experimental investigation on the effects of exponential window and impact force level on harmonic reduction in impact-synchronous modal analysis. *Journal of Mechanical Science and Technology*, 30(8), 3523-3532. doi:10.1007/s12206-016-0712-6
- Chen, H. L., Spyrakos, C. C., & Venkatesh, G. (1995). EVALUATING STRUCTURAL DETERIORATION BY DYNAMIC-RESPONSE. *Journal of Structural Engineering-Asce*, 121(8), 1197-1204. doi:10.1061/(asce)0733-9445(1995)121:8(1197)
- Chen, S. S., & Kim, S. K. (1994, Feb 14-16). *NEURAL-NETWORK-BASED SIGNAL MONITORING IN A SMART STRUCTURAL SYSTEM*. Paper presented at the Conference on Smart Sensing, Processing, and Instrumentation, Orlando, FL.
- Dackermann, U., Smith, W. A., & Randall, R. B. (2014). Damage identification based on response-only measurements using cepstrum analysis and artificial neural networks. *Structural Health Monitoring-an International Journal*, 13(4), 430-444. doi:10.1177/1475921714542890

- Dewangan, P., Parey, A., Hammami, A., Chaari, F., & Haddar, M. (2020). Damage detection in wind turbine gearbox using modal strain energy. *Engineering Failure Analysis, 107*, 27. doi:10.1016/j.engfailanal.2019.104228
- Elkordy, M. F., Chang, K. C., & Lee, G. C. (1994). Application of Neural Networks in Vibrational Signature Analysis. *Journal of Engineering Mechanics-Asce, 120*(2), 250-265. doi:10.1061/(Asce)0733-9399(1994)120:2(250)
- Goldstein, M., & Uchida, S. (2016). A Comparative Evaluation of Unsupervised Anomaly Detection Algorithms for Multivariate Data. *PLoS ONE, 11*(4), 31. doi:10.1371/journal.pone.0152173
- Goodfellow, I., Bengio, Y., Courville, A., & Bengio, Y. (2016). *Deep learning* (Vol. 1): MIT press Cambridge.
- Guo, H. Y., & Li, Z. L. (2014). Structural Multi-Damage Identification Based on Modal Strain Energy Equivalence Index Method. *International Journal of Structural Stability and Dynamics, 14*(7), 17. doi:10.1142/s021945541450028x
- Hadzima-Nyarko, M., Nyarko, E. K., & Moric, D. (2011). A neural network based modelling and sensitivity analysis of damage ratio coefficient. *Expert Systems with Applications, 38*(10), 13405-13413. doi:10.1016/j.eswa.2011.04.169
- Hearn, G., & Testa, R. B. (1991). Modal-Analysis for Damage Detection in Structures. *Journal of Structural Engineering-Asce, 117*(10), 3042-3063. doi:10.1061/(Asce)0733-9445(1991)117:10(3042)
- Hossain, M. S., Chao, O. Z., Ismail, Z., Noroozi, S., & Khoo, S. Y. (2017). Artificial neural networks for vibration based inverse parametric identifications: A review. *Applied Soft Computing, 52*, 203-219. doi:10.1016/j.asoc.2016.12.014
- Hou, R. R., & Xia, Y. (2021). Review on the new development of vibration-based damage identification for civil engineering structures: 2010-2019. *Journal of Sound and Vibration, 491*. doi:10.1016/j.jsv.2020.115741
- Hubert, L., & Arabie, P. (1985). COMPARING PARTITIONS. *Journal of Classification, 2*(2-3), 193-218. doi:10.1007/bf01908075
- Ismail, Z., Razak, H. A., & Rahman, A. G. A. (2006). Determination of damage location in RC beams using mode shape derivatives. *Engineering Structures, 28*(11), 1566-1573. doi:10.1016/j.engstruct.2006.02.010
- Janssens, O., Slavkovikj, V., Vervisch, B., Stockman, K., Loccufier, M., Verstockt, S., . . . Van Hoecke, S. (2016). Convolutional Neural Network Based Fault Detection for Rotating Machinery. *Journal of Sound and Vibration, 377*, 331-345. doi:10.1016/j.jsv.2016.05.027
- Jolliffe, I. T., & Springer-Verlag. (2002). *Principal Component Analysis*: Springer.
- Kim, J. T., & Stubbs, N. (1995). MODEL-UNCERTAINTY IMPACT AND DAMAGE-DETECTION ACCURACY IN PLATE GIRDER. *Journal of Structural*

Engineering-Asce, 121(10), 1409-1417. doi:10.1061/(asce)0733-9445(1995)121:10(1409)

- Li, J. C., Dackermann, U., Xu, Y. L., & Samali, B. (2011). Damage identification in civil engineering structures utilizing PCA-compressed residual frequency response functions and neural network ensembles. *Structural Control & Health Monitoring*, 18(2), 207-226. doi:10.1002/stc.369
- Lim, H. C., Ong, Z. C., & Brandt, A. (2018). Implementation of phase controlled impact device for enhancement of frequency response function in operational modal testing. *Journal of the Franklin Institute-Engineering and Applied Mathematics*, 355(1), 291-313. doi:10.1016/j.jfranklin.2017.11.031
- Lim, H. C., Ong, Z. C., Ismail, Z., & Khoo, S. Y. (2019). A Performance Study of Controlled Impact Timing on Harmonics Reduction in Operational Modal Testing. *Journal of Dynamic Systems Measurement and Control-Transactions of the Asme*, 141(3). doi:10.1115/1.4041609
- Lin, Y. Z., Nie, Z. H., & Ma, H. W. (2017). Structural Damage Detection with Automatic Feature-Extraction through Deep Learning. *Computer-Aided Civil and Infrastructure Engineering*, 32(12), 1025-1046. doi:10.1111/mice.12313
- Ma, H.-W., Liu, Y.-Z., & Nie, Z.-H. (2019). Physical Interpretation of Principal Component Analysis for Structural Dynamics Through String Vibration. *International Journal of Structural Stability and Dynamics*, 19(9). doi:10.1142/s0219455419501098
- Maeck, J., Wahab, M., & De Roeck, G. (1999). *Damage localization in reinforced concrete beams by dynamic stiffness determination*. Paper presented at the Society for Experimental Mechanics, Inc, 17 th International Modal Analysis Conference.
- Morassi, A., & Rovere, N. (1997). Localizing a notch in a steel frame from frequency measurements. *Journal of Engineering Mechanics-Asce*, 123(5), 422-432. doi:10.1061/(asce)0733-9399(1997)123:5(422)
- Newman, M. E. J. (2004). Fast algorithm for detecting community structure in networks. *Physical Review E*, 69(6), 5. doi:10.1103/PhysRevE.69.066133
- Newman, M. E. J., & Girvan, M. (2004). Finding and evaluating community structure in networks. *Physical Review E*, 69(2), 15. doi:10.1103/PhysRevE.69.026113
- Ni, Y. Q., Wang, B. S., & Ko, J. M. (2002). Constructing input vectors to neural networks for structural damage identification. *Smart Materials & Structures*, 11(6), 825-833. doi:10.1088/0964-1726/11/6/301
- Nielsen, M. A. (2015). *Neural networks and deep learning* (Vol. 2018): Determination press San Francisco, CA.
- Ong, Z. C., Lim, H. C., & Brandt, A. (2018). Automated impact device with non-synchronous impacts: a practical solution for modal testing during operation. *Journal of Zhejiang University-Science A*, 19(6), 452-460. doi:10.1631/jzus.A1700431

- Pandey, A. K., Biswas, M., & Samman, M. M. (1991). Damage Detection from Changes in Curvature Mode Shapes. *Journal of Sound and Vibration*, 145(2), 321-332. doi:10.1016/0022-460x(91)90595-B
- Park, N. G., & Park, Y. S. (2003). Damage detection using spatially incomplete frequency response functions. *Mechanical Systems and Signal Processing*, 17(3), 519-532. doi:10.1006/mssp.2001.1423
- Park, S., Lee, J. J., Yun, C. B., & Inman, D. J. (2008). Electro-mechanical impedance-based wireless structural health monitoring using PCA-data compression and k-means clustering algorithms. *Journal of Intelligent Material Systems and Structures*, 19(4), 509-520. doi:10.1177/1045389x07077400
- Parloo, E., Cauberghe, B., Benedettini, F., Alaggio, R., & Guillaume, P. (2005). Sensitivity-based operational mode shape normalisation: Application to a bridge. *Mechanical Systems and Signal Processing*, 19(1), 43-55. doi:10.1016/j.ymsp.2004.03.009
- Pastor, M., Binda, M., & Harcarik, T. (2012). Modal Assurance Criterion. *Modelling of Mechanical and Mechatronics Systems*, 48, 543-548. doi:10.1016/j.proeng.2012.09.551
- Rahman, A., Ismail, Z., Noroozi, S., & Chao, O. (2013). *Impact-synchronous modal analysis (ISMA)-An attempt to find an alternative*. Paper presented at the 5th International Operational Modal Analysis Conference.
- Rahman, A. G. A., Ismail, Z., Noroozi, S., & Ong, Z. C. (2014). Enhancement of Impact-synchronous Modal Analysis with number of averages. *Journal of Vibration and Control*, 20(11), 1645-1655. doi:10.1177/1077546312475147
- Rahman, A. G. A., Ong, Z. C., & Ismail, Z. (2011). Effectiveness of Impact-Synchronous Time Averaging in determination of dynamic characteristics of a rotor dynamic system. *Measurement*, 44(1), 34-45. doi:10.1016/j.measurement.2010.09.005
- Rehman, A. U., Worden, K., & Rongong, J. A. (2011, Jul 04-06). *Fatigue Crack Detection in Vibrating Structures Using Outlier Detection Analysis*. Paper presented at the 8th International Conference on Structural Dynamics (EURODYN), Leuven, BELGIUM.
- Rhim, J., & Lee, S. W. (1995). A NEURAL-NETWORK APPROACH FOR DAMAGE DETECTION AND IDENTIFICATION OF STRUCTURES. *Computational Mechanics*, 16(6), 437-443.
- Salawu, O. S. (1997). Detection of structural damage through changes in frequency: A review. *Engineering Structures*, 19(9), 718-723. doi:10.1016/s0141-0296(96)00149-6
- Samman, M. M., & Biswas, M. (1994a). Vibration Testing for Nondestructive Evaluation of Bridges .1. Theory. *Journal of Structural Engineering-Asce*, 120(1), 269-289. doi:10.1061/(Asce)0733-9445(1994)120:1(269)

- Samman, M. M., & Biswas, M. (1994b). Vibration Testing for Nondestructive Evaluation of Bridges .2. Results. *Journal of Structural Engineering-Asce*, 120(1), 290-306. doi:10.1061/(Asce)0733-9445(1994)120:1(290)
- Sammut, C., & Webb, G. I. (2011). *Encyclopedia of machine learning*: Springer Science & Business Media.
- Shi, Z. Y., & Law, S. S. (1998). Structural damage localization from modal strain energy change. *Journal of Sound and Vibration*, 218(5), 825-844. doi:10.1006/jsvi.1998.1878
- Shi, Z. Y., Law, S. S., & Zhang, L. M. (2000). Structural damage detection from modal strain energy change. *Journal of Engineering Mechanics-Asce*, 126(12), 1216-1223. doi:10.1061/(asce)0733-9399(2000)126:12(1216)
- Shin, K. (2016). An alternative approach to measure similarity between two deterministic transient signals. *Journal of Sound and Vibration*, 371, 434-445. doi:10.1016/j.jsv.2016.02.037
- Srinivasan, M. G., & Kot, C. (1992). *Effect of damage on the modal parameters of a cylindrical shell*. Paper presented at the 10th International Modal Analysis Conference (IMAC), San Diego, CA.
- Ulriksen, M. D., Tcherniak, D., & Damkilde, L. (2015). Damage detection in an operating Vestas V27 wind turbine blade by use of outlier analysis. *2015 Ieee Workshop on Environmental, Energy and Structural Monitoring Systems (Eesms)*, 50-55.
- Wang, C., Gan, M., & Zhu, C. A. (2018). Fault feature extraction of rolling element bearings based on wavelet packet transform and sparse representation theory. *Journal of Intelligent Manufacturing*, 29(4), 937-951. doi:10.1007/s10845-015-1153-2
- Wang, S. Q., & Xu, M. Q. (2019). Modal Strain Energy-based Structural Damage Identification: A Review and Comparative Study. *Structural Engineering International*, 29(2), 234-248. doi:10.1080/10168664.2018.1507607
- Worden, K., Manson, G., & Fieller, N. R. J. (2000). Damage detection using outlier analysis. *Journal of Sound and Vibration*, 229(3), 647-667. doi:10.1006/jsvi.1999.2514
- Zang, C., & Imregun, M. (2001). Structural damage detection using artificial neural networks and measured FRF data reduced via principal component protection. *Journal of Sound and Vibration*, 242(5), 813-827. doi:10.1006/jsvi.2000.3390
- Zhang, A. P., Ren, G., & Jia, B. Z. (2013). Fault Diagnosis for Marine Engine System Based on Complex Network Cluster Method. *Engineering Solutions for Manufacturing Processes, Pts 1-3*, 655-657, 801-805. doi:10.4028/www.scientific.net/AMR.655-657.801
- Zhou, Y. L., Maia, N. M. M., Sampaio, R. P. C., & Wahab, M. A. (2017). Structural damage detection using transmissibility together with hierarchical clustering

analysis and similarity measure. *Structural Health Monitoring-an International Journal*, 16(6), 711-731. doi:10.1177/1475921716680849

Zimek, A., & Schubert, E. (2017). Outlier Detection. In L. Liu & M. T. Özsu (Eds.), *Encyclopedia of Database Systems* (pp. 1-5). New York, NY: Springer New York.

Universiti Malaya

LIST OF PUBLICATIONS AND PAPERS PRESENTED

- Chen, S., Ong, Z. C., Lam, W. H., Lim, K.-S., & Lai, K. W. (2020). Unsupervised Damage Identification Scheme Using PCA-Reduced Frequency Response Function and Waveform Chain Code Analysis. *International Journal of Structural Stability and Dynamics*, 20(8). doi:10.1142/s0219455420500911
- Chen, S. L., Ong, Z. C., Lam, W. H., Lim, K. S., & Lai, K. W. (2020). Operational Damage Identification Scheme Utilizing De-Noised Frequency Response Functions and Artificial Neural Network. *Journal of Nondestructive Evaluation*, 39(3), 9. doi:10.1007/s10921-020-00709-x
- Chen, S., & Ong, Z. C. (2019). *Waveform chain code: a more sensitive feature selection in unsupervised structural damage detection*. Paper presented at the 2019 1st International Conference on Artificial Intelligence and Data Sciences (AiDAS), Ipoh, MALAYSIA. doi:10.1109/AiDAS47888.2019.8970745

Universiti Malay